Data-based stochastic modeling for short-term dynamic analysis of power systems

Guðrún Margrét Jónsdóttir, MSc

A thesis submitted to University College Dublin
in fulfilment of the requirements for the degree of

Philosophiæ Doctor

College of Engineering and Architecture
School of Electrical and Electronic Engineering

Head of School: Prof. Michael Peter Kennedy
Supervisor: Prof. Federico Milano

November 2020

I hereby certify that the submitted work is my own work, was completed while registered as a candidate for the degree stated on the Title Page, and I have not obtained a degree elsewhere on the basis of the research presented in this submitted work.

til Erlu Kristínar Unnarsdóttur

ACKNOWLEDGEMENTS

I would like to thank my supervisor Federico Milano first and foremost for all his support and guidance throughout the last four years and the Science Foundation Ireland for making this Phd work possible by funding me under project AMPSAS, Grant No. SFI/15/IA/3074.

LIST OF ABBREVIATIONS

ACF Autocorrelation Function

ARMA Autoregressive Moving Average

CARMA Continuous-Time ARMA

CDF Cumulative Distribution Function

COI Centre of Inertia

DAE Differential Algebraic Equation

DFIG Double Fed Induction Generators

OMIB One-Machine Infinite-Bus

OU Ornstein-Uhlenbeck

PDF Probability Density Function

PMSG Permanent Magnet Synchronous Generators

PMU Phasor Measurement Unit

PV Photovoltaic

ROCOF Rate of Change of Frequency

SDAE Stochastic Differential Algebraic Equation

SDE Stochastic Differential Equation

ABSTRACT

Power systems contain randomness and uncertainty. The sources of stochastic variations are for example loads and non-dispatchable renewable energy sources, such as wind and solar. Such variations impact the dynamics and stability of power systems. This thesis addresses the modeling of these sources of stochastic perturbations in the system, specifically for dynamic analysis of power systems.

The fundamental mathematical object utilized in this thesis are Stochastic Differential Equations (SDEs). Systematic methods to build SDEs that can be used to model the stochastic variations are discussed. The thesis focuses on the stochastic modeling of a wide range of statistical properties seen in measurement data, including jumps and correlated processes. Specifically, the objective is to systematically generate SDE models based on the Autocorrelation Function (ACF) and Probability Density Function (PDF) of measurement data. SDE-based models for wind speed, solar irradiance, tidal current speed and load consumption based on measurement data are thoroughly discussed. It is shown that the proposed SDE modeling methods can be used to accurately reproduce the different stochastic properties of these sources of volatility.

The modeling of the aggregated farms of variable renewable energy sources (wind, solar, tidal) and their inclusion into power systems, modeled as Differential Algebraic Equations (DAEs), are discussed. Thus, the full stochastic power system models are a set of Stochastic Differential Algebraic Equations (SDAEs). A method is proposed for initializing the SDAE power system model. It is shown that the proposed initialization method has a lower computation time and requires less disc space when compared to other initialization methods used in the literature for SDAE-based power systems.

Several SDAE power system case studies are presented. The case studies are all built around the all-island Irish system. Cases where the system includes stochastic loads, wind, tidal and solar generation are studied and compared. The case studies show that the fluctuations introduced by the various sources impact the dynamic response of the system in a non-negligible way. Simulation results highlight the importance of stochastic models and the key role of measurement data to accurately model the sources of volatility.

CONTENTS

LIST OF TABLES

LIST OF FIGURES

CHAPTER

ONE

INTRODUCTION

1.1 Motivation

Environmental concerns have lead to a surge in the research and installation of renewable energy sources, mainly wind and solar power. This has resulted in new challenges in the planning, operation and stability analysis of power systems including such renewable resources. These challenges are partially driven by the variability and uncertainty of the energy sources.

Multiple other sources of random variations can be found in power systems, e.g. stochastic load variations and measurement errors in control devices. All these uncertainties can affect the dynamics and stability limits of power systems. As early as in the 1960s the modeling of these random variations using probabilistic analysis has been discussed [1]. In [2], the importance of considering the random fluctuations in power system stability studies is highlighted specifically through probabilistic analysis. Multiple probabilistic analysis methods have been proposed in the literature and a review of those is provided here [3]. In probabilistic analysis the probability distribution of the sources of random variations are considered and their effect on the system variables are studied. However, these analysis typically do not consider how the sources of volatility vary over time. In [4], it is shown that for system stability studies this type of analysis might not always be sufficient and that it is important to model the volatility as stochastic processes evolving with time.

Stochastic Differential Equations (SDEs) can be used to model stochastic processes in power systems. They are continuous with time and therefore well equipped for modeling transient random fluctuations. Since power system models are typically formalized as a set of Differential Algebraic Equations (DAEs), SDEs can be readily incorporated into the system model. The resulting model is a set of Stochastic Differential Algebraic Equations (SDAEs).

Research between 1980-2000 where SDEs are used for dynamic analysis of power systems mostly focused on modeling random load fluctuations. Several publications proposed utilizing variations of the Ornstein-Uhlenbeck (OU) SDE model for modeling these fluctuations [5, 6, 7] and highlighted how these stochastic fluctuations in the loads can affect the stability limits of power systems [8, 9]. Discussion on the use of SDEs in dynamic analysis of power systems since then has regularly popped up but their use has not become common practice. However, in the last five years there has been a boom in SDE-based power system research. The work being done includes using SDEs for forecasting [10, 11], for modeling the individual sources of uncertain variations [12, 13, 14, 15, 16, 17] and for dynamic stability analysis of power systems [18, 19, 20, 21, 22, 23, 24].

In Table 1.1, the SDE-based modeling attempts in the literature for stability analysis of power systems are categorized. Purely Wiener SDE processes that have a Gaussian Probability Density Function (PDF) and are uncorrelated over time have in multiple publications been used for modeling stochastic random perturbations in power systems [18, 19, 21, 22, 23, 25]. In cases where the stochastic variations of loads or wind are considered specifically it is more common to use OU SDEs [13, 26, 27] and using the memoryless transformation or the Fokker-Planck equation in cases where the stochastic variations modeled are non-Gaussian [17, 20, 28, 29, 30]. The OU SDE is a better option than a purely Wiener SDE for modeling physical processes due to its mean reverting properties. It has an Autocorrelation Function (ACF) that is exponentially decaying with time which enables modeling how the stochastic fluctuations evolve with time.

Table 1.1: The SDE methods used in the literature. In the table NC stands for "Not Considered" and ED for "Exponentially Decaying". In the table, correlation refers to modeling correlated SDEs.

Reference	**PDF**	**ACF**	**Jumps**	**Correlation**
[18, 19, 21, 22, 23, 25]	Gaussian	NC	NC	NC
[13, 26, 27]	Gaussian	ED	NC	NC
[17, 20, 28, 29, 30]	Any	ED	NC	NC
[12]	Any	Not only ED	NC	NC
[14, 16]	NC	NC	Yes	NC

However, stochastic processes in power systems can be a combination of faster and slower dynamics. In those cases, more complex ACFs need to be modeled. In [12], an SDE modeling method is presented that captures a wide range of PDFs and ACFs based on measured data. However, this method does not present a systematic way to define which type of SDE model to use depending on the data. Finally, modeling stochastic jumps in the system variables is a topic that has not been discussed extensively but has a lot of potential for modeling jumps in solar generation and loads for example [14, 16].

Thus, the existing literature does not provide a general method to synthesize SDEs to model sources of volatility based on measured data for dynamic analysis of power systems. This makes the topic of this thesis very timely as this research is focused on using measurement data to build SDE-based models for the specific sources of stochastic variations in power systems. These models are built and utilized for dynamic analysis of power systems. This thesis discusses the stochastic modeling of wind, solar and tidal generation as well as loads. Further literature review for the specific sources is provided in the thesis where their modeling is discussed.

1.2 Thesis overview and contributions

This thesis discusses the modeling and inclusion of stochastic processes in dynamic power system studies. To this aim the following topics are addressed:

- The data-driven modeling of volatile renewable energy sources. Specifically, wind, solar and tidal.
- The initialization of dynamic power system models including stochastic processes.
- The inclusion of stochastic processes in time-domain simulations of power systems.

The thesis has two major parts. Chapter 2 and 3 present SDE modeling methods for modeling stochastic variations in power systems and examples how these methods can be used to model specific sources of randomness using measurement data. Chapter 4 and 5 present how the SDE models built can be integrated into conventional power system models for dynamic analysis, discuss the initialization of such a stochastic system model and present power system case studies including the stochastic variations.

The specific chapters of this thesis are organized as follows:

Chapter 2 outlines the theory behind the stochastic models utilized in this thesis. This chapter starts of with an introduction of the statistical properties of stochastic processes that are relevant through out this thesis in Section 2.1. Then, a brief introduction to Stochastic Differential Equations (SDEs) is presented in Section 2.2. In Section 2.3, the four different specific modeling methods utilized in this thesis are outlined. These are presented in an order that corresponds to the time-line of this thesis work. The first two methods aim to capture the specific Autocorrelation Function (ACF) and Probability Density Function (PDF) of continuous stochastic processes so that measured data may be conveniently modeled. Both Method I and II presented in Subsections 2.3.1 and 2.3.2 respectively utilize the memoryless transformation to impose an arbitrary PDF. Thus, the two methods can be distinguished in the way the ACF is imposed. Method I, presented in Subsection 2.3.1 builds continuous-time SDEs that are equivalent to discrete-time Autoregressive Moving Average (ARMA) models. These SDE models are termed Continuous-Time ARMA (CARMA). This method utilizes the fact that ARMA models are well-known and can capture a wide range of ACFs. Method II, outlined in Subsection 2.3.2 captures the ACF of a stochastic process through the superposition of the SDE Ornstein-Uhlenbeck (OU) processes. This method can model any ACF that can be modeled as a weighted sum of exponentially decaying and/or sinusoidal functions. The third method, presented in Subsection 2.3.3 discusses the inclusion of jumps. Specifically, jump diffusion SDEs. Finally, in Subsection 2.3.4 the modeling of the correlation of two SDEs is discussed.

In Chapter 3, the stochastic modeling methods outlined in Chapter 2 are utilized to model the sources of uncertain variations of several renewable energy sources. The renewable energy sources discussed in this thesis are wind (Section 3.1), solar (Section 3.2) and tidal (Section 3.3). All the modeling efforts made in this chapter are supported by measurement data. For each renewable source the necessary background and literature review is presented in the beginning of the respective section. The modeling of wind is discussed in Section 3.1 and both Method I and II (Subsections 2.3.1-2.3.2) are utilized to model wind speed, as presented in Subsection 3.1.2 and 3.1.3 respectively. The modeling of solar is outlined in Section 3.2. For modeling the jumpy behavior seen in the measured solar irradiance Method III (Subsection 2.3.3) is used. Section 3.3 compares the modeling of tidal current speed variations to the modeling of the more well-known volatility seen in wind speed. Then, Method II (Subsection 2.3.2) is applied to model the short-term fluctuations seen in the tidal current speed both due to turbulence and waves. Finally, a combination of Method III (Subsection 2.3.3) and Method IV (Subsection 2.3.4) is used to model the active and reactive power consumption of loads as stochastic with jumps and correlated. This model is outlined in Section 3.4.

Chapter 4 discusses the inclusion of SDE models into dynamic power system models. Typically, power systems are modeled as a set of Differential Algebraic Equations (DAEs). The full stochastic power system model is then a set of Stochastic Differential Algebraic Equations (SDAEs) as presented in Section 4.1. The initialization of such system models is discussed in Section 4.2. The two initialization methods that have been used in the literature are presented and their drawbacks highlighted. An alternative way to initialize the system modeled as a set of SDAEs is proposed. Finally, in Section 4.3 the modifications made to the stochastic models of the renewable energy sources (presented in Chapter 3) to include them in dynamic power system models are outlined. The modified stochastic processes provide the stochastic variations of the aggregated output of the full renewable energy plant. The One-Machine Infinite-Bus (OMIB) test system is used to demonstrate the initialization method and to compare the effect of the different modeled sources of renewable energy in Subsections 4.2.2 and 4.3.4, respectively.

Chapter 5 includes four case studies where stochastic power system models are studied. In Section 5.1, the $1,479$ bus all-island Irish transmission system model is presented. This is system is used in all of the case studies presented in this chapter. The initialization methods for power systems modeled as SDAEs, presented in Section 4.2 are compared and tested for the Irish system in Section 5.2. Section 5.3 outlines a case study of the Irish system where the short-term effect of installing tidal generation on the system is studied in reference to wind generation. Several scenarios where waves are present in the tidal current are studied and frequency control for the tidal turbines is tested to mitigate the frequency fluctuations that the tidal generation introduces. In a similar manner, the effect of including solar generation in the Irish system is studied in Section 5.4. Two scenarios are compared, that is a case where the renewable energy in the system is purely supplied by wind and a case where both wind and solar are used. Finally, in Section 5.5, the effect of the correlation in the active and reactive power of loads on the voltage stability of power systems is studied. Two systems are used, that is both the 3-machine, 9-bus system and the Irish system.

Finally, in Chapter 6 conclusions are drawn and future work outlined.

1.3 Publications

1.3.1 Journal papers

Papers closely related to the thesis

1. *G. M. Jónsdóttir*, F. Milano, Data-based Continuous Wind Speed Models with Arbitrary Probability Distribution and Autocorrelation, Renewable Energy, Elsevier, Vol. 143, pp. 368-376, December 2019.

2. *G. M. Jónsdóttir*, F. Milano, Modeling of Short-Term Tidal Power Fluctuations, IEEE Transactions on Sustainable Energy, accepted in November 2019, in press.

3. *G. M. Jónsdóttir*, M. A. Adib Murad, F. Milano, On the Initialization of Transient Stability Models of Power Systems with the Inclusion of Stochastic Processes, IEEE Transactions on Power Systems, accepted on April 2020, in press.

Other papers

4. L. Vanfretti, *G. M. Jónsdóttir*, M. S. Almas, E. Rebello, S. R. Firouzi, M. Baudette, Audur: A platform for synchrophasor-based power system wide-area control system implementation, SoftwareX, Elsevier, Vol. 7, pp. 294-301, 2018.

5. G. Coletta, A. Laso, *G. M. Jónsdóttir*, M. Manana, D. Villacci, A. Vaccaro, F. Milano, On-line Control of DERs to Enhance the Dynamic Thermal Rating of Transmission Lines, Transactions on Sustainable Energy, accepted in March 2020, in press.

6. M. Koivisto, *G. M. Jónsdóttir*, P. Sørensen, K. Plakas, N. Cutulis, Combination of meteorological reanalysis data and stochastic simulation for modelling wind generation variability, accepted in Renewable energy in June 2019, in press.

1.3.2 Conference papers

Papers closely related to the thesis

1. *G. M. Jónsdóttir*, B. Hayes, F. Milano, Continuous-time ARMA Models for Data-based Wind Speed Models, 20th Power System Computation Conference (PSCC), Dublin, Ireland, 11-15 June 2018.
2. *G. M. Jónsdóttir*, F. Milano, Modeling Solar Irradiance for Short-term Dynamic Analysis of Power Systems, IEEE PES General Meeting, Atlanta, GA, 4-8 August 2019.
3. *G. M. Jónsdóttir*, F. Milano, Stochastic Modeling of Tidal Generation for Transient Stability Analysis: A Case Study based on the All-Island Irish Transmission System, 21st Power System Computation Conference (PSCC), 29 June - 3 July 2020.
4. *G. M. Jónsdóttir*, F. Milano, Modeling Correlation of Active and Reactive Power of Loads for Short-Term Analysis of Power Systems, 20th International Conference on Environment and Electrical Engineering (EEEIC), 9-12 June 2020.

Other papers

5. F. Milano, *G. M. Jónsdóttir*, Jupyter Notebooks for Computer-based Laboratories on Power System Dynamics and Control, EDULEARN 2018, Palma de Mallorca, Spain, 2-4 July 2018.
6. *G. M. Jónsdóttir*, B. Hayes, F. Milano, Optimum Data Sampling Frequency for Short-Term Analysis of Power Systems with Wind, IEEE PES General Meeting, Portland, OR, 5-10 August 2018.
7. A. Nic Einrí, *G. M. Jónsdóttir*, F. Milano, Modeling and Control of Marine Current Turbines and Energy Storage Systems, IFAC Workshop on Control of Smart Grid and Renewable Energy Systems (CSGRES), Jeju, Korea, 10-12 June 2019.

8. M. Adeen, *G. M. Jónsdóttir*, F. Milano, Statistical Correlation between Wind Penetration and Grid Frequency Variations in the Irish Network, 19th International Conference on Environmental and Electrical Engineering (EEEIC), Genova, Italy, 11-14 June 2019.

9. *G. M. Jónsdóttir*, F. Milano, Jupyter Notebooks for Computer-based Laboratories on Electrical Energy Systems, EDULEARN 2019, Palma de Mallorca, Spain, 1-3 July 2019.

10. *G. M. Jónsdóttir*, M. Koivisto, P. E. Sørensen, F. Milano, Modelling Wind Speeds using CorRES: Combination of Mesoscale Reanalysis Data and Stochastic Simulations, 18th Wind Integration Workshop, Dublin, Ireland, 16-18 October 2019.

11. J. R. Céu, *G. M. Jónsdóttir*, F. Milano, R. A. Ramos, On the Impact of Non-Synchronous Devices over the Critical Clearing Time of Low-Inertia Systems, 20th International Conference on Environment and Electrical Engineering (EEEIC), 9-12 June 2020.

12. H. Shokrani, *G. M. Jónsdóttir*, F. Milano, Short-Term Stochastic Modeling of Virtual Power Plants with inclusion of Wind, Solar and Tidal Generation and Energy Storage, 20th International Conference on Environment and Electrical Engineering (EEEIC), 9-12 June 2020.

1.3.3 Publication arising

1. I. Dantí López, M. Desmartin, *G. M. Jónsdóttir*, M. Saguan, D. Flynn, Kohala: a unit commitment model for the simulation of flexibility needs in short-term markets, submitted to Applied Energy in August 2020.

CHAPTER

TWO

STOCHASTIC MODELS

Multiple stochastic models have been proposed and utilized in the literature, such as Autoregressive Moving Average (ARMA) and Markov chains. Another prominent class of stochastic models are Stochastic Differential Equations (SDEs). SDEs are intrinsically continuous in time. Thus, they can capture the transient fluctuations of the stochastic process being modeled. The stochastic models proposed in this thesis are intended to be included in power system models used for dynamic analysis. Typically, power systems are formalized as a set of Differential Algebraic Equations (DAEs). These models can readily incorporate stochastic processes modeled as SDEs. Thus, the main focus of the stochastic modeling done in this thesis is on SDEs.

This chapter presents the stochastic models and theory used in this thesis. First, in Section 2.1, some background on stochastic processes is presented. A brief introduction to SDEs is presented in Section 2.2 as they are the main building block in all the modeling done in this thesis. In Section 2.3, the different stochastic modeling methods used in this thesis are outlined.

2.1 The properties of stochastic processes

A *random variable* X is a real function defined on a sample space. For every real number x there exists a probability $F_X(x) = \mathrm{P}[X \leq x]$ (Note that F_X is termed the Cumulative Distribution Function (CDF) of the random variable X). x denotes a value of the random variable X, that is x is an outcome of the random phenomenon X. A random variable X has *mean value*:

$$\mu_X = \mathrm{E}[X], \tag{2.1}$$

and *variance*:

$$\zeta_X = \mathrm{E}[(X - \mu_X)^2], \tag{2.2}$$

and standard deviation $\sigma_X = \sqrt{\zeta_X}$, where E is the expected value operator or *expectation*. A random variable X is characterized by its *Probability Density Function (PDF)*. The PDF describes all the possible values and likelihoods that the values of the random variable can take within a given range. A continuous PDF, $f(x)$ for the value x, is a function that satisfies the following properties:

1. The probability that x is between two points a and b is:

$$P[\, a \leq x \leq b \,] = \int_a^b f(x)dx. \tag{2.3}$$

2. The PDF is non-negative for all real variables x.

3. The integral of the PDF is:

$$\int_{-\infty}^{\infty} f(x)dx = 1. \tag{2.4}$$

An important probability distribution is the normal (or Gaussian) distribution. A random variable that is normally distributed with the mean μ and standard deviation σ (often referred to as $N(\mu, \sigma)$) has the PDF:

$$f_N(x) = \frac{1}{\sigma\sqrt{2\pi}} \exp\left(-\frac{1}{2}\left(\frac{x-\mu}{\sigma}\right)^2 \right). \tag{2.5}$$

In Figure 2.1, an example of a Gaussian distributions PDF and CDF is shown. In this case the mean is $\mu = 4$ and the standard deviation is $\sigma = 1$. The Gaussian PDF has a distinctive bell shape around the mean and gives the probability of each value x of the random variable. The CDF on the other hand gives the cumulative probability of values equal to or smaller than each value x of the random variable.

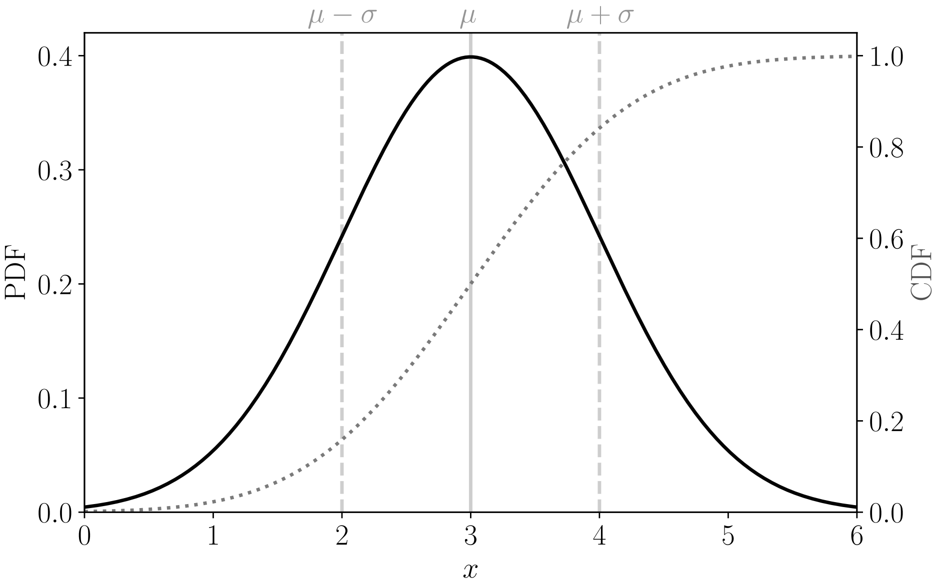

Figure 2.1: PDF and CDF of a Gaussian distribution with the mean $\mu = 4$ and standard deviation $\sigma = 1$.

The Gaussian distribution is the most widely used probability distribution as it gives a good fit in many cases, e.g. for measurement errors. However, other probability distribution shapes are also common. Wind speed for example has a probability distribution that is shifted to the left and tails heavily to the right. This is because lower wind speeds are typically more common than extreme wind speeds. The Weibull distribution PDF is defined as:

$$f_{\mathrm{W}}(x) = \begin{cases} \frac{\lambda_1}{\lambda_2}\left(\frac{x}{\lambda_2}\right)^{\lambda_1 - 1} \exp\left[-\left(\frac{x}{\lambda_2}\right)^{\lambda_1}\right] & \text{if } x \geq 0 \\ 0 & \text{if } x < 0, \end{cases}$$

where λ_1 is a shape parameter and λ_2 is a scale parameter. An example of the Weibull distribution is shown in Figure 2.2.

In some cases, e.g., steady-state analysis [31], it is enough to only use random variables and thereby only consider the PDF. This type of analysis is called probabilistic analysis. However, for dynamic time-domain simulations of power

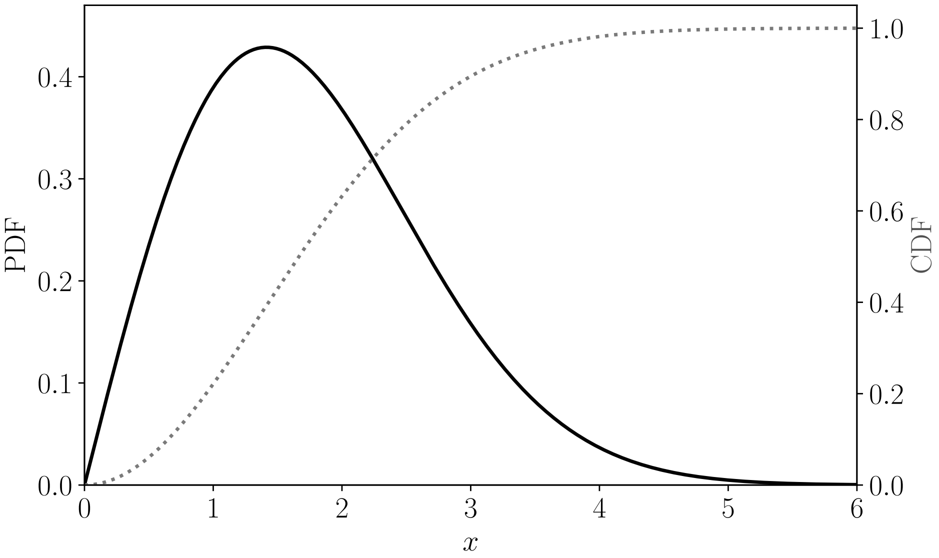

Figure 2.2: PDF and CDF of a Weibull distribution with $\lambda_1 = \lambda_2 = 2$.

systems, stochastic processes need to be considered. A *stochastic process* is a family of values from a random variables $\{x(t) : t \in T\}$, where in our case t denotes time. That is, at every time t in the set T, a random value $x(t)$ is observed. A way to model stochastic processes in continuous time is to use SDEs as presented below.

2.2 Stochastic differential equations

Stochastic Differential Equations (SDEs) are continuous-time stochastic processes. They are a prominent mathematical modeling technique employed in areas such as finance for modeling stock prices or interest rates and physics to model particles in fluids. This section only presents a brief introduction to SDEs. A more extensive presentation of SDEs can be found in [32, 33, 34].

A generic multi-dimensional SDE has the form:

$$d\boldsymbol{\eta}(t) = \boldsymbol{a}(t, \boldsymbol{\eta})dt + \boldsymbol{B}(t, \boldsymbol{\eta})d\boldsymbol{W}(t), \tag{2.6}$$

where $\boldsymbol{a}$ ($\boldsymbol{a} : \mathbb{R}^{n_\eta} \times \mathbb{R}^{+} \mapsto \mathbb{R}^{n_\eta}$) and $\boldsymbol{B}$ ($\boldsymbol{B} : \mathbb{R}^{n_\eta} \times \mathbb{R}^{+} \mapsto \mathbb{R}^{n_\eta}$) are continuous functions and are referred to as the drift and diffusion term of the SDE, respectively. $\boldsymbol{W}$ represents the n_w-dimensional vector of stochastic components driving the SDE. This vector is composed of n_w independent scalar Wiener processes, $\{W(t), t > 0\}$, which is a random function characterized by the following properties:

1. $W(0) = 0$, with probability 1.
2. The function $t \mapsto W(t)$ is continuous in t.
3. If $t_1 \neq t_2$, then $W(t_1)$ and $W(t_2)$ are independent.
4. For $\forall t_i \geq 0$, all increments, $\Delta W_i = W(t_{i+1}) - W(t_i)$, are normally distributed, with mean 0 and variance $h = t_{i+1} - t_i$, i.e., $\Delta W_i \sim \mathcal{N}(0, h)$.

Examples of Wiener processes are shown in Figure 2.3. Wiener processes cannot be integrated in the conventional Riemann-Stieltjes sense as they are not bounded, i.e., the limit $\lim_{x \to 0}(W(t + \Delta t) - W(t))/\Delta t$ does not exist. Therefore, the correct mathematical formulation of the solution of (2.6) is the integral form:

$$\boldsymbol{\eta} = \boldsymbol{\eta}(t_0) + \int_{t_0}^{t} \boldsymbol{a}(\boldsymbol{\eta}, s) ds + \int_{t_0}^{t} \boldsymbol{b}(\boldsymbol{\eta}, s) d\boldsymbol{W}(s), \quad t \in [t_0, t_f], \tag{2.7}$$

where the first integral is an ordinary Riemann-Stieltjes integral and the second one is a stochastic integral. There are several different ways to interpret stochastic integrals. Mainly, Itô's approach, Stratonovich's approach or the backward integral. In this thesis, the most widely used approach is used, namely, the Itô integral.

In most cases SDEs cannot be analytically solved. Thus, numerical methods are used to solve the SDEs. The most common numerical integration schemes for SDEs are the Euler and Milstein schemes. In this work the stochastic Euler scheme is most often used to solve the the SDEs, or at least the diffusion part of the integral in (2.7). Reference [33] provides extensive details on the numerical integration schemes for SDEs.

A *stationary* stochastic processes is characterized by a PDF that does not change with time. An example of a non-stationary process is the Wiener processes.

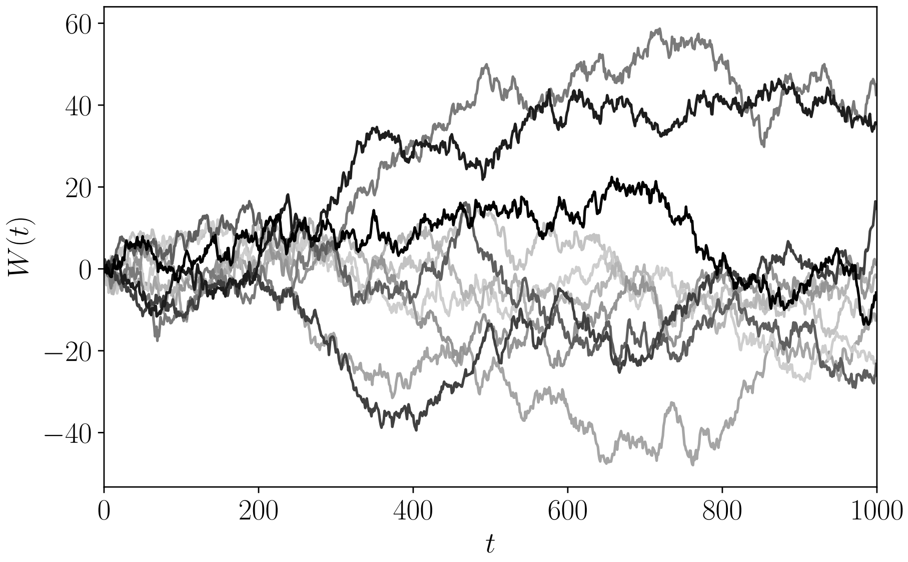

Figure 2.3: Ten simulated sample paths of Wiener processes, illustrating their great variability.

Its mean is constant but its standard deviation, $\sqrt{t}$, changes with time. In this thesis only stationary stochastic processes are considered, even though some non-stationary stochastic processes affect power systems. For example, wind speed with an hourly resolution or bigger may be modeled more accurately with non-stationary models [35]. This is due to the daily, and seasonal variations in the wind speed. However, for the purpose of simulating wind speed within a 10 minute time frame, non-stationary models do not perform better than stationary ones [35]. This is typically, the case for short-term analysis of stochastic processes within the seconds to minutes time frame, which is the time frame considered in dynamic analysis of power systems. Thus, considering non-stationarity is outside the scope of this thesis.

A stationary stochastic process is characterized by its Probability Density Function (PDF) and Autocorrelation Function (ACF). The *Autocorrelation Function (ACF)* is a measure of how the process changes over time. That is, the ACF gives a measure of the relationship between the current process value and past process values. Its mathematical definition for a stationary stochastic process $x(t)$ is:

$$R_x(\tau) = \frac{\mathrm{E}[(x(t) - \mu_x)(x(t+\tau) - \mu_x)]}{\zeta_x}, \tag{2.8}$$

where τ stands for the time lag. μ_x and ζ_x are the mean of and variance of the stochastic process $x(t)$. The *autocovariance function* of the stochastic process $x(t)$ is defined as $R_x(\tau)\zeta_x$.

The *Ornstein-Uhlenbeck (OU)* process is a popular building block in SDE modeling. It is stationary, with a Gaussian PDF which exhibits mean reversion, i.e., it drifts towards its mean value at an exponential rate. It is considered as a modification of the Wiener process, with a bounded standard deviation which makes it suitable to model physical processes, such as wind and load fluctuations [13, 36, 37]. The general form of an OU SDE process is:

$$dX(t) = \alpha(\mu - X(t))dt + \sigma dW(t), \tag{2.9}$$

where α, $\sigma > 0$. α is the mean reversion speed of the process, $X(t)$, which defines the slope of its exponentially decaying ACF. The process $X(t)$ is Gaussian distributed with the mean μ and variance $\sigma^2/(2\alpha)$. In Figure 2.4, examples of simulated OU process trajectories for the OU SDE $X_1(t)$ are shown where $\alpha = 0.01$, $\mu = 0$ and $\sigma = 1$. This shows that this modification to the Wiener process enables the modeling of bounded mean-reverting stochastic processes.

In Figure 2.5, examples of simulated OU process trajectories for another SDE $X_2(t)$ are shown. However, in this case $\alpha = 0.001$. α defines the ACF of the OU process. Thus, by comparing Figure 2.4 and 2.5 the difference in the ACF makes can be observed. That is for a smaller α the processes varies slower over time. The ACFs of $X_1(t)$ and $X_2(t)$ are shown in Figure 2.6.

The starting point of this thesis work is the SDE-modeling method presented in [17]. This method enables modeling SDEs with a certain analytically defined PDF and an exponentially decaying ACF. This method has been used to model wind speed based on measured data with a hourly resolution. However, stochastic processes sampled more frequently, for example every second or minute will typically not have an exponentially decaying ACF, as is shown for wind speed

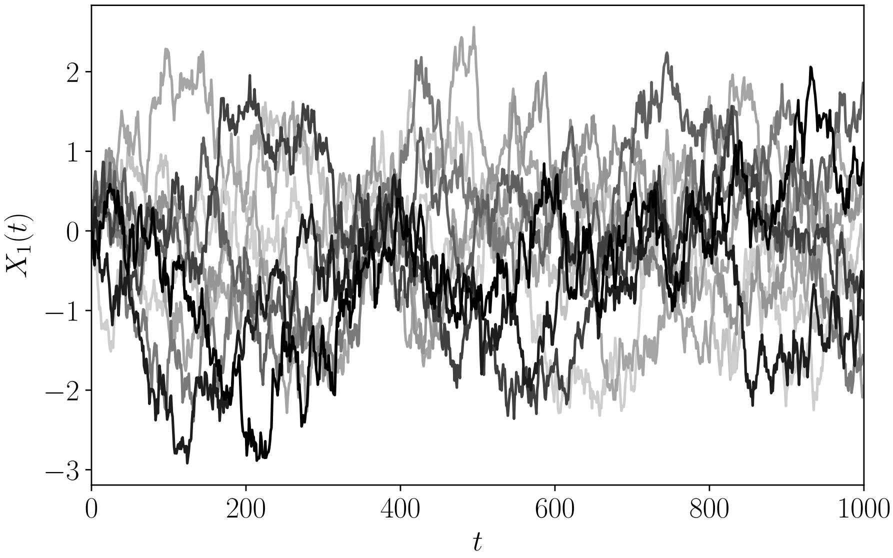

Figure 2.4: Ten simulated sample paths of an OU SDE where $\alpha = 0.01$, $\mu = 0$ and $\sigma = 0.14$.

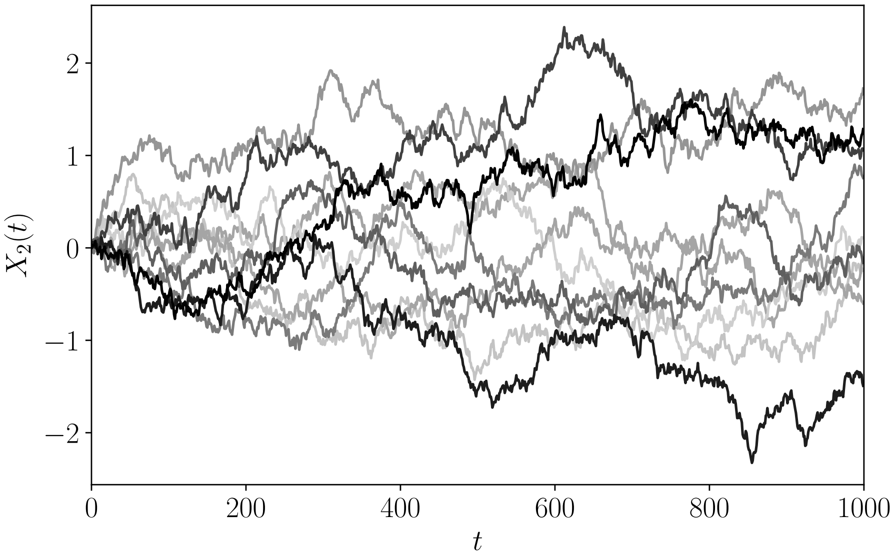

Figure 2.5: Ten simulated sample paths of an OU SDE where $\alpha = 0.001$, $\mu = 0$ and $\sigma = 0.04$.

data in [38]. In these cases the stochastic processes are often a combination of fast and slow dynamics. Then, the ACF is better described as a weighted sum of exponentially decaying functions. Thus, models that capture a wider range of both PDFs and ACFs are needed.

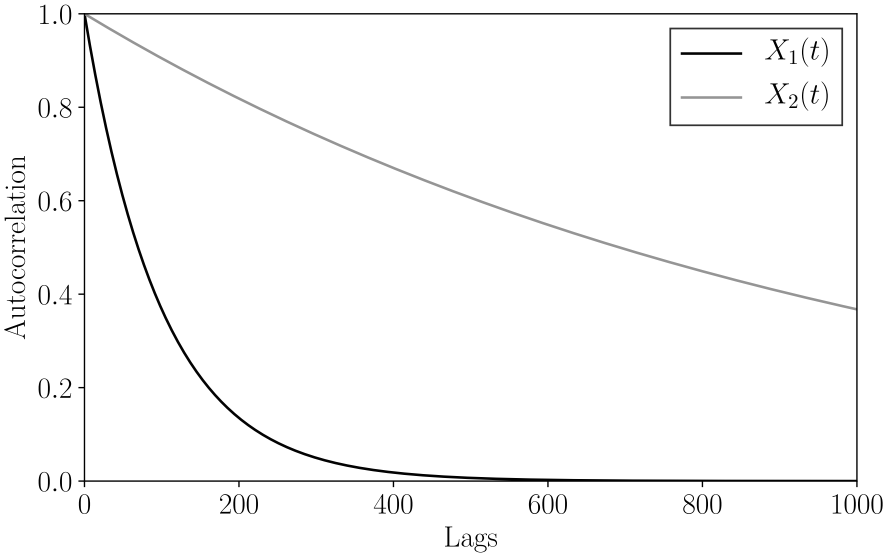

Figure 2.6: ACFs of OU processes $X_1(t)$ and $X_2(t)$.

2.3 Stochastic modeling methods

The starting point is SDE-based models with an exponentially decaying ACF. Thus, the first objective of this thesis work is to be able to build SDE models with more complex ACFs. Autoregressive Moving Average (ARMA) models have been widely used in the literature to model and forecast both load consumption [39, 40] and wind generation [41, 42, 43]. They can model a wide range of ACFs. However, these models are discrete. Method I, presented in Subsection 2.3.1, enables building an equivalent SDE for an ARMA model, called a CARMA model.

2.3.1 Method I - Continuous-Time ARMA models

Autoregressive Moving Average (ARMA) models are the class of stochastic models that have been the most widely studied and utilized in the literature. They are well-established and offer comprehensive tools to fit the model to data [44]. However, ARMA models are discrete and have a fixed time step that must match the sampling interval of the available data. Therefore, ARMA models are not suitable for dynamic analysis of power systems as they typically have a smaller time step than the available data and/or require a varying time step.

This modeling method enables the use of ARMA models in continuous-time which facilitates their use in time-domain simulations of power systems for dynamic analysis. The proposed approach is based on the observation that if an ARMA model is stationary then it has an equivalent SDE, termed a Continuous-Time ARMA (CARMA) [45].

Method I includes two or four steps to produce the CARMA-SDE model depending on the PDF of the stochastic process being modeled. The four steps of the method are shown in Figure 2.7. *Step 2* and *3* enable building a SDE-based model with the desired ACF. In *Step 1* and *4* the desired PDF is imposed. If the stochastic process being modeled is normally distributed *Step 1* and *4* can be skipped. Further details on each step are provided here below.

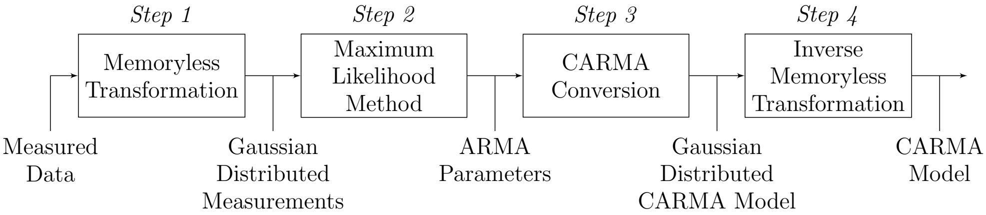

Figure 2.7: Four steps to construct the SDE-based CARMA stochastic models using Method I.

Step 1: Memoryless transformation

ARMA and CARMA models require the data to be normally distributed. Therefore, the measured data being modeled must be fitted to the Gaussian distribution. This is achieved using a memoryless transformation.

The memoryless transformation fits non-normally distributed data to the Gaussian distribution while retaining its original stochastic properties. This is achieved by applying the inverse Gaussian CDF to the CDF of the measured data, as follows:

$$x_{\text{data}}(t) = \Phi^{-1}(F(X_{\text{data}}(t))) \, , \tag{2.10}$$

where Φ^{-1} is the inverse CDF of the imposed Gaussian distribution and F is the CDF of the probability distribution of the measured data [46]. $X_{\text{data}}(t)$ is the measured data time-series. The resulting time-series $x_{\text{data}}(t)$ represents modified normally distributed measured data that can be used to build an ARMA model.

Step 2: ARMA modeling

ARMA models can model and forecast variations of a stochastic processes based on historical data. There are well-established estimation techniques available that simplify the building of custom ARMA stochastic models based on measured data [47].

ARMA models can be divided into two components, namely, Autoregressive (AR) and Moving Average (MA):

- *Autoregressive*: relates the current value of the stochastic process to past values.
- *Moving Average*: relates the current value of the stochastic process to past error values.

The ARMA(p, q) model is given by

$$X_t = \underbrace{\sum_{i=1}^{p} \phi_i X_{t-i}}_{AR} + \underbrace{\sum_{i=1}^{q} \theta_i \varepsilon_{t-i}}_{MA} + \varepsilon_t \ , \tag{2.11}$$

where ε_t is white noise with a standard deviation σ_a, ϕ_i are the autoregressive parameters, θ_i are the moving average parameters and both ϕ_p and θ_q are non-zero.

ARMA models of second order or higher have been widely used to model for example wind speed [41, 42, 43]. The ARMA(2,1) model is used as an example here. However, ARMA models of other higher orders can also be utilized in this method as shown in [45]. The ARMA(2,1) model can be written as

$$\phi(B) X_t = \theta(B) \varepsilon_t \ , \tag{2.12}$$

where B is the backward operator such that $BX_t = X_{t-1}$ and

$$\phi(B) = 1 - \phi_1 B - \phi_2 B^2, \tag{2.13}$$

$$\theta(B) = 1 + \theta_1 B \; . \tag{2.14}$$

Several well-known methods are available to estimate ARMA parameters directly from data such as the Least Squares method, the Method of Moments and the Maximum Likelihood method [44]. In this research, the Maximum Likelihood method has been used. The method finds the parameter values of the ARMA model which maximizes the Likelihood Function of the sampled data. The Likelihood Function is based on the Gaussian CDF of the sampled data. The estimated ARMA parameters are used to find the equivalent CARMA parameters.

Step 3: CARMA modeling

Stochastic phenomena affecting power systems are continuous-time processes. However, measured data are sampled and thus are discrete. For this reason, ARMA models are popular for modeling measured data. CARMA models are the continuous-time counterparts of the discrete-time ARMA models. While ARMA models are limited to using the fixed time step of the sampled data, CARMA models enable the use of smaller and/or variable time steps. Hence, CARMA models can be used to interpolate between sampling points.

A CARMA(p, q) model denoted by $x(t)$ is a SDE of the form

$$\frac{d^p x}{dt^p} + c_{p-1}\frac{d^{p-1}x}{dt^{p-1}} + \ldots + c_1\frac{dx}{dt} + c_0(x(t) - \mu) = b_0 dW(t) + b_1\frac{dz}{dt} + \ldots + b_q\frac{d^q z}{dt^q} \; , \tag{2.15}$$

where $W(t)$ is the standard Wiener process, c_i are the autoregressive coefficients, b_i are the moving average coefficients and both c_i and b_i are real and $b_q \neq 0$ [48, 49, 50].

Generally, a stationary CARMA(p, q) model sampled regularly can be written as an ARMA(p, $p-1$) model with $q < p$ [45]. The simplest example is the

Ornstein-Uhlenbeck (OU) process i.e. CARMA(1,0)

$$dX_t + c_0 X_t = dW(t) \ , \tag{2.16}$$

which is equivalent to an ARMA(1,0) model viewed with a fixed time step h

$$X_t = \exp(-c_0 h) X_{t-1} + \varepsilon_t \ . \tag{2.17}$$

The autoregressive parameter of the discrete-time ARMA, $\phi_1 = \exp(-c_0 h)$, cannot be negative.

The CARMA(2,1) model can be written as

$$c(D)x(t) = b(D)dW(t) \ , \tag{2.18}$$

where D is the differential operator and

$$c(z) = z^2 + c_1 z + c_0, \tag{2.19}$$

$$b(z) = b_0 + b_1 z \ . \tag{2.20}$$

An equivalent discrete-time ARMA(2,1) model, presented in (2.12) can be found if the CARMA(2,1) model is stationary. The CARMA(2,1) model is stationary if the real parts of the roots of (2.19), α_1 and α_2, are negative. The autoregressive parameters of the continuous-time model, c_1 and c_0, can be directly connected to the autoregressive parameters of the discrete-time model, ϕ_1 and ϕ_2, using the Z-transformation.

$$\phi_1 = e^{\alpha_1 h} + e^{\alpha_2 h}, \tag{2.21}$$

$$\phi_2 = -e^{(\alpha_1 + \alpha_2)h} \ . \tag{2.22}$$

The theoretical autocovariance function of a discrete-time ARMA(2,1) model is defined as

$$\gamma_{\text{ARMA}}(k) = \begin{cases} \phi_1\gamma(1) + \phi_2\gamma(2) + \theta_1(\phi_1 + \theta_1)\sigma_a^2 + \sigma_a^2 & \text{if } k = 0 \\ \phi_1\gamma(0) + \phi_2\gamma(1) + \theta_1\sigma_a^2 & \text{if } k = 1 \\ \phi_1\gamma(k-1) + \phi_2\gamma(k-2) & \text{if } k > 1 \ , \end{cases} \tag{2.23}$$

where k is the time lag and $\gamma = \gamma_{\text{ARMA}}$. The theoretical autocovariance function of a CARMA(2,1) model is

$$\gamma_{\text{CARMA}}(h) = e^{\alpha_1 h}\frac{b(\alpha_1)b(-\alpha_1)}{c'(\alpha_1)c(\alpha_1)} + e^{\alpha_2 h}\frac{b(\alpha_2)b(-\alpha_2)}{c'(\alpha_2)c(\alpha_2)} \ . \tag{2.24}$$

The moving average parameter of the continuous-time model, b_1, is set so that the autocovariance of the discrete-time model, γ_{ARMA}, is equal to the autocovariance of the continuous-time model, γ_{CARMA}. This method can be extended to map the parameters from any CARMA(p, q) model, where $p > q$, to find the equivalent ARMA(p, $p-1$) parameters [48].

The resulting CARMA model is normally distributed. Hence, if the desired probability distribution is non-Gaussian it has to be imposed. This is achieved using the inverse memoryless transformation.

Step 4: Inverse memoryless transformation

The inverse of the memoryless transformation in *Step 1* is used to impose the true PDF of the measured data being modeled. The inverse CDF of the measurement data is applied to the Gaussian CDF of the CARMA model

$$y(t) = F^{-1}(\Phi(x(t))) \ . \tag{2.25}$$

This obtains the desired PDF of the measurement data [46]. The memoryless transformation and its inverse enable the use of ARMA and CARMA models to model data with any probability distribution that has a defined CDF and inverse CDF.

A relevant advantage of this approach based on the memoryless transformation, is that it can be used with any analytical or numerical PDF that has been fitted to the probability distribution of the data.

Thus, Method I enables the modeling of SDE stochastic processes with an arbitrary PDF and a wider range of ACFs as compared to [17]. In Subsection 3.1.2, it is shown how this method can be used to model wind speed. This method works well in cases where an ARMA model has already been determined and a continuous-time equivalent is required. Otherwise, having to find the ARMA model first and then build the SDE model based on the ARMA model makes the modeling procedure time consuming and complex when compared to Method II. Method II, presented in Subsection 2.3.2, proposes a more straightforward way to build SDE models with a wide range of ACFs. It is based on using the superposition of Ornstein-Uhlenbeck (OU) processes to model any ACF that can be fitted as a weighted sum of exponential and/or sinusoidal functions. It uses the memoryless transformation to impose an arbitrary PDF.

2.3.2 Method II - Ornstein-Uhlenbeck-based models

The following 2-dimensional OU is utilized as the building block for this method:

$$\begin{pmatrix} dX(t) \\ dY(t) \end{pmatrix} = \begin{pmatrix} -\alpha & -\omega \\ \omega & -\alpha \end{pmatrix} \begin{pmatrix} X(t) \\ Y(t) \end{pmatrix} dt + \begin{pmatrix} \sigma \\ 0 \end{pmatrix} dW(t). \tag{2.26}$$

where $\alpha > 0$, $\sigma > 0$, $\omega \geq 0$ and $W(t)$ is a standard Wiener process. The correlation matrix of the SDE in (2.26) is:

$$\boldsymbol{R}(\tau) = \mathbb{E}\left(\begin{pmatrix} X(t+\tau) \\ Y(t+\tau) \end{pmatrix} \big(X(t), Y(t) \big) \right) = \exp(-\alpha\tau) \begin{pmatrix} \cos(\omega\tau) & -\sin(\omega\tau) \\ \sin(\omega\tau) & \cos(\omega\tau) \end{pmatrix}. \tag{2.27}$$

The process $X(t)$ has the ACF:

$$R_X(\tau) = \exp(-\alpha\tau)\cos(\omega\tau), \tag{2.28}$$

In stationary conditions, $X(t)$ is Gaussian distributed with zero mean and variance $\sigma^2/(2\alpha)$.

For $\omega = 0$, $X(t)$ and $Y(t)$ are decoupled and $X(t)$ becomes a conventional 1-dimensional Ornstein-Uhlenbeck (OU) process:

$$dX(t) = -\alpha X(t)dt + \sigma dW(t), \tag{2.29}$$

with an exponentially decaying ACF:

$$R_X(\tau) = \exp(-\alpha\tau). \tag{2.30}$$

The main idea behind this method is to use a summation of a set of SDEs of the form (2.26) to impose the target ACF. The memoryless transformation in (2.25) is used to impose the desired PDF. The resulting compound stochastic process is build in such a way that it has the same PDF and ACF as the given measured data.

The steps to build the desired compound stochastic process are twofold: *Step 1*, a superposition of SDEs that captures the desired ACF is defined; and *Step 2*, an analytical or numerical memoryless transformation that imposes the desired PDF is applied to the SDEs determined in the previous step.

Step 1: Impose the autocorrelation

In [51], a superposition of OU processes is used for imposing an ACF represented with a weighted sum of exponentially decaying functions. We generalize the technique in [51] with the 2-dimensional OU in (2.26) instead of the conventional OU process. In this way, Method II is able to reproduce not only exponentially decaying ACFs but also periodical behaviors.

Let $Z(t)$ be a stochastic process obtained as the weighted sum of n SDE processes, as follows:

$$Z(t) = \sum_{i=1}^{n} \sqrt{w_i}\, X_i(t), \tag{2.31}$$

where $X_i(t)$, $i = 1, \dots n$, are SDE processes with ACFs $R_{X_i}(\tau)$, $w_i > 0$ and

$$\sum_{i=1}^{n} w_i = 1. \tag{2.32}$$

If all n processes have an identical Gaussian PDF $\mathcal{N}(\mu_X, \sigma_X)$, the stochastic process $Z(t)$ has the same Gaussian PDF, $\mathcal{N}(\mu_X, \sigma_X)$, and an ACF which is a weighted sum of the ACFs of the n SDE processes, that is:

$$R_Z(\tau) = \sum_{i=1}^{n} w_i R_{X_i}(\tau). \tag{2.33}$$

If the n SDE processes in (2.31) are $X(t)$ processes as in (2.26), the resulting ACF of $Z(t)$ is a weighted sum of damped sinusoidal and decaying exponential functions and (2.33) can be rewritten as:

$$R_Z(\tau) = \sum_{i=1}^{n} w_i \mathrm{exp}(-\alpha_i \tau) \cos(\omega_i \tau). \tag{2.34}$$

Hence, the superposition of SDE processes allows capturing any ACF that can be modeled as a weighted sum of exponential and/or sinusoidal functions. If the ACF does not show a periodic behavior than $\omega_i = 0$, $\forall i = 1, \dots, n$.

Step 2: Impose the probability distribution

The sum of the SDE processes in (2.31) resulting in the compound process $Z(t)$ has a Gaussian probability distribution. If the stochastic process being modeled has a non-Gaussian PDF the memoryless transformation, presented in Subsection 2.3.1 is used. The transformation in (2.25) is imposed on $Z(t)$ from (2.31). The resulting process is the target SDE with the desired PDF and ACF.

Thus, this method enables the straightforward modeling of SDEs based on data. All that is required is the ACF and the PDF of the data. The ACF is fitted to a weighted sum of exponential and/or sinusoidal functions and the fitted parameters define the SDE. In Sections 3.1 and 3.3, it is demonstrated how this method can be used to model both wind speed and tidal current speed.

However, certain processes in power systems will not only be stochastic but also have faster variations, termed as jumps. These are for example seen in load consumption and solar generation. Method III presents SDE jump diffusion models that can be used to model stochastic process with jumps [52].

2.3.3 Method III - SDEs with jumps

A general one-dimensional jump diffusion model, i.e. SDE with jumps is defined as:

$$d\eta_J(t) = a(t, \eta_J)dt + b(t, \eta_J)dW(t) + c(t, \eta_J)dJ(t). \tag{2.35}$$

Here $c(t, \eta_J)$ is the jump coefficient which determines the jump size and $\{J(t), t > 0\}$ is the Poisson process. The Poisson process with intensity $\lambda > 0$ is defined as a type of stochastic process called a counting process which is characterized by the following properties:

1. $J(0) = 0$, with probability 1.

2. It has stationary independent increments.

3. The number of events (or points) in any given time interval of length t is a Poisson random variable with the mean λt.

4. Its PDF is:

   $$f(k, \lambda) = \frac{\lambda^k}{k!}\exp(-\lambda), \tag{2.36}$$

   where $k \in \mathbb{N}$.

Jump diffusion SDEs have been used in the literature to model both loads [16] and solar irradiance [14]. Sections 3.2 and 3.4 present examples of jump diffusion SDEs modeling solar irradiance and loads, respectively.

Finally, not all stochastic processes seen in power systems are fully independent. Certain variables are typically correlated, such as the active and reactive power consumption of a load, the wind speed and wind direction at a certain location or even two renewable energy sources located in close proximity.

2.3.4 Method IV - Correlated SDEs

The methods presented here enables modeling the correlation between two Wiener process and the two Poisson jump processes. The modeling of the correlation of multiple stochastic processes is outside the scope of this thesis but is included in future work.

Correlated Wiener processes

The Wiener process is the stochastic driving component of a SDE. The correlation of two Wiener processes, say $W_1(t)$ and $W_2(t)$, can be achieved by defining a third Wiener process, say $V(t)$, which is independent from $W_1(t)$. The correlation between $W_1(t)$ and $W_2(t)$ is defined through a parameter $\rho_W(t)$. This can be constant or time varying. In the latter case, $\rho_W(t)$ is modeled as another stochastic process. In this work, ρ_W is assumed to be constant as in [53]. Then $W_2(t)$ is defined as the following adapted Wiener process:

$$dW_2(t) = \rho_W dW_1(t) + \sqrt{1-\rho_W^2} dV(t). \tag{2.37}$$

In Figure 2.8, three example OU SDE processes are shown. Processes $X_1(t)$ and $X_2(t)$ are correlated with the correlation $\rho_W = 0.8$. Thus, similar trends can be seen in $X_1(t)$ and $X_2(t)$. $X_3(t)$ is uncorrelated from both $X_1(t)$ and $X_2(t)$.

Correlated Poisson jump processes

The jump times of two jump diffusion SDEs as presented in (2.35) can also be correlated. To model the correlation between two Poisson distributed jumps, $J_1(t)$ and $J_2(t)$, three Poisson distributed jumps $n_1(t)$, $n_2(t)$ and $n_3(t)$, with jump rates λ_1, λ_2 and λ_3 are used [54]. $J_1(t)$ and $J_2(t)$ are defined as:

$$J_1(t) = n_1(t) + n_3(t), \tag{2.38}$$

$$J_2(t) = n_2(t) + n_3(t). \tag{2.39}$$

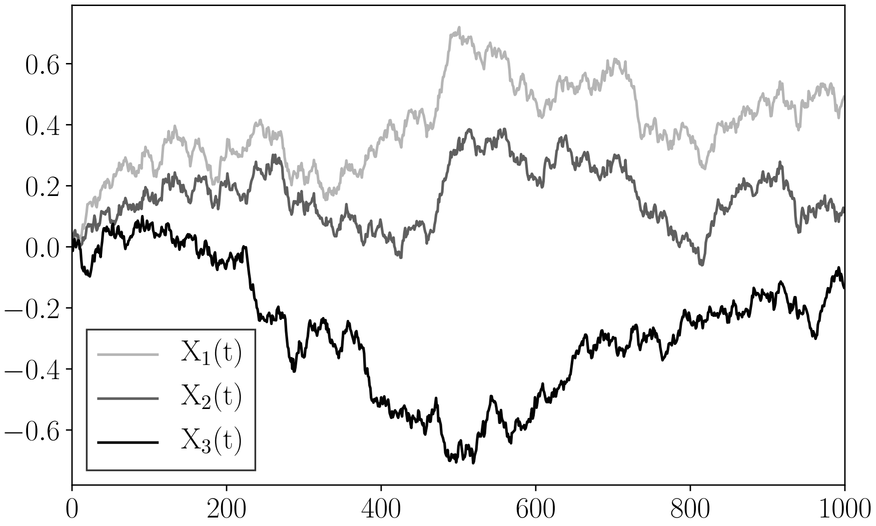

Figure 2.8: Three OU SDE processes. $X_1(t)$ and $X_2(t)$ are simulated with correlated Wiener processes, where $\rho_W = 0.8$. $X_3(t)$ is independent from the other two processes.

Thus, the mean of the two Poisson jump processes is:

$$(\lambda_i + \lambda_3)dt, \quad i = 1, 2. \tag{2.40}$$

Their covariance is λ_3 and their correlation is:

$$\rho_J = \frac{\lambda_3}{\sqrt{(\lambda_1 + \lambda_3)(\lambda_2 + \lambda_3)}}. \tag{2.41}$$

Figure 2.9 shows three example OU SDE processes with jumps. Processes $X_1(t)$ and $X_2(t)$ are simulated with the jumps correlated with the correlation $\rho_J = 0.5$. Thus, some of the jumps in the two processes occur at the same time. $X_3(t)$ is independent from $X_1(t)$ and $X_2(t)$.

In Section 3.4, this method to correlate both two Wiener and two Poisson jump processes is utilized to model the correlation between the active and reactive power consumption of loads.

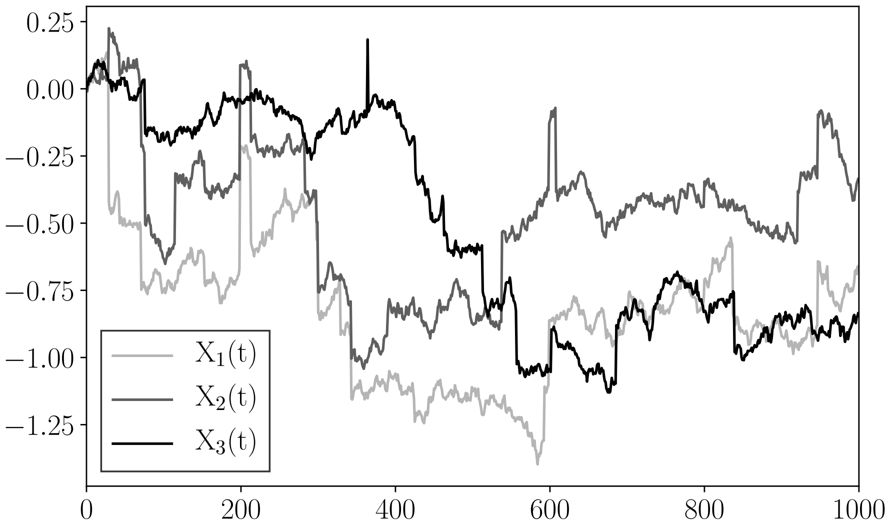

Figure 2.9: Three example OU SDE processes. $X_1(t)$ and $X_2(t)$ are simulated with correlated Poisson processes, where $\rho_J = 0.5$. $X_3(t)$ is independent from the other two processes.

CHAPTER

THREE

APPLICATIONS

Randomness and uncertainty has always been present in power systems. However, it is usually not considered in conventional power system models. With increasing integration of intermittent renewable energy, the uncertain variations in power system can no longer be neglected and have to be modeled.

In this section the stochastic modeling methods, presented in Chapter 2, are utilized to model a few of the potential sources of volatility in power systems. All modeling efforts are supported by measured data. The modeling of wind speed is discussed in Section 3.1, solar irradiance in Section 3.2, tidal current speed in Section 3.3 and loads in Section 3.4.

3.1 Wind generation

During the 20th century wind plants from small scale plants, for farm use, upto large utility scale plants were developed and deployed. However, it wasn't until in the 21st century that serious development focus was put into wind generation, sparked by the increasing demand for renewable energy. In the last few years onshore wind power has become one of the most important sources of renewable power generation. Meanwhile, offshore wind power is only taking off and is expected to grow rapidly in the next few years. For example, in Ireland the instantaneous wind generation can be up to 65 % of the total demand and the system operator is planning to increase this limit to 95 % by 2030 [55]. However, this growth comes with drawbacks. The power generated by a wind turbine depends on the weather conditions which makes it a highly volatile power source. In order to ensure a reliable and secure operation of the grid, it is essential to model the source of such a volatility, i.e., the wind speed. The existing literature does not provide a general method to synthesize continuous dynamic wind speed models that are adequate for the transient stability analysis of power systems. The work presented here aims to address this issue by developing continuous-time wind speed models that precisely reproduce the statistical properties of actual measurement data.

3.1.1 Literature review

The Probability Density Function (PDF) and Autocorrelation Function (ACF) that best describe the wind speed variability depend on the location and the time frame [56, 57, 58, 59, 60, 61, 62]. Commonly, wind speed has a PDF that is shifted to the left and tails heavily to the right. This is because, in most areas, strong extreme winds are rare, while moderate winds are quite common. The most widely used PDF for wind speed is the two-parameter Weibull distribution. However, a wide range of distributions have been proposed in the literature to fit the PDF of wind speed at a specific location [56, 57, 58].

The ACF of wind speed is characterized as an exponentially decaying function over the first 12 hours for hourly averaged data and then settles to zero or a value bigger than zero or shows damped periodic fluctuations due to daily variations [61, 62, 17]. However, if the data is sampled more frequently and/or not averaged, fast wind speed variations change the shape of the ACF. Such short-term wind speed variations, e.g., turbulence and gusts, typically occur within a 10 minute time frame and result in the ACF initially decreasing rapidly before settling to the same slope as the hourly data [38, 63]. This kind of ACF can be well described as a weighted sum of decaying exponential functions.

A wide range of wind speed models are available in the literature. Most of the literature has focused on the forecasting of wind speed and the modeling of the forecast error. Discrete Autoregressive Moving Average (ARMA) models are the most common type found in the literature. These models have been widely used for wind speed forecast error modeling and short-term forecasting [41, 42, 43, 64, 65]. They are well-established and offer comprehensive tools to fit the model to data and reproduce both the PDF and ACF of wind speed data. Markov chains of first order and higher have also been widely used to model wind speed [66, 67]. Additionally, physical models that use meteorological information have been widely used to predict the long-term wind speed [68]. Both ARMA models and Markov chains are discrete and have a fixed time step that must match the sampling interval of the available data. This constraint prevents using such models for transient stability analysis, for which continuous wind speed models are required.

In recent years, the use of SDEs for wind speed modeling has gained popularity. SDEs appear more suitable than classical discrete time-series approaches as they are intrinsically continuous with respect to time and thus, they can better reproduce the transient fluctuations of wind speed. More importantly, SDEs are not constrained to use the sampling time step of the original measurement data. Finally, power systems are typically formalized as a set of differential algebraic equations which allow readily incorporating SDEs.

In the literature, SDEs have been used for wind speed forecasting [10, 11]; modeling the volatility of wind power generation [19, 69, 25]; and power system stability analysis [20]. However, the SDE-based wind speed models that have been presented so far in the literature fail to capture either the PDF, the ACF, or both [19, 20, 25, 70]. In [15, 17, 71], SDEs with an arbitrary PDF are presented but are limited to a strictly exponentially decaying ACF.

To address this, two attempts at modeling wind speed are presented in this thesis. First, as presented in [38], Method I presented in Subsection 2.3.1 is used to build wind speed models. This is discussed in Subsection 3.1.2. This work is followed up by Method II proposed in [72]. This method is an improvement compared to Method I as it is more systematic and straight forward. The use of Method II to model wind speed is discussed in Subsection 3.1.3.

3.1.2 Wind speed modeled with Method I

In [38], Method I is used to model wind speed with a hourly and minutely resolution. In this section a part of the results published in [38] are presented. A comparison is provided of hourly and minutely wind speed data and it is demonstrated that a construction method that can produce wind speed models with a non-exponentially decaying ACF is necessary. It is established that the Continuous-Time ARMA (CARMA) construction approach (Method I) presented in Subsection 2.3.1 can accurately capture the properties of hourly and minutely sampled wind speed data.

Wind speed data

The wind speed measurement data used in this section were provided by Met Éireann [73]. The wind speed measurements were gathered at Valentia Observatory in Kerry. The data consist of minutely and hourly averaged samples over a one month period.

The PDFs for the hourly and minutely data are shown in Figure 3.1. The lower wind speeds are slightly more prevalent in the hourly data while the minutely sampled measurement data has a flatter PDF. An hourly sampling is sufficient to capture the PDF of the wind speed as the difference between the two PDFs is minimal.

Hourly sampled data does not capture fast variations in the wind speed that are visible in the minutely data. These short term variations in the wind speed result in a fast drop in the ACF within the first few minutes. After the first 20 minutes, the ACF settles to the same slope as the ACF of the hourly data (see Figure 3.2). Models based on hourly data generate processes with lower fluctuations than those that are observable in the actual wind speed.

Simulation results

The wind speed is modeled to fit the data presented here above using Method I presented in Subsection 2.3.1. The PDFs presented in [17] are fitted to the data

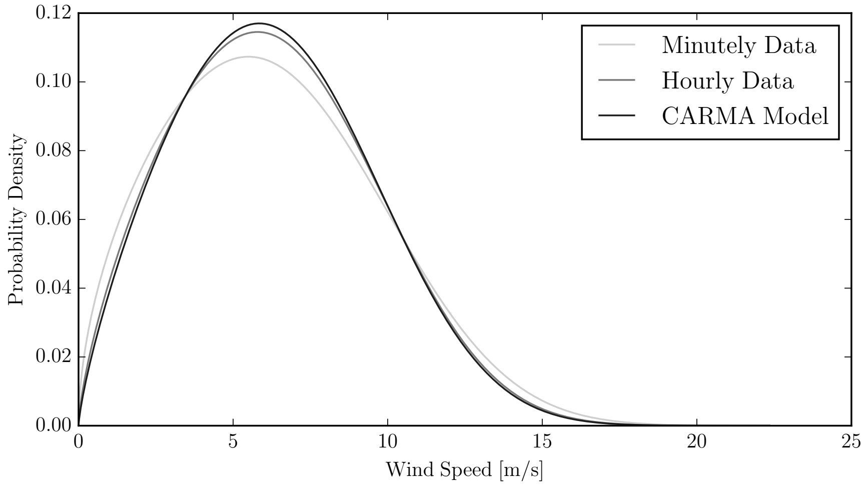

Figure 3.1: Comparison of PDFs of the wind speed data gathered hourly and minutely in the Valentia Observatory, Kerry, Ireland [73]. The CARMA model PDF is the average of 1,000 simulations of the wind speed model based on the minutely data.

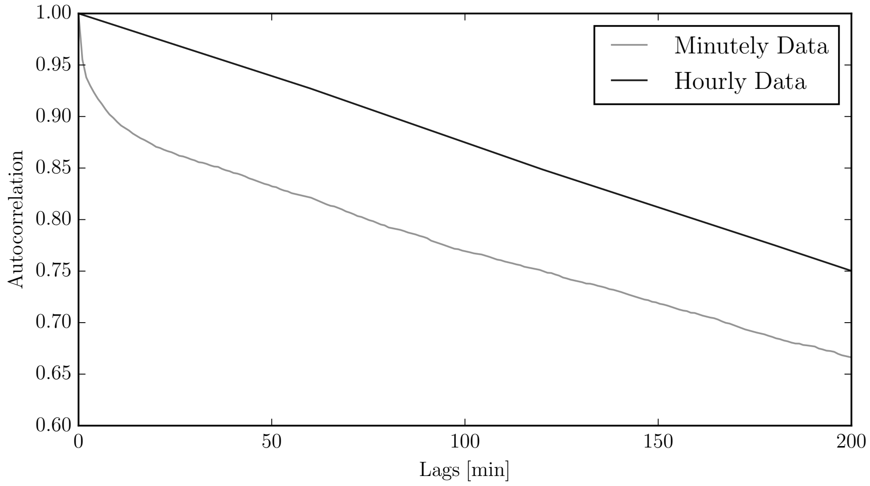

Figure 3.2: Comparison of ACFs of the wind speed data gathered hourly and minutely in the Valentia Observatory in Kerry, Ireland [73].

sets and the Kolmogrov-Smirnov test is used to determine which of the PDFs best fits the data. The best fitting PDF is the Gamma distribution with the parameters presented in Table I in [38]. The model is simulated 1,000 times producing one month of minutely data. The resulting PDF for the 1,000 simulations is shown in Figure 3.1. The CARMA-based model has a PDF where low wind speeds are marginally more likely.

The average ACF of the $1,000$ generated processes and the ACF of the minutely data are shown in Figure 3.3. The CARMA(2,1) model captures the ACF of the minutely data for lags of up to 20 minutes. Its ACF diverges from the ACF of the data over longer time periods. This is sufficient if the wind speed model is intended for angle and voltage stability analysis of power systems. A higher order CARMA model is required to effectively capture the ACF for higher lags.

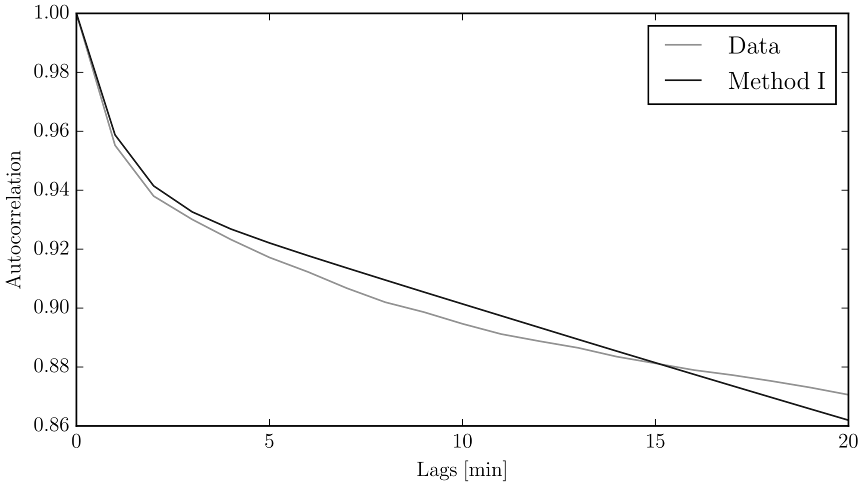

Figure 3.3: Average ACF of the $1,000$ CARMA processes modeled based on minutely data gathered at Valentia Observatory, Kerry, compared to the actual ACF of the data.

This method is able to model more wind speed time-series then the method presented in [17]. However, the conversion from ARMA to CARMA can become more complex as higher order models are required. Additionally, having to always find the ARMA model first makes the modeling procedure time consuming and non-intuitive. Therefore, a more straight forward systematic method to build SDE-based wind speed models based on measured data is proposed in [72].

3.1.3 Wind speed modeled with Method II

In [72], Method II as presented in Subsection 2.3.2, is used to model measured wind speed time-series having sampling rates from 1 second to 1 hour. The data sets modeled are presented in Table 3.1. Further details on the measured wind speed data can be found in [73, 74, 75] as all the data sets used are available open source.

Table 3.1: The wind speed data sets modeled using Method II.

#	Sampling rate	Averaged	Duration	Location
1	1 hour	Yes	3 years	Mace Head, Galway, Ireland
2	1 hour	Yes	3 years	Malin Head, Donegal, Ireland
3	10 minute	Yes	1 year	Ashburnham, Massachussetts
4	10 minute	Yes	1 year	Orleans, Massachussetts
5	1 minute	Yes	1 month	Johnstown, Wexford, Ireland
6	1 minute	Yes	1 month	Oak Park, Carlow, Ireland
7	1 second	No	1 month	Tracy, California

The fitting procedure involves fitting the function in (2.34) to the ACF of the data as well as identifying a PDF that best captures the probability distribution of the data. Full advantage is taken of the flexibility of the memoryless transformation as two methods to define the PDF are utilized: (1) fit an analytical PDF to the data; and (2) find a numerical estimated PDF.

ACF parameters

Figure 3.5 shows the autocorrelation for data set 1. To capture this ACF using Method II presented in Subsection 2.3.2, (2.34) has to be fitted to the ACF. This can be done with any typical curve fitting algorithm. In this work, a non-linear least squares method, included in the Python package SciPy, is utilized. The number of decaying exponential and/or damped sinusoidal functions used to fit the ACF can most often be estimated visually or, if not, by trial and error. The ACF of data set 1 can be captured with the weighted sum of two exponential functions. Further details on the fitting procedure are provided in [72]. There, in Table 4, the parameters for the fitted ACFs of all the data sets presented in Table 3.1 are shown. In the table, it is implied that $\omega_i = 0$ if not provided.

PDF parameters

Figure 3.4 shows the PDF of data set 1. The PDF of the wind speed is imposed using the memoryless transformation as discussed in Subsection 2.3.2. The PDF can be defined in two ways, analytically or numerically. The latter approach is to be preferred if the wind speed distribution is irregular or has two peaks. Further discussion on these two approaches to define the PDF are presented in [72], and there in Table 4 the fitted analytical PDF parameters are presented.

Simulation results

Method II is coupled with the data-fitted parameters from Table 4 in [72]. Combined together, they make wind speed models for the data sets described in Table 3.1. These models are used for generating synthetic wind speed trajectories whose statistical properties accurately reproduce those of the actual wind speed data sets.

Synthetic models are simulated to produce N data points with the time step h (values for N and h are shown in Table B.1 in [72]). To illustrate the ability of the models developed using Method II to reproduce the statistical properties of the original data, the PDF and ACF of the synthetic processes are compared with those of the data sets. First the results of such comparisons for data set 1 are discussed in detail and then an overview is provided of the results for data sets 2 to 7.

The PDF and ACF results for data set 1 are shown in Figure 3.4 and 3.5, respectively. In Figure 3.4, the histogram of data set 1 (in gray) is compared to the results for the generated process using the analytical PDF (solid line) and numerical PDF (dashed line). Both the analytically and numerically defined PDF are well captured by the SDE-based models. In this case the analytical PDF is likely the best option.

Figure 3.6 compares analytical, numerical and data-based PDFs for data sets 2 to 7. For data set 6, the analytical PDF gives a good fit to the probability distribution of the measurements. For the remaining PDFs, however, that is not the case. For data sets 2-5 and 7, in fact, the top of the PDF is uneven, i.e., it is wider or narrower than what can be reproduced through the analytical PDFs. In these cases, the numerically defined PDFs provide better approximations. These PDFs can, in principle, also be approximated through a combination of analytical

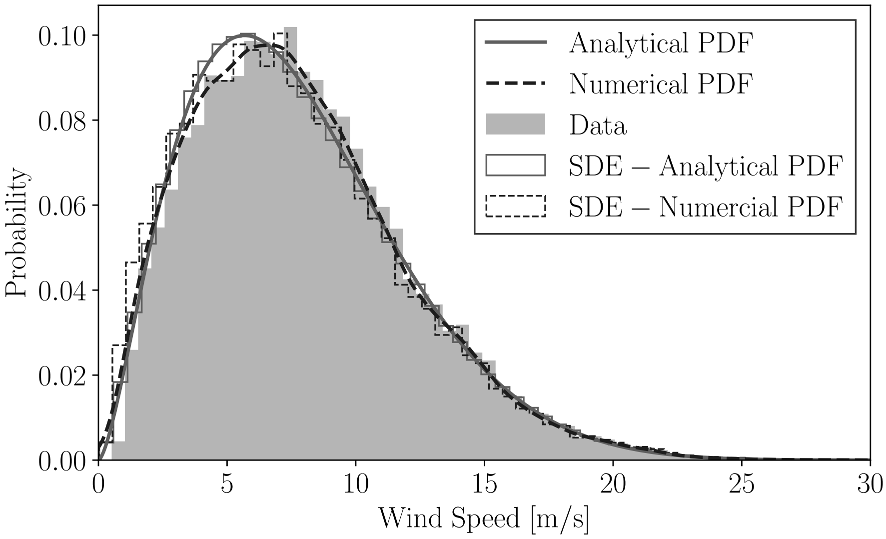

Figure 3.4: Histogram of the data, fitted analytical and numerical PDFs and histogram of the simulated SDE with the analytical and numerical PDF for data set 1.

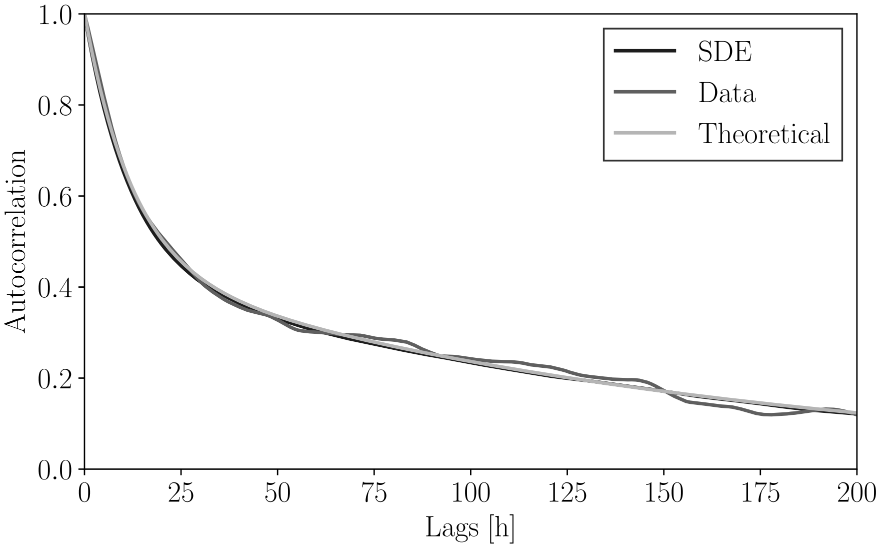

Figure 3.5: ACF of the data, fitted theoretical ACF and ACF of the simulated SDE model for data set 1.

PDFs, e.g., a superposition of Gaussian distributions. However, the numerical approach is simple, general and yet very accurate.

Figure 3.5 shows the ACF of data set 1, the fitted theoretical function and the ACF of the wind speed trajectory generated by the proposed SDE-based model.

The latter consists of the weighted sum of two decaying exponential functions and captures well the ACF of the data.

Figure 3.7 compares analytical and data-based ACFs for data sets 2 to 7. Results clearly show that the ACF is highly dependent on the sampling rate as the ACFs have different shapes for different sampling rates. For example, data sets 5 and 6 show two different sections, one in the time lags that ranges from 0 to 5 minutes, and another one for time lags larger than 5 minutes. The ACF of data set 2 shows a poorly damped sinusoidal mode with a period of 24 hours. The proposed superposition approach is able to reproduce all these different shapes of wind speed ACFs as a weighted sum of exponential and sinusoidal functions.

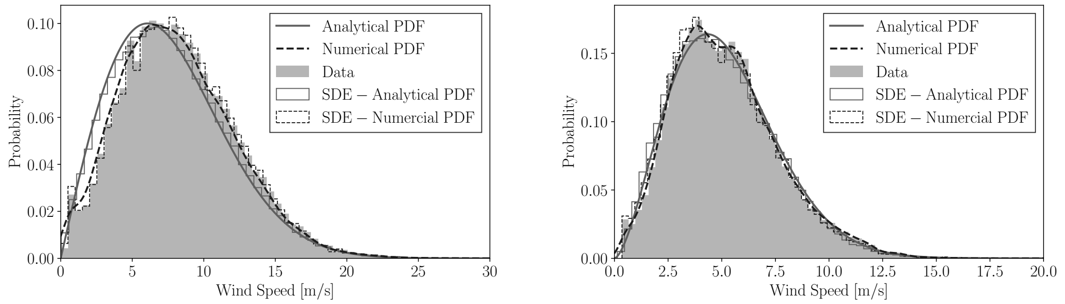

(a) Data set 2 **(b)** Data set 3

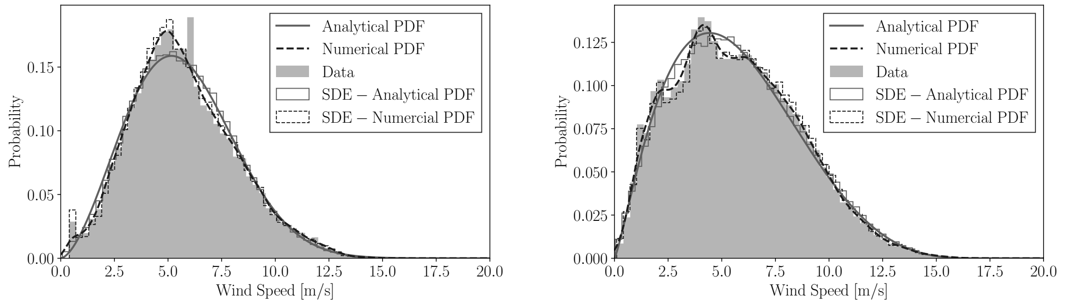

(c) Data set 4 **(d)** Data set 5

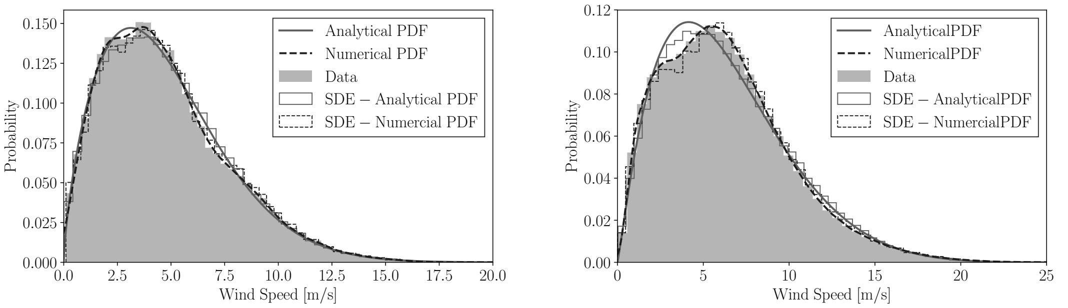

(e) Data set 6 **(f)** Data set 7

Figure 3.6: Histograms of the data, fitted analytical and numerical PDFs and histograms of the simulated SDE with the analytical and numerical PDFs for data sets 2-7.

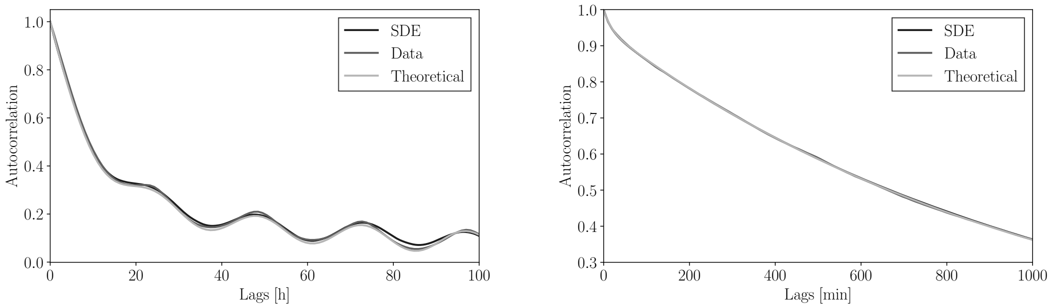

(a) Data set 2 **(b)** Data set 3

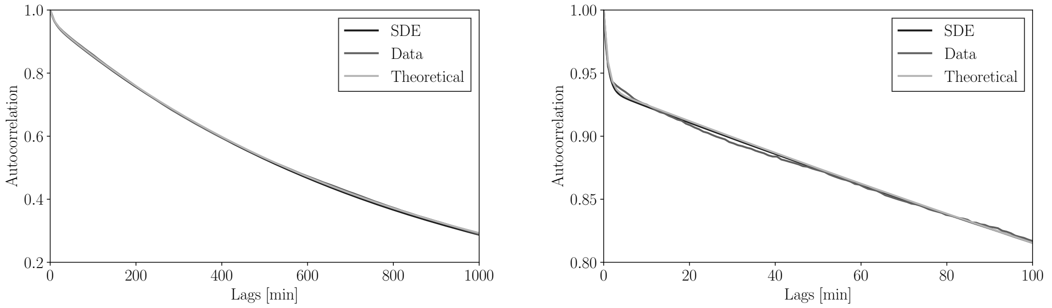

(c) Data set 4 **(d)** Data set 5

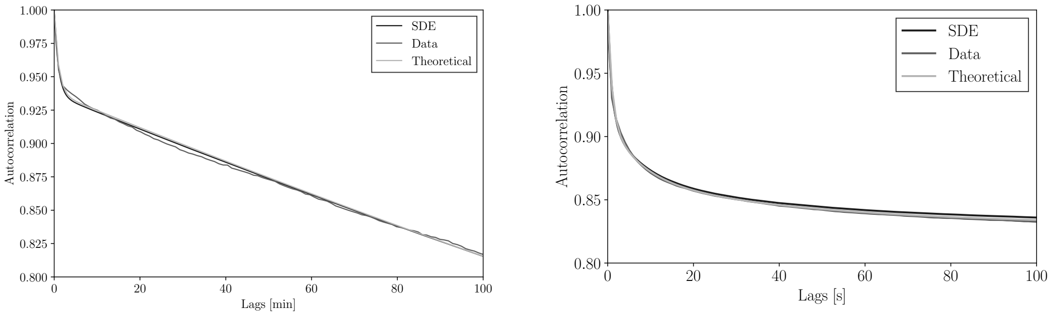

(e) Data set 6 **(f)** Data set 7

Figure 3.7: ACFs of the data, the fitted theoretical ACFs and the ACFs of the simulated SDE model for data sets 2-7.

3.2 Solar generation

Various forms of solar energy have been utilized, e.g. solar heat, solar Photovoltaic (PV) and solar thermal. The technology that has gained the most popularity is solar PV. PV conversion is the direct conversion of sunlight into electricity without any heat engine to interfere. The fist practical PV generator was installed in 1958 on the Vanguard satellite. In the last three years the installed capacity of solar

PV generation has doubled. This makes solar PV one of the fastest growing energy source in power systems worldwide [76]. Solar generation is renewable and eco-friendly but also highly volatile due to the position of the sun and clouds changing [77]. The impact of solar generation fluctuations on the dynamic behavior of power systems has not been thoroughly investigated and remains a relevant research question. Accurate models are required to represent the solar irradiance fluctuations in power system simulations. This modeling need is addressed in this section and the results presented in [78] highlighted.

3.2.1 Literature review

The output of PV solar power plants naturally changes throughout the day because of the daily path the sun follows across the sky. During sunrise and sunset the output of the PV plant will change by about 10 % in just 15 minutes. The daily sun path can be easily and accurately predicted. On the other hand, PV power plants are also a significant source of intermittency due to cloud coverage. The change in solar irradiance caused by cloud movement can be over 60 % of the peak irradiance within a few seconds [79]. These variations can be smoothed and their transient effects minimized if a large PV power plant or if an aggregated model of several geographically distributed plants is considered [77]. However, if a single PV power plant covers a relatively small area, e.g., in micro-grid applications, its power output fluctuations have to be properly modeled [14].

Based on the discussion above, solar irradiance variations can be divided into a deterministic component and a stochastic one. The deterministic component is the variations at a minutely or hourly scale due to the daily apparent movement of the sun. This trajectory can be accurately predicted based on location, time of year and day using clear-sky irradiance models [80, 81]. The stochastic variability is dependent on the cloud coverage and can be expressed using the clear-sky index (the ratio between the global solar radiation and the corresponding clear-sky radiation).

In the dynamic analysis of power systems with PV generation, the solar irradiance is either assumed to be constant [82, 83] or to vary with random steps

[84, 85, 86]. These models do not capture the actual intermittency of the solar irradiance. Measurement data has to be utilized to build more accurate models.

In [87], the solar irradiance variability is modeled by combining a Poisson jump process and an ARMA model. SDEs with jumps are defined in [14] for modeling the clear-sky index. Both these methods define model parameters based on measurements. However, these models do not adequately capture the volatility of the solar irradiance in the seconds to minutes time scale.

In this section a novel SDE model coupled with two jump diffusion processes is presented for modeling the jumps in the solar irradiance caused by cloud movements. This model is also compared to three models from the literature [14, 86, 87]. Before presenting the modeling approaches in Subsection 3.2.3 some background on the modeling of solar irradiance is discussed in Subsection 3.2.2.

3.2.2 Modeling of solar irradiance

This section presents the procedure to identify the deterministic and stochastic part of the solar irradiance from measurement data. With this aim and for the analysis done here, the solar irradiance data collected by the National Renewable Energy Laboratory (NREL), gathered in Kalaeloa, Hawaii, are used [88]. This data set consists of one year of measurements gathered with a 1 Hz sampling frequency from April 2010 to March 2011. Each day consists of measurements from 5am to 8pm.

Irradiance is a measure of the power of sunlight ($\mathrm{W/m^2}$). The power output of a PV panel is proportional to the solar irradiance that hits the panel. Figure 3.8 shows the solar irradiance measurements over three whole days, with different clouding conditions. The effective Global Horizontal Irradiance (GHI) on the solar panel can be modeled in two parts. The deterministic part, which is the estimated clear-sky irradiance based on the position of the sun and the stochastic part, dependent on the cloud movement.

The temporal variability of solar irradiance, due to cloud coverage, can be modeled through the clear-sky index, k. This is defined as the ratio between the

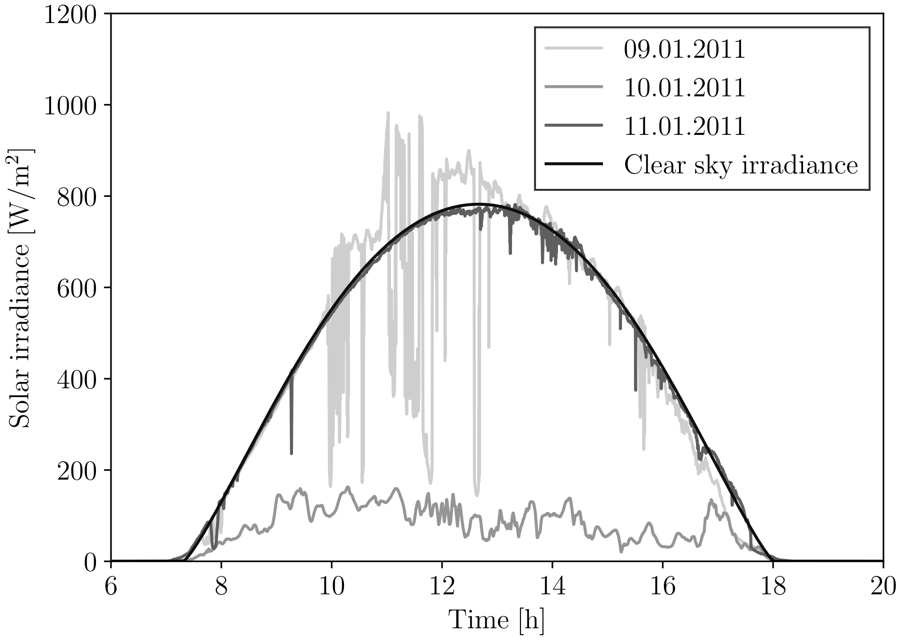

Figure 3.8: Measured solar irradiance [88] for three days and the estimated clear-sky global solar irradiance using (3.2).

measured GHI, G, and the estimated global horizontal clear-sky irradiance, G_C:

$$k = \frac{G}{G_C}. \tag{3.1}$$

The clear-sky index for the three days in Figure 3.8 is shown in Figure 3.9.

The clear-sky global solar irradiance is the maximum irradiance arriving at the earth's surface at a specific location and time, i.e., when no clouds are present. The clear-sky irradiance depends on the site, the solar elevation angle and various atmospheric conditions [81].

A number of models of varying complexity have been suggested in the literature to model the clear-sky irradiance. In this work, a clear-sky model of the same form as the Adnot-Bourges-Campana-Gicquel model is used [80]:

$$G_C = a \cdot \cos(z)^b, \tag{3.2}$$

where z is the zenith angle, which is estimated based on the location and time of day. The parameters a and b are determined by fitting equation (3.2) to the

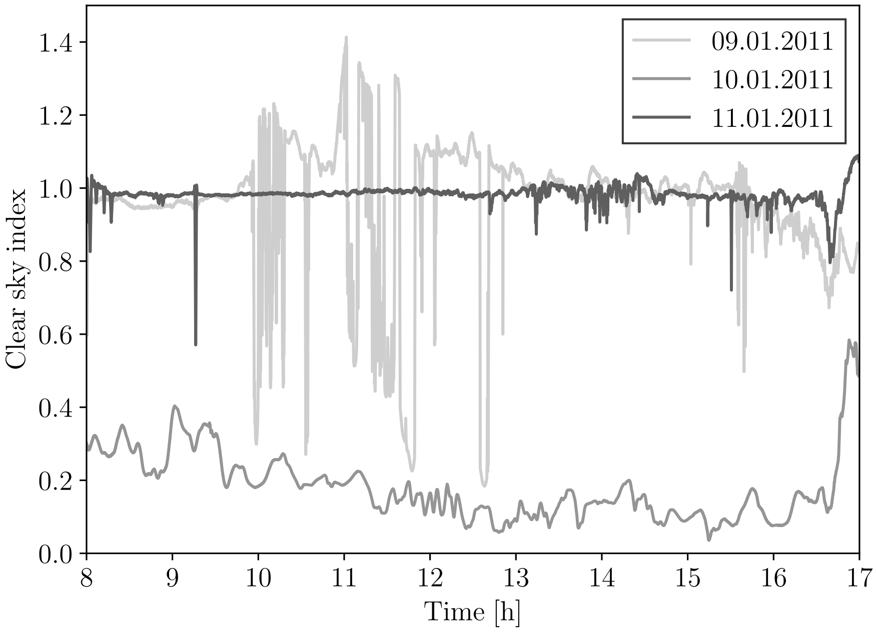

Figure 3.9: Clear-sky index found for the measured solar irradiance data shown in Figure 3.8. In some cases, the clear-sky index becomes bigger than zero during flickering conditions. This is due to cloud enhancement, i.e., sunlight being reflected by surrounding clouds.

measured data for clear-sky days [81]. These coefficients change day by day and are thus found for each clear day of the data set. For the remaining days, a and b coefficients are estimated based on the parameters for the clear days.

The data sets of clear-sky indexes for one day are limited by the sunrise and sunset, that is when $G_C(t) > 0$. The low values of GHI occurring just after sunrise and sunset result in higher uncertainties in the clear-sky index [89]. Because of this, only solar irradiance data from 8am to 5pm are used.

3.2.3 Modeling the clear-sky index with Method III

This section presents four approaches to model the fluctuations of the clear-sky index. The first three models have been presented in the literature to represent solar irradiance fluctuations for the short-term (seconds-to-minutes time scale) analysis of power systems. In [78], the fourth model is presented and the shortcomings of the available models are addressed. An overview of the results presented in [78] are presented in Subsection 3.2.4.

Model I

This model is a simple way to represent the clear-sky index variations in simulation [85, 86]. The variations are represented by a random signal between 1 and 0.4, with 5 second steps. Figure 3.10 shows an example of a simulated clear-sky index obtained with Model I. The range of the jump size and the waiting time between jumps can be changed to fit different locations. However, it is not possible to vary the waiting time between consecutive jumps or to consider the correlation of jump amplitudes.

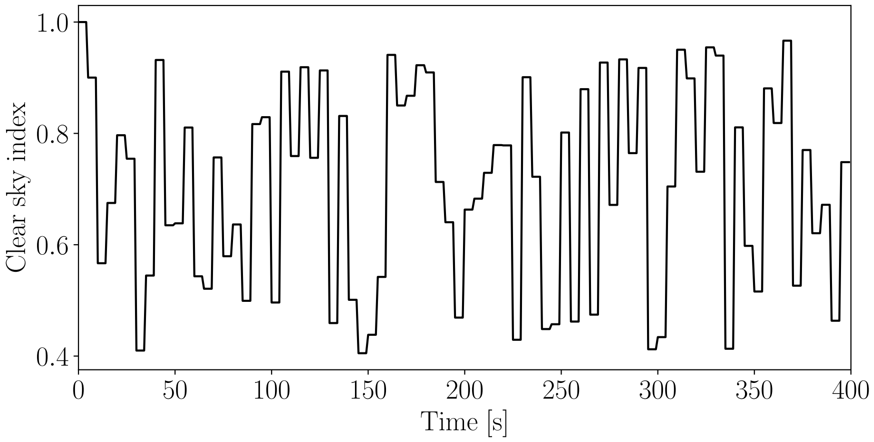

Figure 3.10: Clear-sky index generated with Model I.

Model II

This model, presented in [87], as well as the following two models, split the representation of the clear-sky index into two parts:

1. The baseline of the clear-sky index varying around 1, which models the clear-sky condition.
2. The jumps of the clear-sky index due to cloud coverage.

Model II models the baseline using an ARMA model. Measured solar irradiance data sampled every minute is used to define the parameters of the model. In [87], interpolation is used to convert the model from a time-step of one minute to one second.

The number of cloud events E (jumps) are modeled using a Poisson random variable, with the intensity λ as presented in Subsection 2.3.3. The inter-event waiting time, i.e., the time between cloud events, is itself a random variable with an exponential distribution with the mean μ_W:

$$f_W(t) = \frac{1}{\mu_W}\exp(-t/\mu_W), \tag{3.3}$$

where $t \geq 0$. Finally, the duration T_D of a cloud event is assumed to be exponentially distributed with mean μ_D. A detailed description of how the parameters for the cloud events are derived can be found in [87].

In this work, the ARMA model is substituted with a 1-dimensional Ornstein-Uhlenbeck (OU) Stochastic Differential Equation (SDE), as presented in (2.29) to illustrate the properties of this model. This substitution has no side effect as the variations of the baseline are minimal in the considered time scale.

Figure 3.11 shows an example of a simulated clear-sky index, generated with Model II and with the parameters of the jump process that represent the spring data set, i.e., $\lambda = 7.4178$, $\mu_W = 46.5186$ and $\mu_D = 54.0616$ [87]. In this model, the jump amplitude is the same for all cloud events, which is not realistic.

Model III

This model is presented in [14] and uses a jump diffusion processes as defined in (2.35). In the following, for comparison, it is assumed that the first two terms on the right-hand side of (2.35) represent a 1-dimensional OU process, as in (2.29). $c(t, \eta_J)$ is assumed to be a constant ξ.

In [14], three scenarios are modeled: cloudy, flickering and sunny. For the cloudy and sunny scenarios, no jumps are considered ($\xi = 0$). Then, a non-parametric estimation method is used for estimating the parameters of the model.

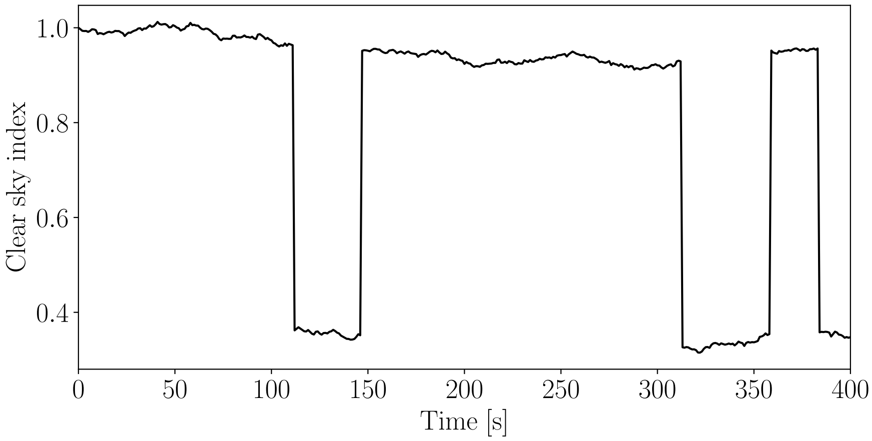

Figure 3.11: Clear-sky index generated with Model II.

Figure 3.12 shows an example of a simulated clear-sky index in the flickering state obtained with Model III. The parameters defined in [14] for the flickering state are used, namely, $\lambda = 0.01$, $\sigma_\xi = 0.028$ and $\mu_\xi = 0.7$. The number of times the clear-sky index data crosses its mean value (~ 0.7) is used for defining the jump rate λ. This assumption clearly prevents modeling any jump that is smaller than the threshold defined by the mean value.

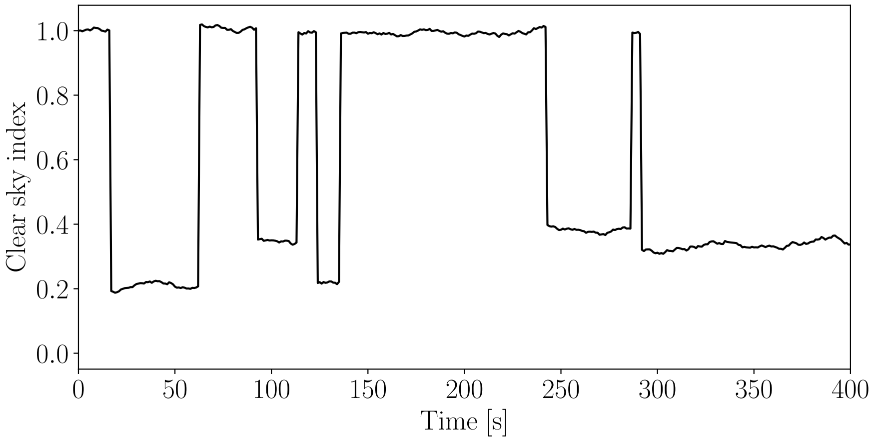

Figure 3.12: Clear-sky index generated with Model III.

Model IV

If the clear-sky indexes generated using Models I - III above are compared with measurement data, two limitations become apparent. Firstly, they are based on the whole data set, not on the flickering cloudy conditions solely. For this reason, these models cannot capture the dynamics of fast variations in the time scale of seconds to minutes. Secondly, small jumps of the clear-sky index are neglected.

Model IV is proposed in [78]. It is aimed at capturing clear-sky index variations for flickering clouding events over the time scale of seconds to minutes. The proposed method utilizes the 1-dimensional OU SDE in (2.29) to represent the clear-sky stochastic variations in the same way as is done in Method II and III. For this model $c(t, \eta_J)$ in (2.35) is set as constant. Since the jumps do not depend on the stochastic variable $X(t)$ and are additive noise they are added directly to the $X(t)$, thus simplifying the numerical integration. The interested reader can find the detailed procedure to integrate jump diffusion processes in [52].

The jumps are modeled as:

$$H(t) = mP(t), \tag{3.4}$$

where m is the jump amplitude assumed to be a normally distributed random number, namely, $m \sim N(\mu_m, \sigma_m^2)$. $P(t)$ is a step function that can get only $0/1$ values, where the number of transitions per period are determined with Poisson distribution with parameter λ. The duration of each jump is determined with a normal distribution $\delta \sim N(0, \sigma_\delta^2)$. In turn, each time $P(t)$ switches from 0 to 1 (or to 1 to 0), it remains constant for a time δ.

Visual inspection of the measured clear-sky index data allows identifying two types of jumps of the clear-sky index:

- **Jump model 1 (JM1):** Big clouds passing over the PV that block most of the solar irradiance.
- **Jump model 2 (JM2):** Small clouds that typically pass by more frequently and only partially reduce the solar irradiance.

The resulting proposed model of the clear-sky index is:

$$k(t) = X(t) + u(t)\,G(t), \tag{3.5}$$

where $X(t)$ is defined by (2.29) and $u(t)$ is a function that defines the duration of a clouding event:

$$u(t) = \begin{cases} 1 & \text{if } u_{\text{start}} \leq t \leq u_{\text{stop}} \\ 0 & \text{otherwise,} \end{cases} \tag{3.6}$$

where u_{start} and u_{stop} are the starting and ending times of the clouding event and

$$G(t) = \begin{cases} -H_1(t) + H_2(t) & \text{if } H_1(t) > 0 \\ -H_2(t) & \text{otherwise,} \end{cases} \tag{3.7}$$

where $H_1(t)$ and $H_2(t)$ are JM1 and JM2, respectively.

The data set presented in Section 3.2.2 is used for evaluating the parameters of the jump models. Five clouding events for each month, for a total of 60 events, are analyzed. This analysis leads to the parameters shown in Table 3.2.

Table 3.2: Range of parameters for the jump models of Model IV defined based on the analysis of 60 clouding events.

Parameters	**Jump model 1**	**Jump model 2**
λ	$0.005 - 0.05$	$0.05 - 0.1$
μ_m	$0.6 - 0.8$	0
σ_m^2	$0.0005 - 0.005$	$0.01 - 0.1$
σ_δ^2	$10 - 50$	$1 - 5$

3.2.4 Simulation results

A cloud event from the data set presented in Subsection 3.2.2 is considered in this subsection to illustrate Model IV and compare its output with Models I to III discussed above. The event occurred on the 1st of December 2010 and its duration is 450 s. The measured clear sky index for this cloud event is shown in Figure 3.13. The analysis of the behavior of the clear-sky index during this event allows determining the parameters for the clear-sky index through Model

Table 3.3: Parameters of Model IV for the clouding event shown in Figure 3.13.

Parameters	Jump model 1	Jump model 2
λ	0.007	0.05
μ_m	0.7	0
σ_δ^2	30	3
σ_m^2	0.05	0.001

IV. Further details on how the parameters of Model IV are set for this cloud event are presented in [78]. The fitted parameters from [78] are presented in Table 3.3.

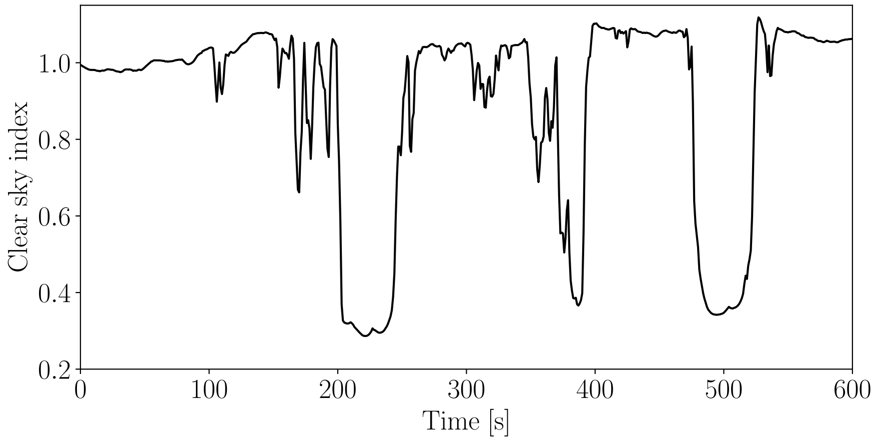

Figure 3.13: Clear-sky index obtained from measurement data [88] and clear-sky model (3.2).

Using Model IV and the parameters of Table 3.3, one can generate synthetic scenarios that are comparable with the measurement data clouding event shown in Figure 3.13. Three sample processes are shown in Figure 3.14. Visual inspection reveals that Model IV is able to reproduce the main features of the clouding event of the measurement data in the time-domain.

In Figure 3.15, the probability distribution of the measured and simulated clear-sky index is compared using histograms for the four different models. Model I does not capture the two peaks in the probability distribution, while Models II and III capture the peaks but not the distribution between the peaks. Model IV is able to better reproduce the clear-sky indexes probability distribution and time-domain behavior when compared to Models I-III.

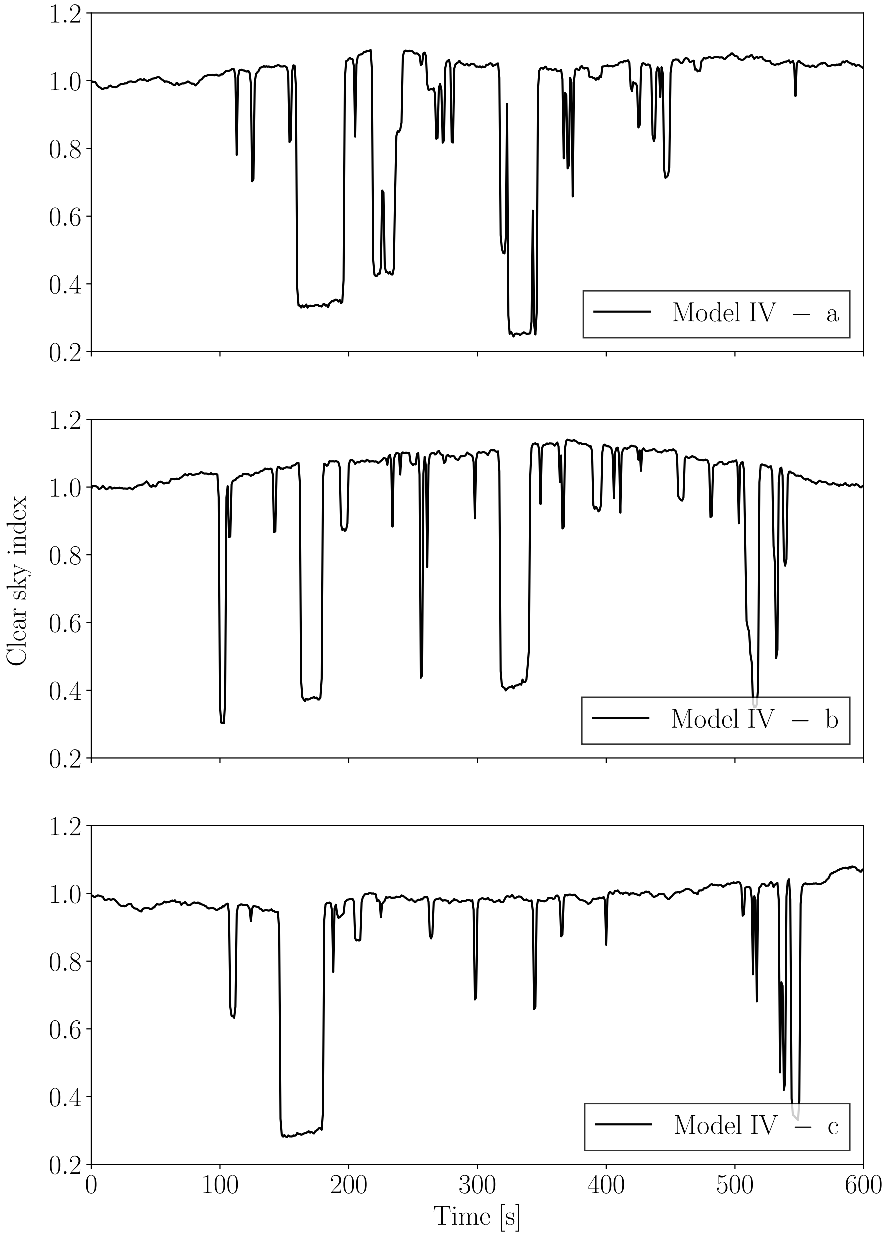

Figure 3.14: Three sample synthetic clear-sky index processes, generated with Model IV and based on the cloud event shown in Figure 3.13.

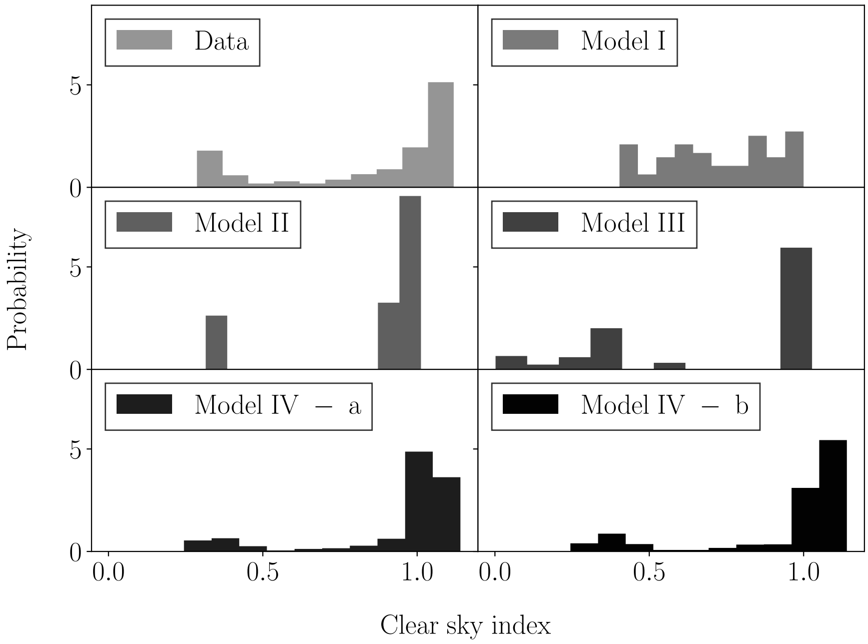

Figure 3.15: Histogram of the clear-sky index during the clouding event in Figure 3.13 and the histogram of the generated clear-sky index utilizing Model I-IV.

3.3 Tidal generation

The potential of marine and tidal currents for electric power generation is widely recognized [90, 91] although multiple techno-economic issues have still to be solved [92]. Historical projects in this area include, for example, the SeaGen project in Strangford Lough, Northern Ireland, the Deepgen project by Tidal Generation Ltd. and a project by ANDRITZ HYDRO Hammerfest deployed at the European Marine Energy Centre (EMEC) tidal test site. Notable recent activities are ongoing within the MeyGen project (Pentland Firth, Scotland) [93] and the Nova Innovation tidal array (Shetland, Scotland), along with operations led by Orbital (Orkney, Scotland) and Sabella (Fromveur Passage, France). These projects demonstrate that tidal stream generation is a viable source of renewable energy.

Tidal currents have a high long-term predictability compared to other prominent renewable energy sources, e.g. wind and solar. However, short-term fluctuations (seconds to minutes) in the current are less predictable. These short-term fluctuations are caused by turbulence and waves and they can negatively impact the power quality and the stability of power systems including tidal generation. In [94], the fluctuations in the power output of the SeaGen tidal generators are studied. There it is shown that the power output of a 600 kW turbine can ramp up/down by 10 kW in a matter of seconds. Experience from the ReDAPT tidal project (ETI, UK) shows levels of power fluctuations far greater, with routine fluctuations, particularly during winter months, of $20-30$ % of rated power per wave-cycle. Thus, understanding and characterizing these fluctuations is essential for the development, design and operation of tidal power plants.

3.3.1 Literature review

Several studies have aimed to characterize the current fluctuations due to turbulance [95, 96, 97, 98, 99]. In [95], the turbulence intensity within the bottom boundary layer at a height of 5 m is studied and is measured to be $12-13$ % in the tidal channel of the Sound of Islay, Scotland. A study conducted within the Puget Sound, Washington state, USA reports the turbulence intensity at approximately the same height as 10 % [96]. In [99], the turbulence intensity is shown to exhibit strong dependence on tide direction (between flood and ebb tides) and water depth. In [97], the current fluctuations with and without waves present are studied based on measurements from the English Channel, France. These studies provide valuable understanding of the statistical properties of these current fluctuations.

In tidal system studies for their integration into power systems, the fluctuations have typically been modeled as purely turbulent [100] or as dominated by waves, in particular swell waves [101, 102, 103, 104]. Swell waves have been characterized as the biggest cause of short-term fluctuations in the tidal power output and multiple publications have addressed the damping of said fluctuations using storage or other additional control [101, 102, 103, 104]. These publications model the swells using the first-order Stokes model coupled with the JONSWAP spectrum [105, 106]. This model is widely used in ocean engineering for modeling wind and swell waves. However, the model is not specifically built to model waves in sites with strong tidal flows, that is where tidal turbines are likely to be installed. Additionally, such models do not consider the coupling of the turbulence and waves. Therefore, these studies might over- or under-estimate the effect of waves on the tidal current and thereby the control/storage needed alongside the tidal turbine.

3.3.2 Tidal generation technology

This section provides some important background on tidal generation as ocean renewable energy sources are generally not as well known as the two other renewable sources discussed here above. Namely, wind and solar.

Various kinds of energy can be extracted from the ocean, e.g. tidal current energy, wave energy and thermal energy. The technology used to harvest the kinetic energy in tidal current is relatively mature compared to the other ocean energy technologies. Tidal generators extract energy from the ocean movement due to the tidal phenomenon. This phenomenon is a result of the changing gravitational pull of the sun and moon in respect to the earth's oceans. It causes large bodies of water to move towards and away from the shore. The tidal movement is site specific. Each location will experience diurnal tides (one high, one low in a tidal day), semi-diurnal tides (two high, two low in a tidal day) or a mixture of the two. Tides can be predicted far in advance and with a high degree of accuracy. This is one of the driving forces for tidal generation development, as it makes tidal generation one of the more reliable sources of renewable energy [107].

The world's first tidal power station opened in 1966, in the Rance river, France [108]. This power plant is of the tidal barrage type, which is a dam-like structure across a bay or a river that is subject to tidal flows. Another form of tidal power is tidal stream generation. It converts the energy of free flowing water into electricity. This technology has gained popularity, over tidal barrages and other tidal generation technologies because they are the cheapest and least ecologically damaging [109]. Numerous types of tidal stream devices have been proposed in the literature, such as horizontal- and vertical-axis turbines and tidal kites. The main research and development focus has been on horizontal-axis turbines [110], with important tidal projects, such as SeaGen in Norther Ireland [111] and more recently MeyGen in Scotland [93] utilizing those. A contributing factor to their dominance is their similarity to wind turbines. This allows for much of the readily available technology, for wind turbines to be reused for tidal turbines. Because of this similarity tidal generation will, for the remainder of this section and in Subsection 3.3.3, be discussed in comparison to wind generation.

The utilization of similar technology for tidal and wind generation systems is not surprising, as both aim to capture kinetic energy from one kind of a flowing mass. However, several important differences are between the two energy sources. One of the main differences being the density of the flowing mass. The density of air is about 1/800 of the density of water. This means the rated current speed can be much lower, between 2-3 m/s, compared to the rated wind speed of a wind turbine. Thus, to get similar power ratings, the tidal turbine rotor size is relatively much smaller. This makes tidal turbines more compact than wind turbines. The density difference between the two flowing masses also impacts the design of the turbine blades.

Another difference is the direction of the flowing mass. For wind turbines, the wind can hit the turbine from any direction. For tidal turbines, however, there are only two possible directions of the current flow, ebb or flood. This affects the design of the pitch angle control for tidal turbines.

In [112], different generator types for tidal turbines are studied and compared. There it is concluded that Permanent Magnet Synchronous Generatorss (PMSGs) are better suited for tidal generation than Double Fed Induction Generatorss (DFIGs). DFIGs are more lightweight and lower in cost, but would require more regular maintenance of the gearbox and slip rings. This maintenance would be more difficult to conduct underwater, than is the case for wind turbines. However, both PMSGs and DFIGs can be used for tidal generation.

This comes to show that the wind and tidal turbine technologies are in most ways very similar. Thus, the main noticeable difference, when it comes to dynamic analysis, is due to the difference in the input signals, that is wind speed and tidal current speed. This subject is discussed in more detail in Subsection 3.3.3

3.3.3 Comparison of tidal current and wind speed

If average values over some minutes are considered the current speed is highly predictable many days or even years in advance. The mean current speed usually has roughly four or eight peaks per day. This can be seen in Figure 3.16.a where an example of measured current speed for Port Mantee, US is shown [113]. Wind power on the other hand will vary with more uncertainty in that minutely to hourly time frame. An example of hourly measured wind speed, collected in Mayo, Ireland can be seen in Figure 3.16.b [73].

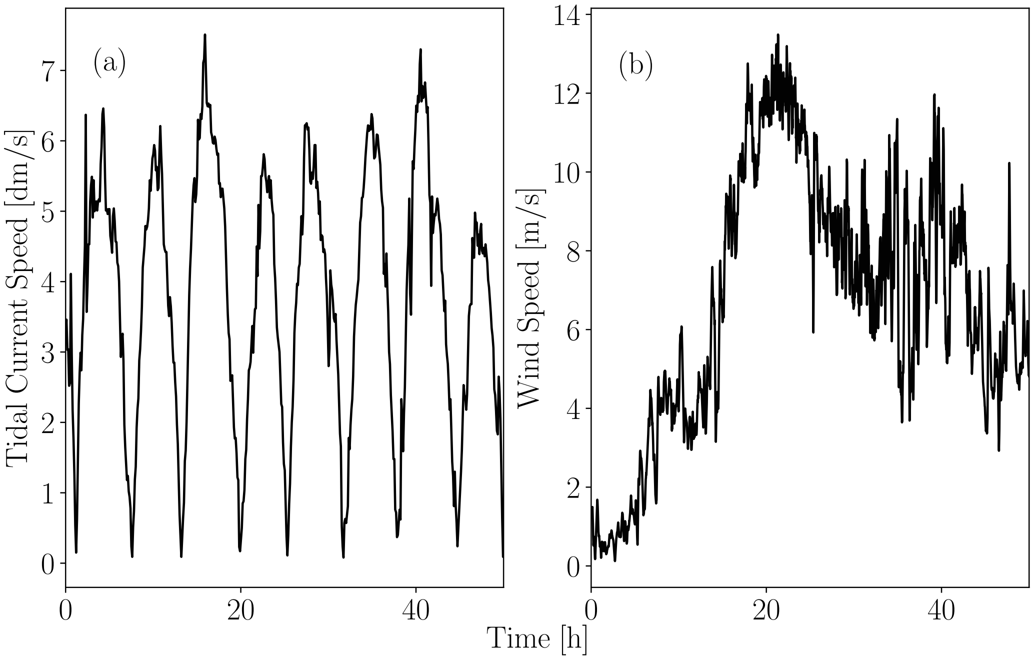

Figure 3.16: Wind speed and tidal current speed measurements averaged every 10 minutes [73, 113].

Wind and tidal current speeds are variable on a shorter time scale as well. In the case of wind speed these short-term variations can be due to gusts or turbulence. The intensity of the turbulence depends on the terrain surrounding the wind power plant. For a land-based wind turbine the normal turbulence intensity would be close to 20 % for wind speed of around 12 m/s [114], while for offshore locations this percentage is expected to be slightly smaller. An example of measured wind speed, with a sampling frequency of 1 Hz, is shown in Figure 3.17.b, measured in Tracy, California [74]. Further details on how these short-term variations in the wind speed are modeled for power system analysis are presented in Section 3.1 and Subsection 4.3.1.

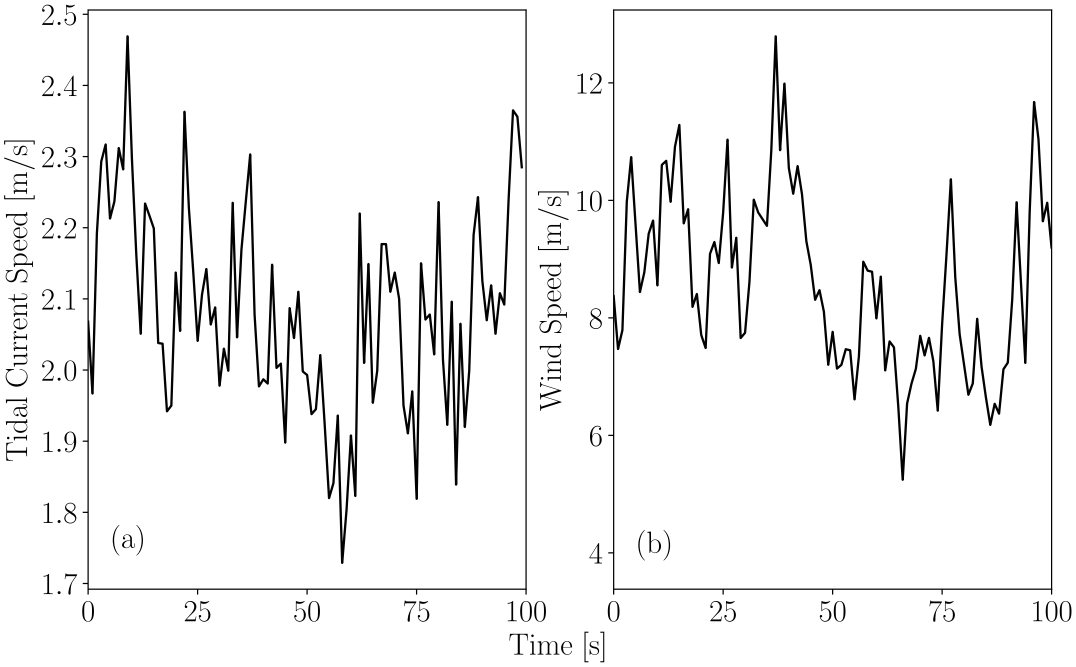

Figure 3.17: Wind speed and tidal current speed measurements with a 1 Hz sampling frequency [74, 115].

The short-term variations in the tidal current are both due to the bottom and side friction and the surface waves. These fluctuations are typically about 10 % of the mean speed [114]. An example of measured tidal current, with a sampling frequency of 1 Hz, is shown in Figure 3.17.a, collected in the European Marine Energy Centre tidal test site in Orkney, UK [115]. In this case the fluctuations are dominated by turbulence.

The tidal current speed can also be subject to wind waves and ocean swells. Wind waves have a relatively short wave length and high frequency. These are caused by local winds. Swells are long wavelength waves that originate in a remote region of the ocean and propagate out of their area of generation. These are considered to have the greatest disturbing effect on the tidal current speed in a tidal turbine, as they travel deep under the ocean surface [102].

3.3.4 Tidal current speed modeled with Method II

This section outlines results from [116] which focuses on modeling the short-term fluctuations in the tidal current. The total tidal current speed is modeled as:

$$u_{\text{tidal}}(t) = u_0 + \eta(t), \tag{3.8}$$

u_0 represents the averaged variations in the tidal current. This value is kept constant in this work but could also be set to model the changes in the current due to the tidal phenomenon. Method II, presented in Subsection 2.3.2 is used to model the short term variations in the tidal current, $\eta(t)$.

Data

This section presents the measured tidal current speed data used to validate the use of Method II to model short-term fluctuations in the tidal current. The current speed data were gathered during the Reliable Data Acquisition Platform for Tidal project (ReDAPT) in the European Marine Energy Centre (EMEC) tidal test site in Orkney, UK. The data is publicly available from [115]. The measurements are collected using a single-beam acoustic Doppler profiler deployed at the nose of the test Deep-Gen IV tidal turbine. It measures the velocity directly along the stream-wise axis. The provided velocity profiles have cell sizes of 0.5 m. The measured data analyzed in this paper is the stream-wise tidal current speed measured 10 m upstream from the turbine at hub height. Further information on field measurement techniques and subsequent data processing are discussed in [99].

Two sets of data are analysed, representing the two following scenarios:

- *Scenario 1*: Short-term fluctuations are exclusively due to turbulence. Waves are not considered.
- *Scenario 2*: Fluctuations are both due to turbulence and waves. The most significant wave height is $H_s = 1.9$ m and the peak period is $T_p = 9$ s.

Further details on each scenario are provided in Table 3.4.

Table 3.4: Details on the Scenario 1 and 2 data sets.

Scenario	**Dates**	**Time**	**Sampling rate**	**Sea state**
1	2014/08/09	14:00-18:40	2 Hz	No waves
2	2014/11/11 2014/11/12	21:00-08:55	4 Hz	Waves

An example of the measured time-series for Scenario 1 is shown in Figure 3.18.a (grey line), where a trend in the tidal current is noticeable. This trend is due to the tidal phenomenon. As the aim is to model the short-term variations (in the seconds to minutes time scale) this trend is removed from the data. To identify the trend the two-sided rolling mean of the time-series is used. The two-sided rolling mean of a time-series y_t is defined as:

$$z_t = \frac{1}{2m+1} \sum_{j=-m}^{m} y_{t-j}, \tag{3.9}$$

where m is the smoothing parameter that defines the window to average over. In this case y_t is the Scenario 1 time-series. The two-sided rolling mean of the measured time-series where m is set to 10 minutes is shown in Figure 3.18.a (black line). The measured stochastic process to be modeled is:

$$x_t = y_t - z_t, \tag{3.10}$$

which represents the measured tidal current speed where the trend has been removed. In this way, the short-term fluctuations of the current speed are 'isolated' as it is shown in Figure 3.18.b. In Figure 3.18.b, it can be observed that the standard deviation of the fluctuations is proportional to the average tidal current. This has also been discussed in the literature where the tidal current turbulence is studied [95, 96, 97, 98]. In Figure 3.18.c, the rolling standard deviation of the current speed fluctuations (gray line) and the scaled down rolling mean ($0.1z_t$) are shown which demonstrates they are somewhat correlated.

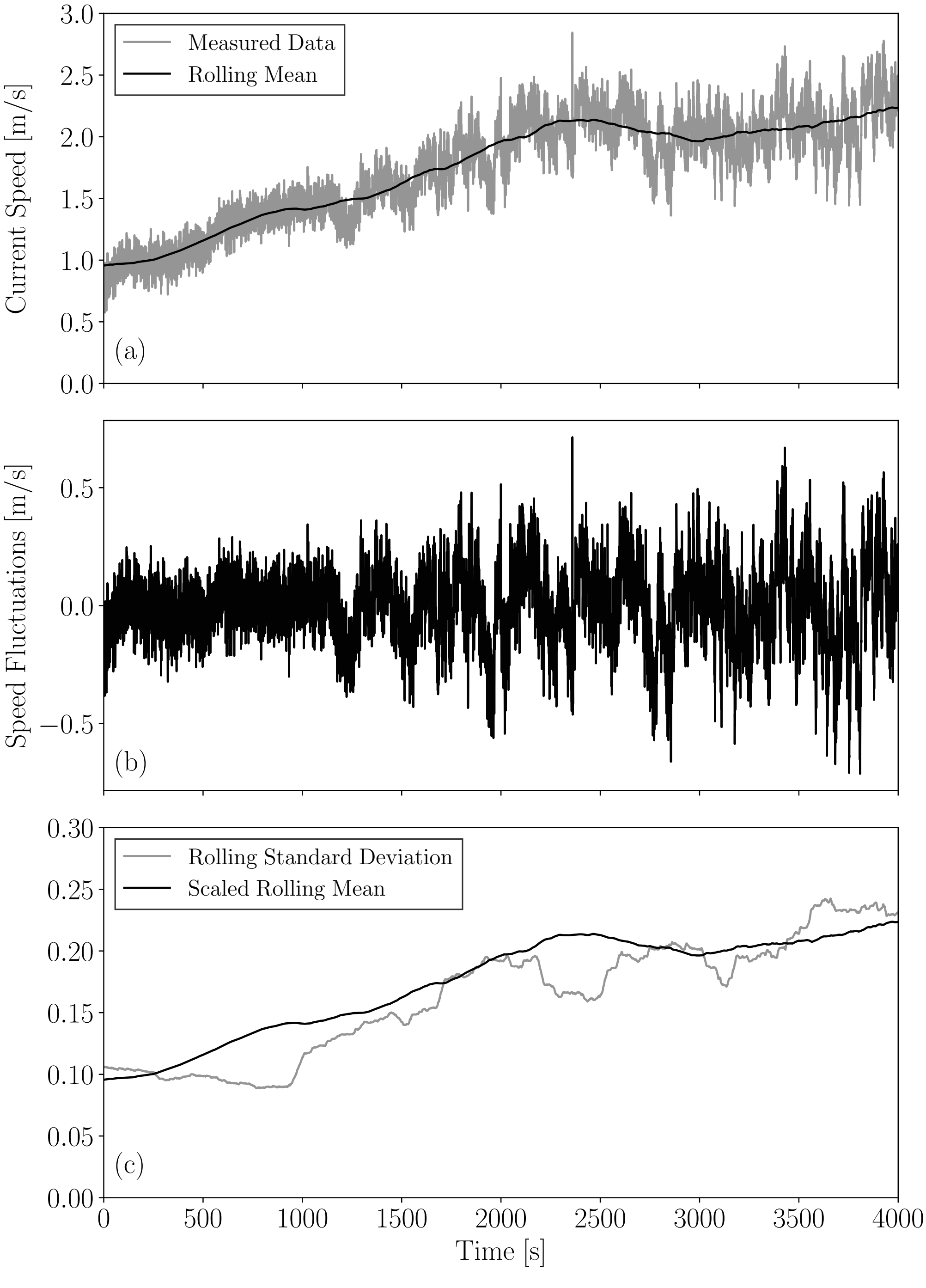

Figure 3.18: (a) Measured stream wise tidal current speed (Scenario 1) and the rolling two-sided mean derived using (3.9). (b) Current speed fluctuations derived using (3.10). (c) Rolling standard deviation and scaled rolling mean ($0.1z_t$).

ACF and PDF parameters

The Method II modeling procedure presented in Subsection 2.3.2 consists in fitting the model to measurement data based on their statistical properties, that is the ACF and PDF. The ACF parameters are found in the same way as presented in Subsection 3.1.3 and in [116]. Table 3.5 shows the fitted parameters for the ACFs for both scenario. In the table, it is assumed that $\psi_i = 0$ if not provided.

Table 3.5: The fitted ACF and PDF parameters for the current fluctuations models of Scenario 1 and 2.

Scenario	ACF Parameters		Standard deviation
1	$w_1 = 0.23$	$\kappa_1 = -5$	$\sigma_X = 0.09266\,u_0$
	$w_2 = 0.32$	$\kappa_2 = -0.2$	
	$w_3 = 0.45$	$\kappa_3 = -0.04$	
2	$w_1 = 0.28$	$\kappa_1 = -5$	$\sigma_X = 0.09702\,u_0$
	$w_2 = 0.18$	$\kappa_2 = -0.2$	
	$w_3 = 0.46$	$\kappa_3 = -0.05$	
	$w_4 = 0.08$	$\kappa_4 = -0.06$	
		$\psi_4 = 0.7$	

In this work, the PDF of the short-term tidal current fluctuations is modeled as Gaussian. In Figure 3.18.c, it is shown that there is a correlation between the mean tidal current speed and the standard deviation of the fluctuations. Hence, the standard deviation is dependent on the magnitude of the tidal current speed. The higher the tidal current speed the higher the standard deviation of the fluctuations in the current [95, 96, 97, 98]. To determine this relationship the mean of the rolling standard deviation as a function of the rolling mean is found as follows:

$$\frac{\sigma_X}{u_0} = \frac{\sum_i^n \sigma_{r_i}/\mu_{r_i}}{n}, \tag{3.11}$$

where μ_{r_i} and σ_{r_i} are the rolling mean and standard deviation respectively for the i-th time frame of the n time frames of data. In this case, the time frame is 10 minutes. In this way, (3.11) can give the relation between the tidal current magnitude u_0 an the standard deviation σ_X. The standard deviation for each measured scenario is shown in Table 3.5. In both cases the standard deviation is slightly less than 10 % of the tidal current magnitude. This value can be subject to the tidal conditions (flood/ebb tides) or the date. This topic is outside the scope of this thesis work.

Simulation results

For Scenario 1 the ACF can be captured through the superposition of three OU processes. In this scenario, the fluctuations are primarily due to turbulence. Thus, no periodicity is identified in the ACF. In Figure 3.19.a, the ACF of the data for Scenario 1 is shown, as well as the fitted ACF function and the ACF of the simulated synthetic time-series derived from the model.

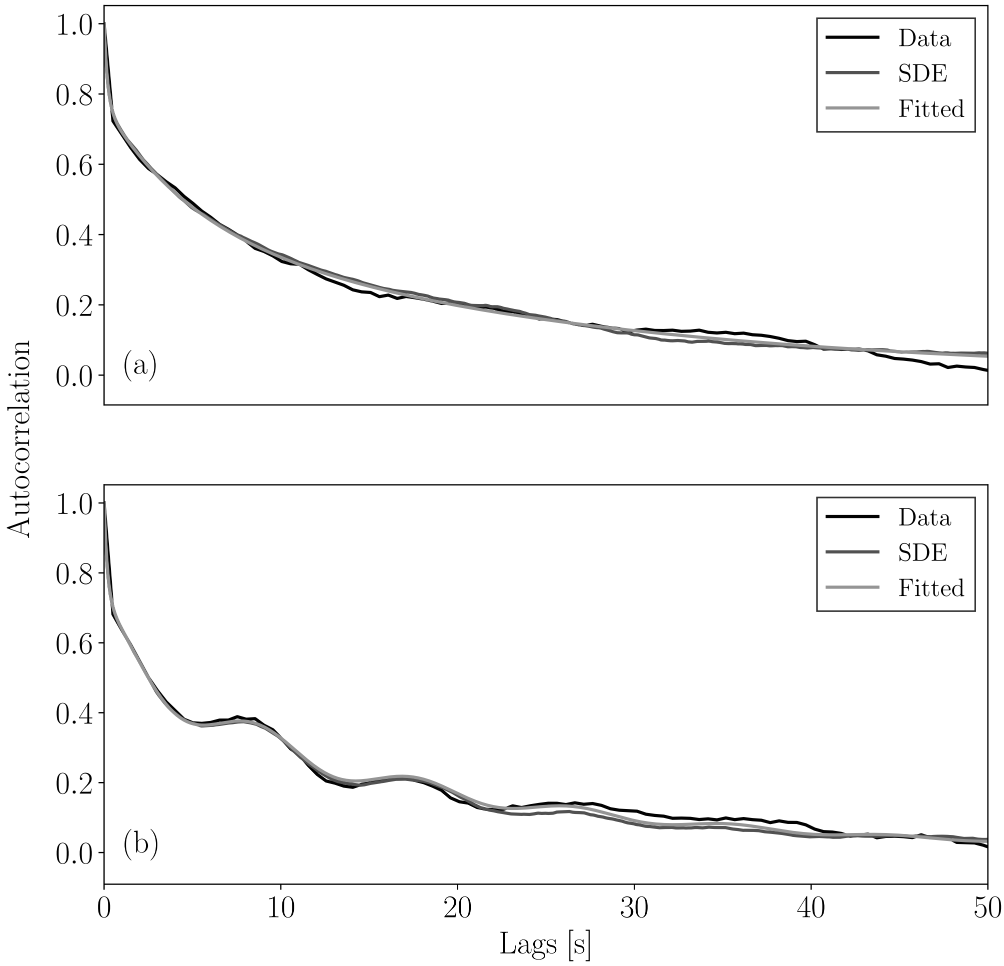

Figure 3.19: ACFs of the data set, the fitted ACF and the ACF of the simulated SDE model for: (a) Scenario 1 and (b) Scenario 2.

For Scenario 2, periodic behavior driven by the waves in the tidal current is observable in the ACF. Thus, in this case, an additional OU process is needed to capture the periodicity. The ACF of the data for Scenario 2, the fitted ACF function and the ACF of the simulated process are shown in Figure 3.19.b.

The behavior of the ACF for Scenario 2 indicates that the waves are periodic with a frequency around 0.1 Hz. In the model built using Method II, the periodicity is set through the parameter $\psi_4 = 0.7$ rad/s presented in Table 3.5. In particular, for Scenario 2, a frequency of 0.11 Hz, which corresponds to a period of 9 s, has been determined. This matches the specified peak period of the measured data.

For both scenarios the model is able to capture the desired ACF. By capturing the ACF the model ensures that the generated stochastic trajectories evolve in time in the same way as the measured time-series.

The power spectral density of a time-series measures the time-series power content versus frequency. It is defined as the Fourier transform of the autocovariance and can be viewed as the frequency-domain equivalent of the autocovariance. Figures 3.20.a-b show the power spectral densities of the two scenarios measured and simulated. The power spectral densities for both scenarios look similar for most frequencies except around 0.1 Hz, where a spike is visible for Scenario 2. This is the contribution of the waves in the power spectral density of the measured time-series. For both scenarios the simulated processes have spectral densities that have a very similar trend to those shown by the measurement data.

The similarity of the two scenarios can be observed also in the fitted ACF parameters in Table 3.5. The weights w_i differ, but the first three κ_i parameters are very similar. The fourth process component for Scenario 2 is modeling the contribution of the wave. Thus, the first three process components can be said to be capturing the turbulence contribution.

3.4 Load

Load power consumption is not fully deterministic. This has led to the proposal of a variety of stochastic load models in the literature. In this section a load model for short-term analysis of power systems, proposed in [117] is presented. Its

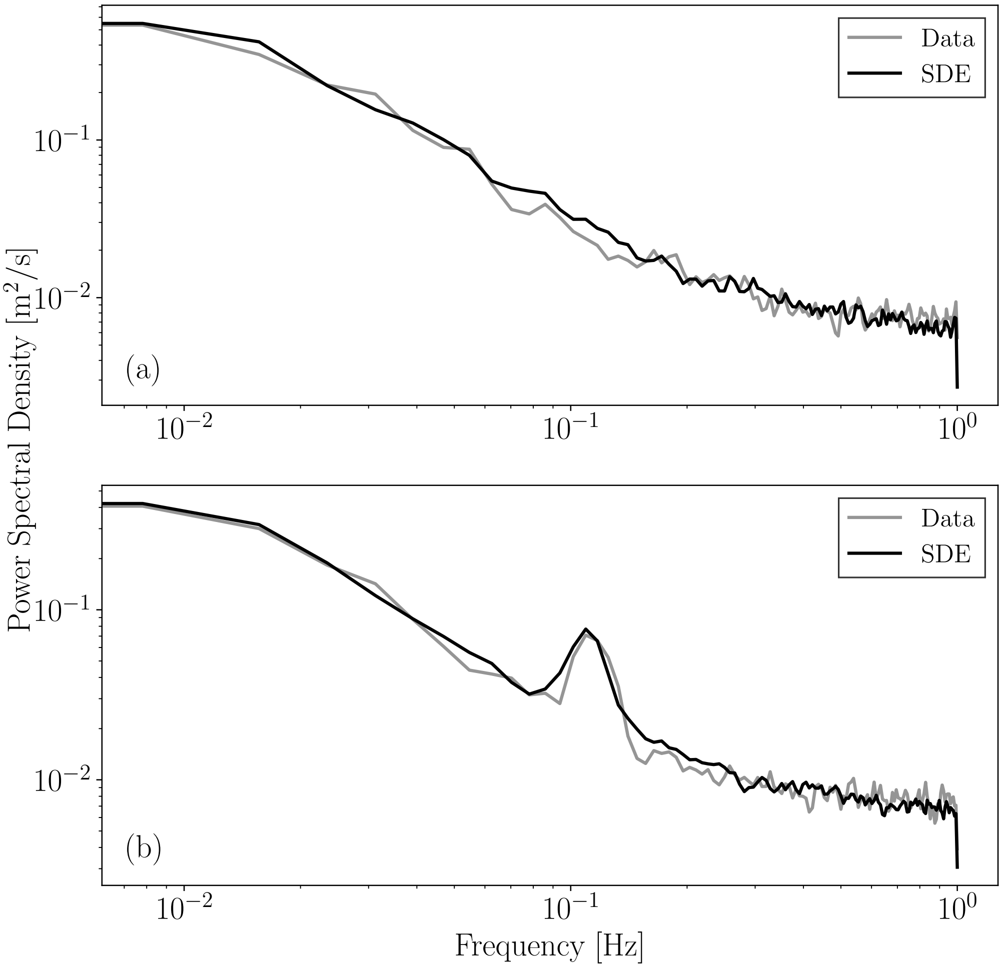

Figure 3.20: Power spectral density for the measured data and the SDE simulated time-series for: (a) Scenario 1, (b) Scenario 2.

novelty is modeling the correlation in the active and reactive power consumption of a load.

3.4.1 Literature review

In power system stability studies loads have traditionally been modeled as deterministic using either static or dynamic models [118, 119]. However, loads often vary in an uncertain manner. Specifically, in the frame of seconds to minutes. Recent relevant studies that consider the short-term uncertainty of loads are as follows.

In [120], the effect of load uncertainty on voltage stability is considered using trajectory sensitivity analysis. Other such probabilistic analysis considering the effect of load uncertainty on the system stability are presented in [121, 122]. In [4] it is shown that important information is lost when only probabilistic analysis of the system is considered for stability analysis. For this reason it is important to model the load uncertainty as a stochastic processes evolving with time.

Load uncertainty can be modeled as a stochastic process in time using SDEs. Several studies have used SDEs for load modeling. A modified exponential recovery model, with a purely diffusion term SDEs, modeling the load uncertainty is utilized in [123]. In [13, 37, 124], Ornstein-Uhlenbeck (OU) SDE processes are used to model the load variations and in [16] OU processes including jumps are proposed for load modeling. However, none of these stochastic models consider the correlation in the active and reactive power.

Figure 3.21 shows an example of active and reactive power measurements obtained with a Phasor Measurement Unit (PMU). The data indicate that there is a clear correlation between the stochastic component and the jump component when it comes to jump time and size in the measured active and reactive power. Thus, the active and reactive power of the load are, at least in some cases, correlated and their correlation needs to be modeled.

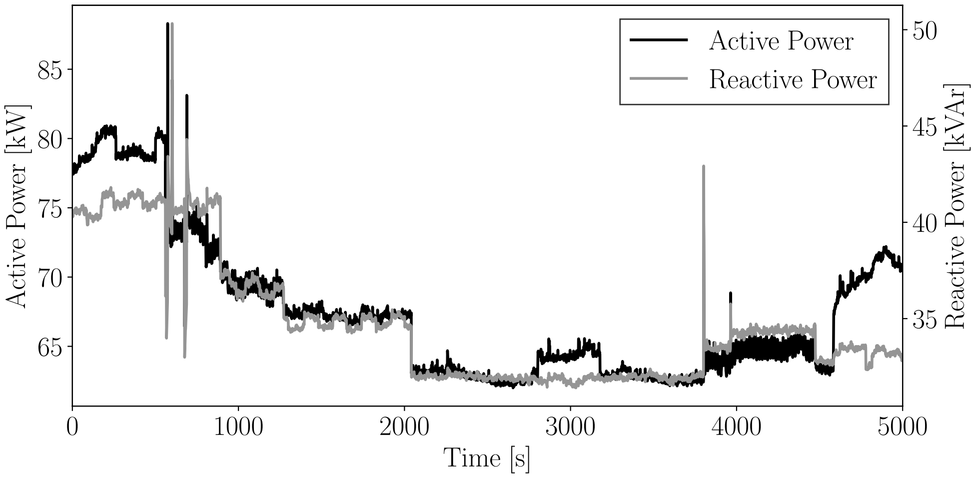

Figure 3.21: Active and reactive power consumption of a load measured with a PMU.

3.4.2 Load modeling with Methods III and IV

The load model presented here, proposed in [117], utilizes both Method III to model jumps in the load consumption and Method IV to model the correlation between the active and reactive power consumption of a load. The SDE-based model, presented in [16], models the load variations using an OU SDE model with jumps. This load model is developed based on the well-known voltage dependent load model. However, it models the active and reactive power independently. The updated load model proposed in [117] utilizes the model proposed in [16] but enables the stochastic and jump component of the active and reactive power to be correlated by using Method IV as presented in Subsection 2.3.4. Thus, the load model is:

$$
\begin{aligned}
p_L(t) &= (p_{L0} + \eta_p(t))(v(t)/v_0)^k, \\
q_L(t) &= (q_{L0} + \eta_q(t))(v(t)/v_0)^k, \\
d\eta_p(t) &= \alpha_p(\mu_p - \eta_p(t))dt + \sigma_p dW_1(t) + \varsigma_p(t)dJ_1(t), \\
d\eta_q(t) &= \alpha_q(\mu_q - \eta_q(t))dt + \sigma_q dW_1(t) + \varsigma_q(t)dJ_2(t),
\end{aligned}
\tag{3.12}
$$

where $p_L(t)$ and $q_L(t)$ are the active and reactive power of the load, respectively, and p_{L0} and q_{L0} are parameters representing active and reactive load powers at $t = 0$. $v(t)$ is the voltage magnitude at the bus where the load is connected and v_0 is the value of this voltage magnitude at $t = 0$.

The model in (3.12) can, through the exponent k define whether the load is a constant power load ($k = 0$), a constant current load ($k = 1$) or a constant impedance load ($k = 2$). The stochastic variability of the load is modeled through the stochastic processes $\eta_p(t)$ and $\eta_q(t)$ which are formulated as SDE jump diffusion processes as presented in Subsection 2.3.3, where α is the mean-reversion speed, μ is the mean and σ is the diffusion component of the OU process (2.29).

The jump amplitudes $\varsigma_p(t)$ and $\varsigma_q(t)$ are normally distributed random numbers, namely $\varsigma_p(t) \sim N(0, \sigma_{\varsigma_p})$ and $\varsigma_q(t) \sim N(0, \sigma_{\varsigma_q})$. They are modeled to have a correlation ρ_{J_s} in the same way as the Wiener process, as presented in Subsection 2.3.4. The correlation in the Wiener ($W_1(t)$ and $W_2(t)$) and Poisson processes ($J_1(t)$ and $J_2(t)$) are modeled as presented in Section 2.3.4.

Examples of the load consumption of a load modeled using (3.12) are shown in Figure 3.22-3.25. In Figure 3.22-3.23, the loads are modeled without jumps, that is $\varsigma_p(t) = \varsigma_q(t) = 0$. By comparing these two figures two scenarios can be compared. That is what the load consumption looks like without correlation and with a correlation of $\rho_W = 0.8$.

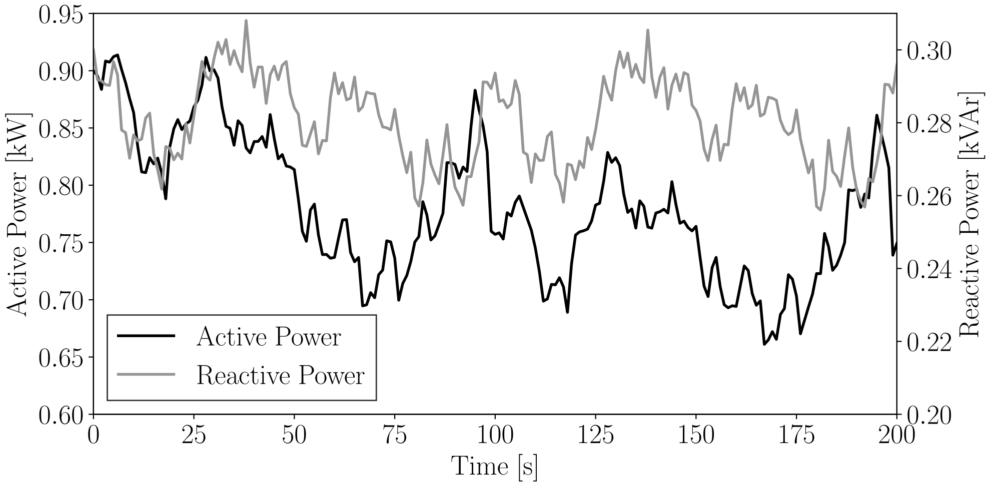

Figure 3.22: Active and reactive power of a load modeled without jumps with no correlation.

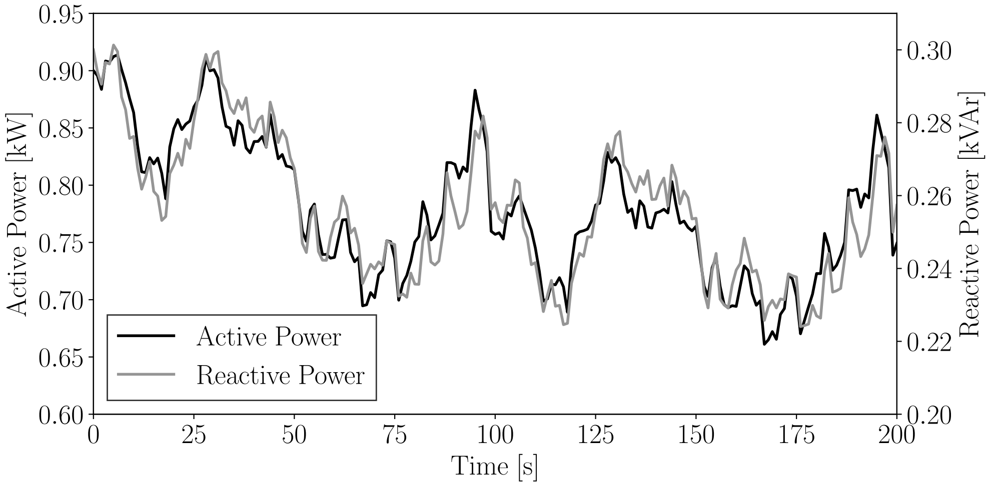

Figure 3.23: Active and reactive power of a load modeled without jumps with correlation ($\rho_W = 0.8$).

Figures 3.24 shows load consumption modeled with jumps where there is no correlation in the jump times or size. This results in the active and reactive power trajectories being very different from one and other and for example at the end of the simulation it can be seen that while the active power is dropping the reactive power is increasing. In Figure 3.25, an example is shown where both the jump times and jump amplitudes are correlated, that is $\rho_J = \rho_{J_s} = 0.8$. In this case we can see that the two trajectories are following the same trend and in many cases the jumps are proportionally similar in the active and reactive power consumed.

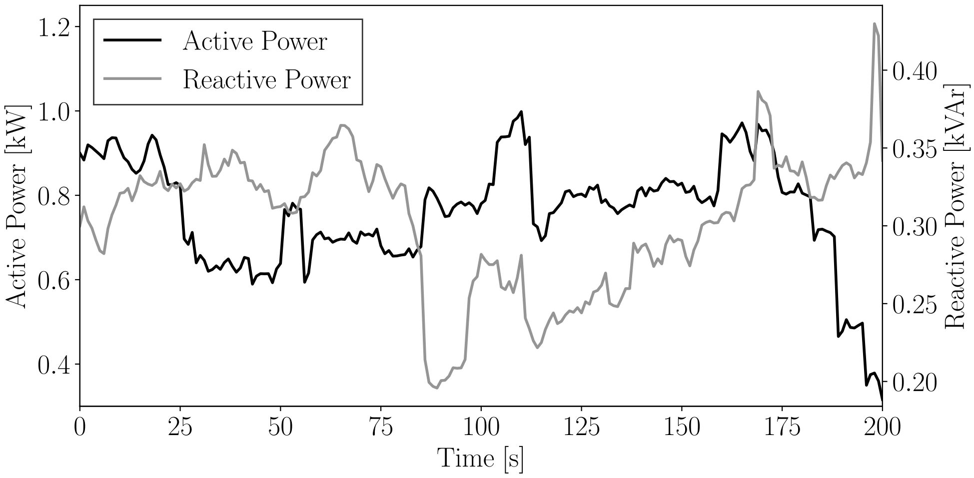

Figure 3.24: Active and reactive power of a load modeled with jumps with no correlation.

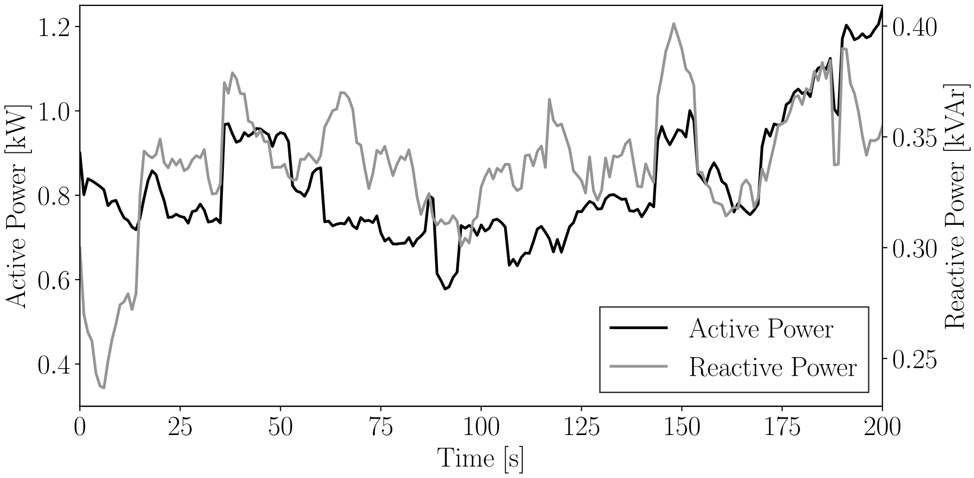

Figure 3.25: Active and reactive power of a load modeled with jumps with correlation ($\rho_J = 0.8$, $\rho_{J_s} = 0.8$).

The effect of considering this correlation in loads on the dynamics of power systems is studied in [117]. This case study is presented in Section 5.5 and further extended to a larger system.

CHAPTER

FOUR

STOCHASTIC POWER SYSTEM MODELS

In this chapter, power system models are formulated as a set of SDAEs. In particular, Section 4.1 discusses the inclusion of stochastic processes modeled as SDEs into DAE power system models. Then, Section 4.2 discusses the initialization of such power system models and a novel initialization method is presented. Finally, in Section 4.3, it is discussed how the stochastic models presented in Chapter 3 can be utilized and modified to capture the aggregated output of a whole renewable energy farm.

4.1 Power system modeling

Traditionally, the transient behavior of power systems is described through the following set of Differential Algebraic Equations (DAEs):

$$\begin{aligned} \dot{\boldsymbol{x}} &= \boldsymbol{f}(\boldsymbol{x}, \boldsymbol{y}, t)\,, \\ \boldsymbol{0}_m &= \boldsymbol{g}(\boldsymbol{x}, \boldsymbol{y}, t)\,, \end{aligned} \tag{4.1}$$

where $\boldsymbol{f}$ ($\boldsymbol{f} : \mathbb{R}^n \times \mathbb{R}^m \times \mathbb{R}^+ \mapsto \mathbb{R}^n$) are the differential equations; $\boldsymbol{g}$ ($\boldsymbol{g} : \mathbb{R}^n \times \mathbb{R}^m \times \mathbb{R}^+ \mapsto \mathbb{R}^m$) are the algebraic equations; $\boldsymbol{x}$ ($\boldsymbol{x} \in \mathbb{R}^n$) are the state variables, e.g., rotor speeds and rotor angles of synchronous machines, the dynamic states of loads and system controllers; $\boldsymbol{y}$ ($\boldsymbol{y} \in \mathbb{R}^m$) are the algebraic variables, e.g., line outages and faults, switching operation of tap-changers; $t \in \mathbb{R}^+$ is the time.

Equations (4.1) do not model the effect of stochastic perturbations on the systems transient behavior. Such stochastic perturbations can be originated in variable renewable energy sources, as discussed in Chapter 3, stochastic variations of loads, measurement errors of control devices and more. In the general case, these stochastic perturbations depend on the system variables. Thus, stochastic perturbations can be modeled as a set of SDEs, as presented in Section 2.2:

$$\dot{\boldsymbol{\eta}} = \boldsymbol{a}(\boldsymbol{x}, \boldsymbol{y}, \boldsymbol{\eta}, t) + \boldsymbol{b}(\boldsymbol{x}, \boldsymbol{y}, \boldsymbol{\eta}, t)\boldsymbol{\xi}, \tag{4.2}$$

where the stochastic perturbations are $\boldsymbol{\eta}$ ($\boldsymbol{\eta} \in \mathbb{R}^p$) and $\boldsymbol{\xi}$ ($\boldsymbol{\xi} \in \mathbb{R}^q$) is the vector of white noise processes that represent the time derivatives of the Wiener processes. Each of the SDEs is characterized by its drift $\boldsymbol{a}$ ($\boldsymbol{a} : \mathbb{R}^n \times \mathbb{R}^m \times \mathbb{R}^p \times \mathbb{R}^+ \mapsto \mathbb{R}^p$) and diffusion term $\boldsymbol{b}$ ($\boldsymbol{b} : \mathbb{R}^n \times \mathbb{R}^m \times \mathbb{R}^p \times \mathbb{R}^+ \mapsto \mathbb{R}^p \times \mathbb{R}^q$).

These stochastic perturbations can lead to stochastic behavior in the main system variables, such as the voltage and frequency, described through (4.1). Thus, the updated power system model including the stochastic perturbations is modeled as a set of Stochastic Differential Algebraic Equations (SDAEs):

$$\begin{aligned} \dot{\boldsymbol{x}} &= \boldsymbol{f}(\boldsymbol{x}, \boldsymbol{y}, \boldsymbol{\eta}, t)\,, \qquad (4.3)\\ \boldsymbol{0}_m &= \boldsymbol{g}(\boldsymbol{x}, \boldsymbol{y}, \boldsymbol{\eta}, t)\,, \\ \dot{\boldsymbol{\eta}} &= \boldsymbol{a}(\boldsymbol{x}, \boldsymbol{y}, \boldsymbol{\eta}, t) + \boldsymbol{b}(\boldsymbol{x}, \boldsymbol{y}, \boldsymbol{\eta}, t)\boldsymbol{\xi}\,, \end{aligned}$$

where the functions $\boldsymbol{f}$ ($\boldsymbol{f} : \mathbb{R}^n \times \mathbb{R}^m \times \mathbb{R}^p \times \mathbb{R}^+ \mapsto \mathbb{R}^n$) and $\boldsymbol{g}$ ($\boldsymbol{g} : \mathbb{R}^n \times \mathbb{R}^m \times \mathbb{R}^p \times \mathbb{R}^+ \mapsto \mathbb{R}^m$) are updated to include the effect of the stochastic term $\boldsymbol{\eta}$.

4.2 Initialization of stochastic power system models

This section discusses the initialization of the SDAE power system model in (4.3). The initialization method presented here and the case study outlined in Section 5.2 are presented in [125].

The initialization of deterministic power system models, described through the DAEs in (4.1), consists in finding a (stable) equilibrium point $(\boldsymbol{x}_o, \boldsymbol{y}_o)$ that satisfies the condition:

$$\begin{aligned} \mathbf{0}_n &= \boldsymbol{f}(\boldsymbol{x}_o, \boldsymbol{y}_o) \, , \\ \mathbf{0}_m &= \boldsymbol{g}(\boldsymbol{x}_o, \boldsymbol{y}_o) \, . \end{aligned} \tag{4.4}$$

The initial values of the deterministic state and algebraic variables are then set as $\boldsymbol{x}(0) = \boldsymbol{x}_o$ and $\boldsymbol{y}(0) = \boldsymbol{y}_o$, respectively.

Initializing the stochastic power system model (4.3), on the other hand, is not as straightforward. In the literature, two methods are commonly used, as follows.

- **Method 1:** The SDAEs are initialized in a deterministic way. That is the deterministic state and the algebraic variables are initialized as shown in (4.4) and the initial values of the stochastic processes are set equal to their expectation, i.e. $\boldsymbol{\eta}(0) = \boldsymbol{\eta}_o$.

- **Method 2:** The initialization of the DAEs in (4.1) is the same as in Method 1, thus leading to $\boldsymbol{x}(0) = \boldsymbol{x}_o$ and $\boldsymbol{y}(0) = \boldsymbol{y}_o$, which are obtained using $\boldsymbol{\eta} = \boldsymbol{\eta}_o$. Once this step is completed, the stochastic processes $\boldsymbol{\eta}$ are initialized in a probabilistic way. That is, the initial value of the stochastic processes are selected at random based on their probability distributions, say $\boldsymbol{\eta}_s$. The complete initial point is thus represented by $\boldsymbol{x}(0) = \boldsymbol{x}_o$, $\boldsymbol{y}(0) = \boldsymbol{y}_o$ and $\boldsymbol{\eta}(0) = \boldsymbol{\eta}_s$.

Neither of these two methods provide the correct initialization of the whole SDAE system. The method, presented below, proposes an alternative and efficient way to initialize the SDAE system as a whole. Note also that, in general, the initial point obtained with Method 2 yields $\boldsymbol{g}(\boldsymbol{x}_o, \boldsymbol{y}_o, \boldsymbol{\eta}_s) \neq \mathbf{0}_m$. This, however, is not an issue as, at the first step of the time domain simulation, the condition $\boldsymbol{g}(\boldsymbol{x}_o, \boldsymbol{y}(0), \boldsymbol{\eta}_s) = \mathbf{0}_m$ is recovered by means of the internal loop of the numerical integration scheme.

4.2.1 Proposed Method 3

The starting point of the proposed initialization method is the set of SDAEs linearized at the equilibrium point $(\boldsymbol{x}_o, \boldsymbol{y}_o, \boldsymbol{\eta}_o)$ as per Method 1 above. The linearization of (4.3) gives:

$$\begin{bmatrix} \dot{\tilde{\boldsymbol{x}}} \\ \mathbf{0}_m \\ \dot{\tilde{\boldsymbol{\eta}}} \end{bmatrix} = \begin{bmatrix} \boldsymbol{f_x} & \boldsymbol{f_y} & \boldsymbol{f_\eta} \\ \boldsymbol{g_x} & \boldsymbol{g_y} & \boldsymbol{g_\eta} \\ \mathbf{0}_{p,n} & \mathbf{0}_{p,m} & \boldsymbol{a_\eta} \end{bmatrix} \begin{bmatrix} \tilde{\boldsymbol{x}} \\ \tilde{\boldsymbol{y}} \\ \tilde{\boldsymbol{\eta}} \end{bmatrix} + \begin{bmatrix} \mathbf{0}_{n,q} \\ \mathbf{0}_{m,q} \\ \boldsymbol{b}(\boldsymbol{\eta}_o) \end{bmatrix} \boldsymbol{\xi} \, , \tag{4.5}$$

where $\boldsymbol{f_x}$, $\boldsymbol{f_y}$, $\boldsymbol{f_\eta}$, $\boldsymbol{g_x}$, $\boldsymbol{g_y}$, $\boldsymbol{g_\eta}$, $\boldsymbol{a_\eta}$ are the Jacobian matrices of the system calculated at $(\boldsymbol{x}_o, \boldsymbol{y}_o, \boldsymbol{\eta}_o)$. $\tilde{\boldsymbol{x}}$ and $\tilde{\boldsymbol{\eta}}$ represent the deterministic and the stochastic states of the linearized system. Eliminating the algebraic variables from (4.5) and defining $\boldsymbol{z} = (\tilde{\boldsymbol{x}}, \tilde{\boldsymbol{\eta}})$ leads to a set of linear SDEs, as follows:

$$\begin{aligned} \begin{bmatrix} \dot{\tilde{\boldsymbol{x}}} \\ \dot{\tilde{\boldsymbol{\eta}}} \end{bmatrix} &= \begin{bmatrix} \boldsymbol{f_x} - \boldsymbol{f_y}\boldsymbol{g_y}^{-1}\boldsymbol{g_x} & \boldsymbol{f_\eta} - \boldsymbol{f_y}\boldsymbol{g_y}^{-1}\boldsymbol{g_\eta} \\ \mathbf{0}_{p,n} & \boldsymbol{a_\eta} \end{bmatrix} \begin{bmatrix} \tilde{\boldsymbol{x}} \\ \tilde{\boldsymbol{\eta}} \end{bmatrix} + \begin{bmatrix} \mathbf{0}_{n,q} \\ \boldsymbol{b}(\boldsymbol{\eta}_o) \end{bmatrix} \boldsymbol{\xi} \\ &= \mathbf{A}_o \, \boldsymbol{z} + \mathbf{B}_o \, \boldsymbol{\xi} \, . \end{aligned} \tag{4.6}$$

Based on the Fokker-Planck equation, as presented in Chapter 5 of [126], the probability distribution of all state variables in stationary condition satisfy:

$$\mathbf{P}(\boldsymbol{z}) = (\det \mid 2\pi\mathbf{C} \mid)^{-1/2} \cdot \exp\bigg(-\frac{1}{2}\boldsymbol{z}^T\mathbf{C}^{-1}\boldsymbol{z} \bigg) \, , \tag{4.7}$$

where $\mathbf{C}$ is the covariance matrix of the state variables in (4.6). This matrix is symmetric and satisfies the Lyapunov equation:

$$\mathbf{A}_o\mathbf{C} + \mathbf{C}\mathbf{A}_o^T = -\mathbf{B}_o\mathbf{B}_o^T \, , \tag{4.8}$$

which is a special case of the Riccati equation. This equation can be solved numerically for systems of arbitrary size.

The covariance matrix can be clustered as:

$$\mathbf{C} = \begin{bmatrix} \mathbf{C}_{\boldsymbol{x}\boldsymbol{x}} & \mathbf{C}_{\boldsymbol{x}\boldsymbol{\eta}} \\ \mathbf{C}_{\boldsymbol{\eta}\boldsymbol{x}} & \mathbf{C}_{\boldsymbol{\eta}\boldsymbol{\eta}} \end{bmatrix}, \tag{4.9}$$

where $\mathbf{C}_{\boldsymbol{x}\boldsymbol{x}}$ and $\mathbf{C}_{\boldsymbol{\eta}\boldsymbol{\eta}}$ are the covariance matrices of $\tilde{\boldsymbol{x}}$ and $\tilde{\boldsymbol{\eta}}$, respectively. The two remaining sub-matrices $\mathbf{C}_{\boldsymbol{x}\boldsymbol{\eta}}$ and $\mathbf{C}_{\boldsymbol{\eta}\boldsymbol{x}} = \mathbf{C}_{\boldsymbol{x}\boldsymbol{\eta}}^T$ represent the covariance between the deterministic $\tilde{\boldsymbol{x}}$ and stochastic $\tilde{\boldsymbol{\eta}}$ state variables.

The proposed method, Method 3, to initialize the SDAE power system model in (4.3) begins with the initialization of the stochastic state variables, $\boldsymbol{\eta}$. The initial stochastic state variables are set independently at random, based on their probability distribution, i.e. $\boldsymbol{\eta}(0) = \boldsymbol{\eta}_s$. That is, in the same way as in Method 2. Then, the state variables $\boldsymbol{x}$ are initialized using the mean of the conditional distribution of $\boldsymbol{x}$, given $\boldsymbol{\eta}$ [127], that is:

$$\boldsymbol{x}_s = \boldsymbol{x}_0 + \mathbf{C}_{\boldsymbol{x}\boldsymbol{\eta}} \mathbf{C}_{\boldsymbol{\eta}\boldsymbol{\eta}}^{-1} \boldsymbol{\eta}_s \,. \tag{4.10}$$

Thus, in this way the initial value of $\boldsymbol{x}$, set using Method 1 is modified to consider the effect of the random stochastic state initial value $\boldsymbol{\eta}_s$, considering their correlation.

As discussed for Method 2, there is no need to update the algebraic variables as they will be determined by the time integration routine. Hence, the resulting initial point is $\boldsymbol{x}(0) = \boldsymbol{x}_s$, $\boldsymbol{y}(0) = \boldsymbol{y}_o$ and $\boldsymbol{\eta}(0) = \boldsymbol{\eta}_s$.

In Subsection 4.2.2, the OMIB test system is used to compare the proposed Method 3 to Method 1 and 2. Furthermore in Section 5.2 the Irish system model is used to demonstrate that Method 3 scales well for larger systems.

4.2.2 Test case

The test system used in this part is the simple three bus OMIB system where the machine is a wind power plant. The OMIB test system utilized in this section is shown in Figure 4.1.

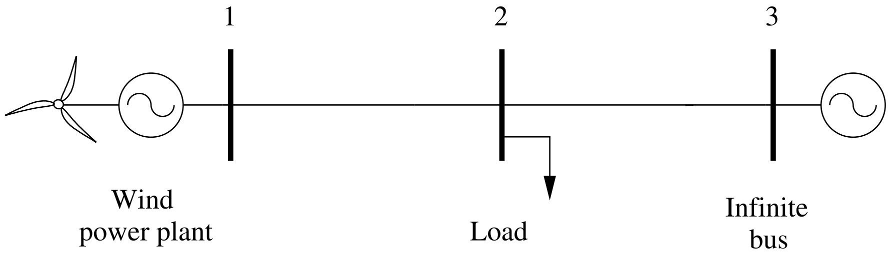

Figure 4.1: One-Machine Infinite-Bus (OMIB) test system.

The wind speed input for the wind power plant is modeled as the following Ornstein-Uhlenbeck (OU) stochastic process.

$$\dot{\eta}(t) = \alpha(\mu - \eta(t))dt + \beta\xi, \tag{4.11}$$

where $\mu = 9.67$ m/s is the mean wind speed, $\alpha = 0.01$ is the mean reversion speed and $\beta = 0.05$ is the diffusion constant of the process.

The OMIB system is utilized to test the three initialization methods, namely Method 1, 2 and 3. For each method, $1,000$ Monte Carlo simulations are solved for 60 s with a time step of 0.1 s. As an example, the active power flow from Bus 2 to 3 is shown in Figure 4.2-4.4. The system base is 100 MW. In these figures, μ and σ represent the mean and standard deviation of the $1,000$ simulated time series. The process is said to have reached stationarity when the standard deviation becomes constant. At this point, the simulations represent the full probability distribution of the variable.

Figure 4.2 shows that the standard deviation of the active power is still growing at the end simulation time when Method 1 is utilized. Thus, it has not reached stationarity. The time it takes the system variables to reach stationarity for Method 1 is dictated by the ACF of the stochastic processes in the system. In this case the ACF of the single stochastic process in (4.11) is $\exp(-\alpha t)$. Therefore,

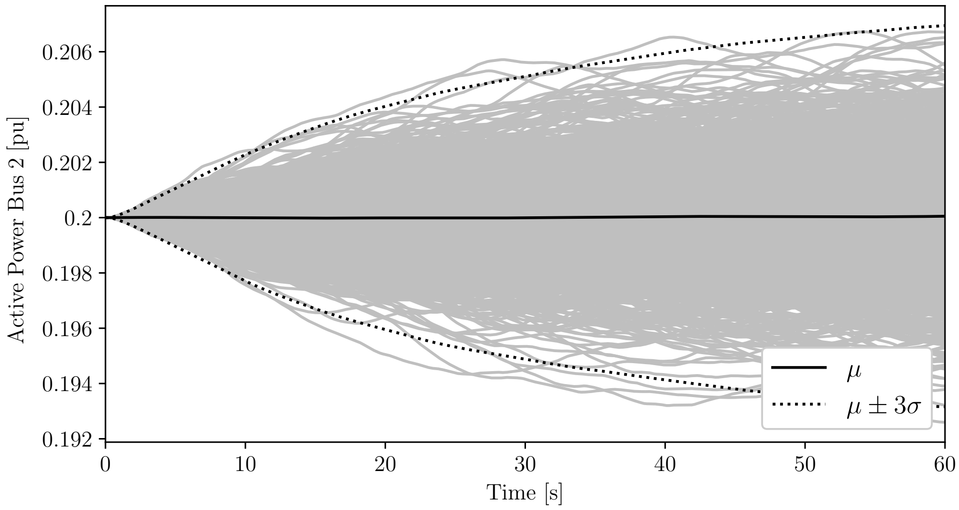

Figure 4.2: Illustration of Method 1. In this case the stochastic processes have not reached stationarity as the standard deviation is still continuously growing at time 60 s.

this particular system needs to be simulated for at least $2/\alpha = 200$ s to reach stationarity, which requires a relatively large computing time.

To reduce the computing time required to reach stationarity, an option is to increase the time step. However, in general, this is not a feasible solution for power systems. The transient stability model, in fact, is stiff, i.e., it combines fast and slow dynamics. Fast dynamics quickly reach stationarity but need a small time step. On the other hand, slow dynamics dictate when the system trajectories reach stationarity.

Figure 4.3 shows the behavior of Method 2. In this method, the slowest dynamics of the differential equation $\boldsymbol{f}$ (in this case, wind power plant dynamics) determine how long the system takes to reach stationarity. This occurs, in this case, in approximately 20 s of simulated time. Thus, if the stochastic processes have a slow aACF, Method 2 requires less computing time than Method 1 to reach stationarity. Note that, for systems with slow dynamics, Methods 1 and 2 have an equivalent computational burden.

The results of the Monte Carlo simulations obtained with the proposed method are shown in Figure 4.4. In this case, the initial conditions are stationary as confirmed by the fact that the standard deviation is constant along the whole

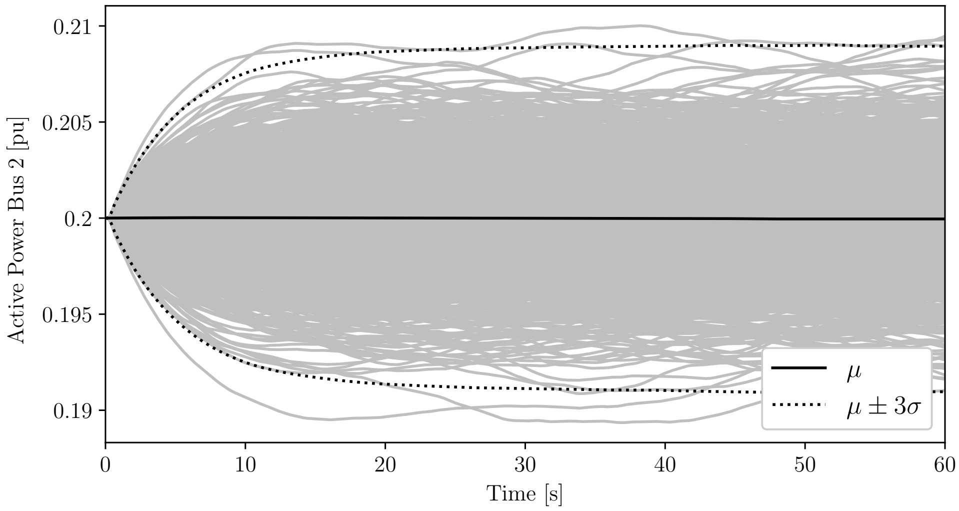

Figure 4.3: Illustration of Method 2. In this case the processes reach stationarity at time 20 s. From there on the standard deviation is practically constant.

simulation. This method significantly reduces the required computation time as no part of the simulated processes need to be discarded.

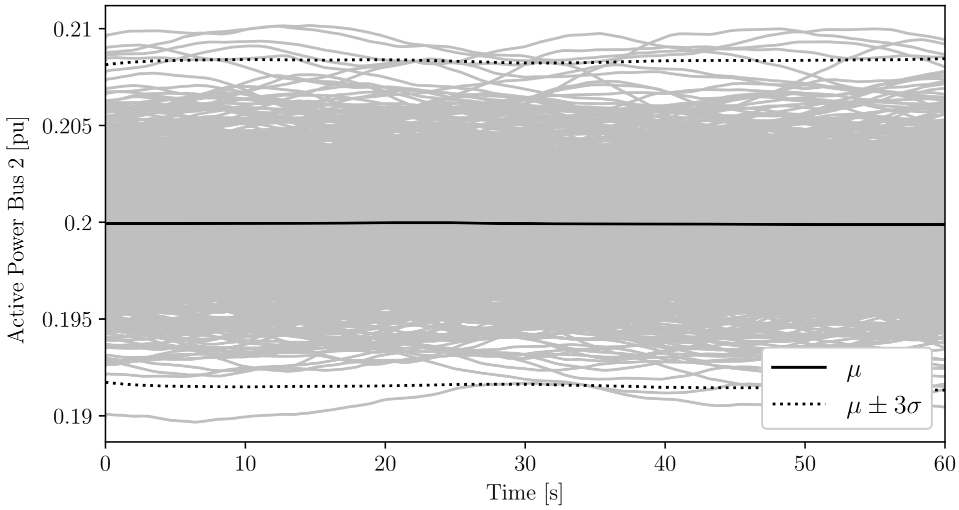

Figure 4.4: Illustration of the proposed Method 3.

4.3 Inclusion of renewable energy sources in the power system model

The models presented in Sections 3.1-3.3 capture the stochastic variability of the source, e.g. wind speed, solar irradiance and tidal current speed. In most power system models for dynamic analysis the individual turbines or PV panels are not modeled. Thus, an average model is used to model the aggregated output of the whole plant. For example as presented in [128] for a wind farm. In this section the modeling of the aggregated effect of the energy sources variability on a plant is discussed for the sources modeled in Sections 3.1 to 3.3.

4.3.1 Wind generation

The aggregated wind speed model considered for the dynamic studies in this thesis consists of two parts: a constant-mean wind speed, v_c, and a Gaussian stochastic process, $\rho_w(t)$. The wind is modeled in this way since the wind speed variations within a 10 minute time frame can be assumed to be normally distributed around a certain mean v_c [129]. The wind speed model used for each wind farm is:

$$v_{\text{wind}}(t) = v_c + \rho_w(t), \tag{4.12}$$

where $v_{\text{wind}}(t)$ is the modeled wind speed time-series and $\rho_w(t)$ is a stochastic process modeled as a SDE. The aggregated wind speed model considers both the filtering across the blade are of a single turbine and the aggregation effect across the whole wind farm.

Wind speed is not uniform across the rotor blade area. For example, wind speed at the tip, center and hub can differ [130]. However, these variations even out over the blade area. This damping effect by the rotor blades is modeled as a low-pass filter, shown in Figure 4.5. The input is the model in (4.12) generating wind speed at hub height of the wind turbine. The output is the equivalent wind speed that produces the same torque as the actual wind field [131].

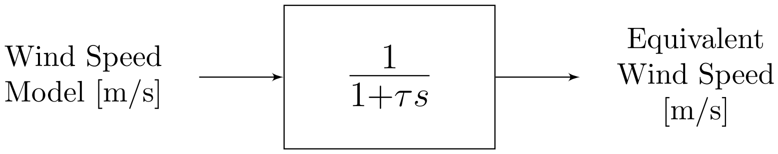

Figure 4.5: Low-pass filter that represents the damping effect of the blades of a wind turbine.

The time constant, τ [s], of the low-pass filter is proportional to the rotor radius, R [m], and the average wind speed at the hub height, v_c [m/s]. The time constant of the low-pass filter is:

$$\tau = \frac{\gamma R}{v_c} \ , \tag{4.13}$$

where γ is the decay factor over the disc [130].

The stochastic processes $\rho_w(t)$ is defined using Method II, presented in Subsection 2.3.2. Thus, $\rho_w(t)$ has the probability distribution $\mathcal{N}(\mu_{\rho_w}, \sigma^2_{\rho_w})$ and an ACF as in (2.34). The standard deviation of the process is set to be 20 % of the mean wind speed v_c as supported by [114] and analysis of the data set in [74]. The aggregated wind speed is defined through the σ_{ρ_w} parameter:

$$\sigma_{\rho_w} = 0.2 \cdot v_c / \sqrt{2 n_{turb}}, \tag{4.14}$$

where n_{turb} is the number of turbines in the wind farm. Thus, the standard deviation of the modeled wind speed decreases in proportion to the number of turbines, as the variability of wind speed averages out over a spread wind farm.

The power output of an example wind farm is shown in Figure 4.6. It shows two cases. The first case is when the wind speed is modeled as for one turbine. The second case is where the aggregated wind speed model presented in this section is used. The number of turbines for the aggregated case is 20. The parameters used for the wind speed model are those presented in [132].

4.3.2 Solar generation

The solar irradiance measured at a single PV panel is known to be very jumpy during mixed clouding conditions. The aggregation of a whole plant of PV panels smooths the effect of the most rapid jumps [77]. This smoothing effect is dependent on the area the plant covers. The aggregated irradiance for a PV plant can be modeled as a low pass filter, as shown in Figure 4.7 [133]. The single PV clear-sky index is modeled as presented in Section 3.2.

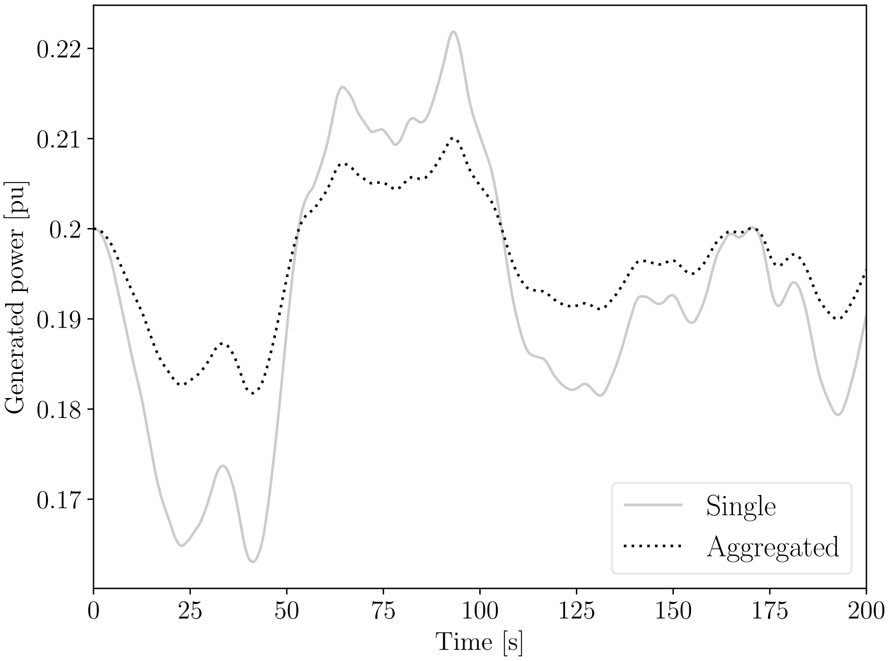

Figure 4.6: Generated power of a single wind turbine and an aggregated wind farm of 20 turbines.

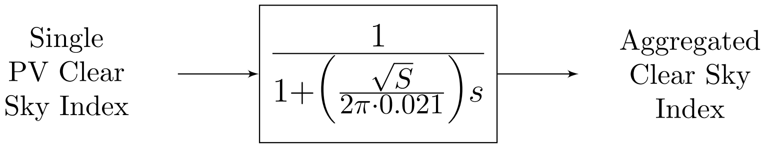

Figure 4.7: Low-pass filter that represents the smoothing effect of a PV plant.

The cut-off frequency for the filter is directly dependent on the square root of the plant area S, measured in Ha.

In Figure 4.8, the generated power of a farm of PV panels is shown. There the output power is compared for when the irradiance is modeled as presented in Section 3.2 for a single point to a case where the aggregated solar irradiance is considered, using the low-pass filter presented in Figure 4.7. In this case $S = 2$ Ha. The parameters used for the solar model are those presented in [78].

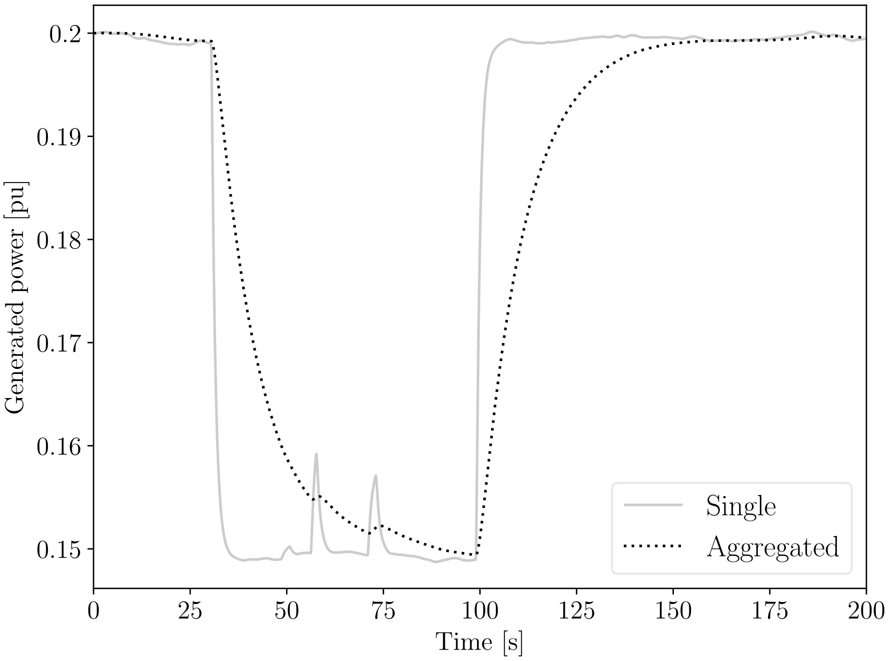

Figure 4.8: Generated power by a single PV panel and aggregated power output of a PV park covering an area of 2 Ha.

4.3.3 Tidal generation

The aggregated tidal current speed model used in this thesis consists of three parts. The first two parts are modifications of the model presented in Section 3.3. The third part allows to model the effect of multiple different wave scenarios. The three parts of the tidal current model are:

a. The variations in the tidal current due to the tidal phenomenon are very slow and relatively small in the time-frame of seconds to minutes. Thus, the predicted tidal current speed is modeled as a constant, v_{ct}.

b. The stochastic turbulence, $\rho_t(t)$, in the current speed is modeled using a stochastic process as defined in (2.31). It is defined in the same way as for the wind speed (see Subsection 4.3.1). The only difference is that the standard deviation of the tidal current speed is set to be 10 % of the current speed, v_{ct}, and the ACF parameters are set based on measured tidal current speed data [116].

c. The third part represents the effect of waves on the tidal current, $v_{\text{waves}}(t)$.

The resulting tidal current speed model is the following:

$$v_{\text{tide}}(t) = v_{\text{ct}} + \rho_t(t) + v_{\text{waves}}(t). \tag{4.15}$$

The ocean sea state is affected by a range of waves at the same time. These waves are generally modeled using the first order Stokes model representing a random sea-state [134]:

$$v_{\text{waves}}(t) = \sum_{i=1}^{N} a_i \omega_i \frac{\cosh[k_i(h+d)]}{\sinh(k_i d)} \cos[\omega_i t - k_i x + \phi_i], \tag{4.16}$$

where h is the vertical distance from the sea surface to the hub height of the tidal turbine, positive upwards, and d is the sea depth. ϕ_i are random phases, uniformly distributed between 0 and 2π, ω_i is the frequency of the i-th frequency component, k_i is the wave number of the i-th frequency component. Finally

$$a_i = \sqrt{2S(\omega_i)\Delta\omega_i} \tag{4.17}$$

is the amplitude of the i-th frequency component, defined from the frequency spectrum, $S(\omega)$, of the waves.

The frequency spectrum considered is the JONSWAP spectrum [134]. The wave angular frequency, ω_i, is within the frequency band, $\Delta\omega_i$, and N different frequency components are considered to represent the random sea-state. The JONSWAP spectrum is defined as:

$$S(\omega) = \frac{mg^2}{\omega^5} \exp\left(- 1.25 \left(\frac{\omega_p}{\omega}\right)^4 \right) \gamma^Y, \tag{4.18}$$

where g is the acceleration due to gravity, ω_p is the peak frequency of the spectrum and γ is the peak enhancement factor which controls the sharpness of the peak. m is the intensity of the spectrum and can be defined for North Sea applications

[134] as:

$$m = 5.058\left(\frac{H_s}{T_p^2}\right)^2(1 - 0.287\ln\gamma), \tag{4.19}$$

where H_s is the significant wave height, $T_p = 2\pi/\omega_p$ is the peak wave period.

The aggregation model for the wave component of the tidal current, presented in [135] is utilized.

Waves can be thought of as an intermittent disturbance. They are not always present and are not likely to affect the different locations at the same time, with the same intensity. Thus, the Stokes model, coupled with the JONSWAP spectrum, can be set to represent different wave scenarios, as discussed and demonstrated in Section 5.3.

Figure 4.9 shows the effect of the variations in the tidal current on the power output of a tidal farm. Two cases are considered: (i) the current is assumed to be as measured in a single turbine; and (ii) the tidal current is obtained by aggregating 20 turbines. In the latter case, the parameters for the small wave scenario presented in [132] are used.

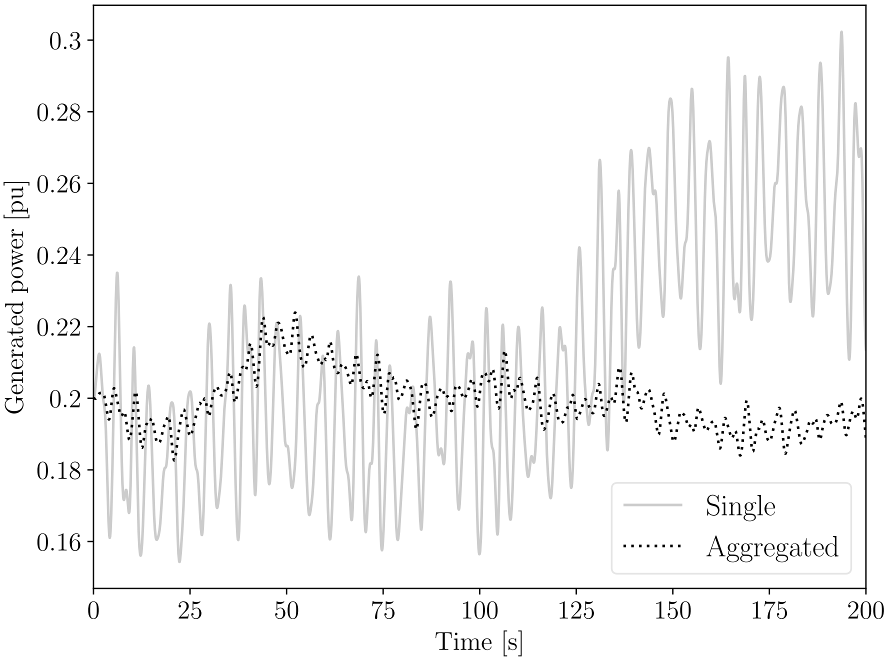

Figure 4.9: Output generated power of a single tidal turbine subject to waves and aggregated power output of a 20 turbine tidal farm.

4.3.4 Test case

This subsection considers the test system presented in Figure 4.1. Three cases are considered: wind, solar and tidal generation. The stochastic variations of each source are modeled using the aggregated models presented in Subsections 4.3.1 to 4.3.3.

As a metric to compare the different cases, it is convenient to compute ramp rates, defined as:

$$\Delta_h x_t = x_t - x_{t-h} \tag{4.20}$$

where x_t is the system variable at time t. $\Delta_h x_t$ is a new stochastic variable that gives the probability of the sizes of ramps in the system variable in a time step h. The ramp rates are computed for time lags $h = 0 - 100$ s. Then, the standard deviation of the ramp rates, $\Delta_h x_t$, for each time step h is computed. In this way, the ramp rates give information on how the ramps in the system variable evolve with time. Thus, the effect of the PDF and ACF of the sources of stochastic fluctuations in the system can be visualized in a single plot.

In Figure 4.10, the standard deviation of the ramps in the active power at Bus 2 in the OMIB system for the three cases is shown. In this comparison the fastest ramps within the 10 second time frame are seen for tidal generation. For time steps h bigger than 10 seconds the tidal generation results in smaller ramps in the active power than the solar and wind generation. Solar generation results in the biggest ramps in the active power.

The comparison of the standard deviation in the ramps in the voltage at Bus 2 in the OMIB system, shown in Figure 4.11 gives a very different picture. In this case, the ramps in the voltage for solar generation are the smallest and the biggest for wind generation.

It is important to note that only a single scenario for wind, tidal and solar generation are considered here. The results could be very different if the tidal scenario considered included no waves or bigger waves. Also the solar scenario modeled is one mixed clouding scenario. The jumps in the solar generation are

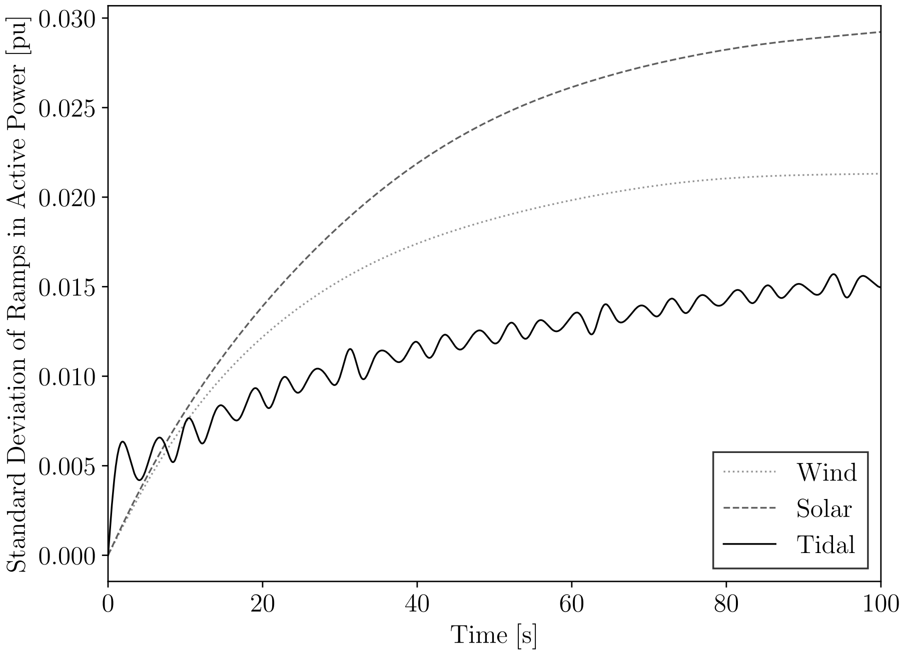

Figure 4.10: Standard deviation of the ramps in the active power at Bus 2 in the OMIB test system. Ramp rates are computed as in (4.20).

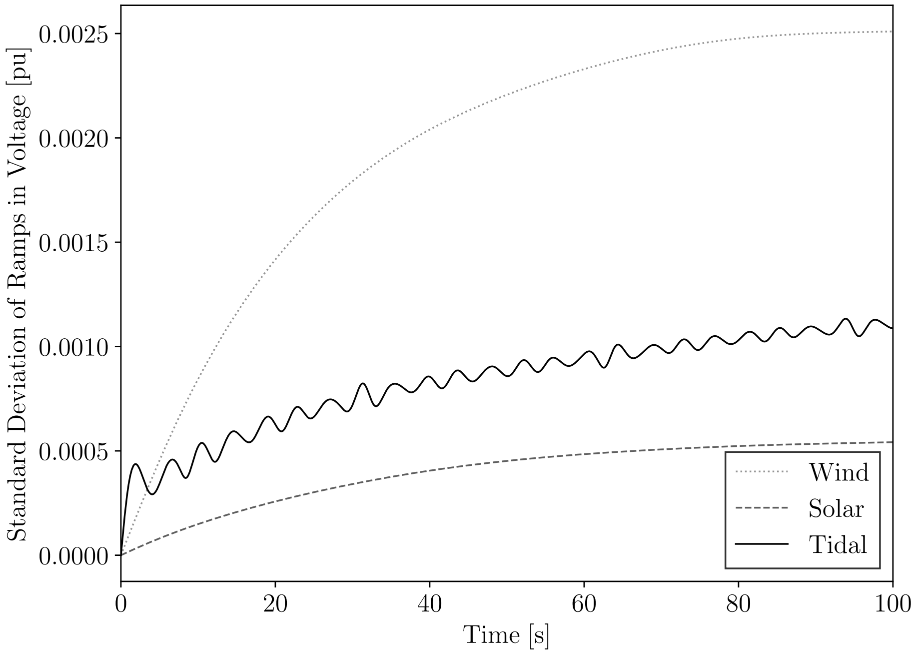

Figure 4.11: Standard deviation of the ramps in the voltage at Bus 2 in the OMIB test system. Ramp rates are computed as in (4.20).

not present for a clear sky scenario and could be even bigger for other mixed clouding scenarios.

CHAPTER

FIVE

SYSTEM STUDIES

This chapter presents a variety of case studies that are aimed at testing the stochastic models discussed in the previous chapters of this thesis. All case studies utilize the $1,479$ bus Irish system model, presented in Section 5.1.

In the first case study, outlined in Section 5.2 and published in [125], the initialization methods discussed in Section 4.2 are tested. Then a case study, presented in [132] of the Irish system including wind and tidal generation is presented in Section 5.3. Similarly, Section 5.4, compares scenarios for the Irish system with wind and solar generation. Finally, in Section 5.5, a case study, published in [117] considering the effect of modeling the correlation of the active and reactive power of loads on the system dynamics is presented.

All simulations are carried out using Dome, a Python-based software tool for power system analysis [136]. Dome solves the SDEs using the Itô integral. It supports solving the SDEs using either the Euler-Maruyama or Milstein integration method. For this work the Euler-Maruyama is used [33].

5.1 All-island Irish transmission system

The Irish system is an isolated and relatively small transmission system. It consists of two 50 Hz grids which are AC interconnected and operated by independent TSOs: System Operator for Northern Ireland and Eirgrid Group. The current transmission peak of the system is about 5,500 MW and the demand is expected to grow between 22 % and 53 % by 2030 [137]. The system has two HVDC interconnections, to Scotland and Wales, both with a capacity of 500 MW, flowing in both directions. The all-island Irish transmission system is shown in Figure 5.1.

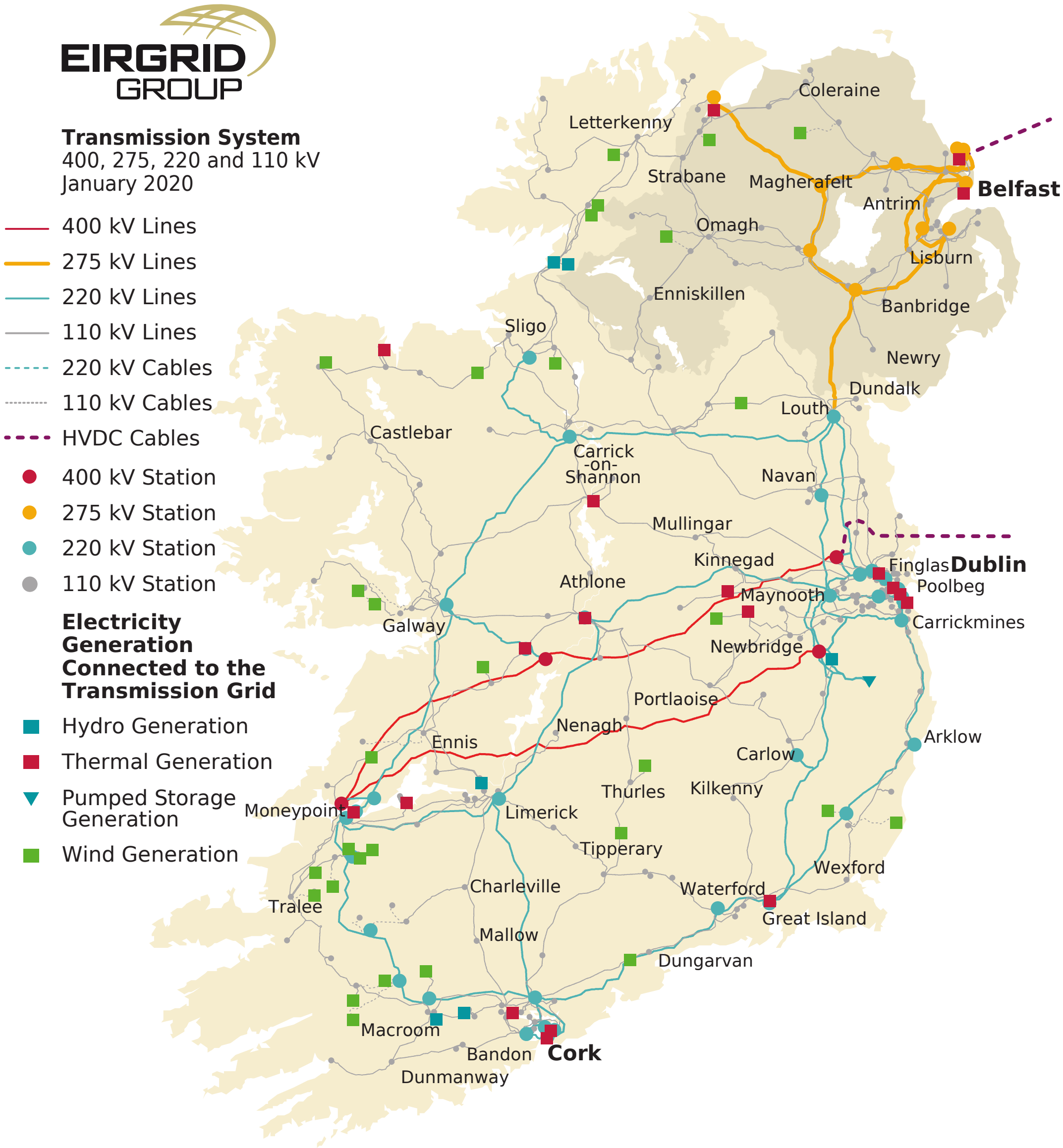

Figure 5.1: Map of the all-island Irish transmission system [138].

The installed wind generation in the system has increased rapidly for the last 10 years. At present, the record of produced wind power in the Irish system is approximately 3,500 MW and the system is able to handle upto 65 % renewable energy, primarily composed of wind power [139].

The Irish transmission system model utilized in this chapter consists of 1, 479 buses, 1, 851 transmission lines and transformers, 245 loads, 22 conventional synchronous power plants, modeled with 6th order synchronous machine models, with AVRs and turbine governors, 6 PSSs, and 169 wind power plants, of which 159 are DFIGs and 10 are CSWTs. In the system used for the case studies presented in this chapter the total load of the system is 2, 215 MW and 25 % of the total generated power is supplied by wind.

5.2 Initialization of SDAE-based power system models - case study

The initialization method presented in Subsection 4.2.1 is compared with Methods 1 and 2, in the case study outlined in this section. In Subsection 4.2.2, the initialization methods are tested for the OMIB system. In this section, the Irish system model, presented in Section 5.1, is utilized to demonstrate that the proposed Method 3 scales well and can be applied to large systems.

All simulations are solved exploiting parallelism on a 8 core 3.60 GHz Intel Xeon with 12 GB of RAM [136]. Equation (4.8) in the proposed initialization method is solved using the open-source library SLICOT.

5.2.1 Irish system model

In this case the only source of uncertainty in the Irish system model is the wind, modeled as presented in Subsection 4.2.2. The Irish test system is simulated using a Monte Carlo method, i.e. 1, 000 simulations with a simulated time of 60 s with a time step of 0.1 s using the three different initialization methods discussed in Section 4.2. Figure 5.2 shows the standard deviation of the voltage at a centrally located bus (Athlone in county Westmeath) in the Irish system. Method 1 does not reach stationarity within the 60 s time frame. Method 2 reaches stationarity in approximately 10 s.

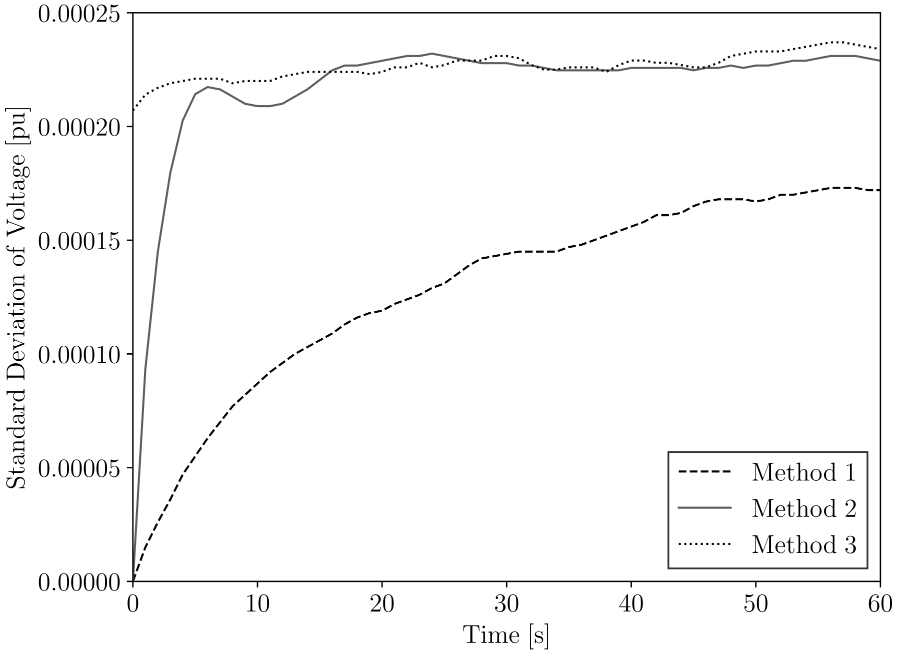

Figure 5.2: Standard deviation of voltage at a centrally located bus in the all-island Irish transmission system.

As expected the proposed initialization method, namely Method 3, allows starting the time domain simulations with points that are in stationary conditions. Only a very short and, effectively, negligible transient of the standard deviation can be observed due to the approximations introduced by the linearization and the solution of (4.8) obtained with the SLICOT library.

Table 5.1 shows the computing time for the three initialization methods, defined as the time that each method takes to reach a stationary condition, for both the OMIB system (Subsection 4.2.2) and the Irish system. For example, for the OMIB system, the computing time for Method 1 is the time required to solve $1,000$ simulations for 200 s. Similarly, the computing time of Method 2 for the OMIB system is the time required to simulate $1,000$ trajectories for 20 s. On the other hand, the computational burden of Method 3 is largely driven by the time required to solve (4.8). However, the Lyapunov equation needs to be solved only once for all Monte Carlo simulations of a given scenario.

Table 5.1: Computing time for each initialization method

	Computation time [s]	
	OMIB	**Irish system**
Method 1	28.38	1317.77
Method 2	7.00	76.50
Method 3	0.08	16.05

5.2.2 Remarks

The speedup of using the proposed Method 3 as apposed to Method 1 and 2 depends on a trade-off between the number of trajectories simulated with the Monte Carlo approach and the size of the system. If the number of trajectories is sufficiently high the proposed method will always safe time compared to the conventional methods.

Another benefit of Method 3, besides saving time is that less disc space is required. This is because the initial non-stationary part of the Monte-Carlo simulations for Method 1 and 2 are typically discarded as the full probability distribution of the variables is not simulated. With the proposed approach, Method 3, the whole trajectories are meaningful.

Finally, when using Method 1 and 2, the slowest processes in the system need to be identified to be able to know before-hand how long a simulation time is needed to reach stationarity. This can be involved and time consuming for large systems. With the proposed method, on the other hand, this analysis is not required.

5.3 Irish system with inclusion of wind and tidal generation

The renewable energy currently generated in the Irish system is almost entirely supplied by wind power plants. However, in the sea around Ireland there is a significant tidal energy potential. This section includes an Irish system case study presented in [132], considering both wind and tidal generation.

5.3.1 Irish system model

Ireland had the world's first large scale commercial tidal stream generators in operation from 2003 until 2017. Those turbines were a part of the SeaGen tidal test project and are located in Northern Ireland's Strangford Lough, producing 1.2 MW [111]. This project has provided valuable information for further development of tidal generation in Irish waters and has shown that tidal generation is a viable energy source for the Irish system. In [140], Ireland's tidal resources are assessed. Eleven practical resource sites for tidal generation are identified. The four sites with the greatest estimated capacity are shown in Figure 5.3. Table 5.2 shows the potential energy of the four locations.

Figure 5.3: Top four locations of potential tidal generation as identified in [140].

The tidal power plants are assumed to be installed in the four locations shown in Figure 5.3. The combined generation of these four locations is set to be 10 %

Table 5.2: The potential energy and installed power at the four modeled tidal power locations [140].

Location	Name	Potential Energy [GWh/y]	Installed Power [MW]
1	Inishtrahull Sound	514	67
2	Shannon Estuary	367	34
3	Tuskar Rock	420	47
4	Codling	791	69

of the total generation in the system. The local wind generation in each location is substituted with tidal generation. The set power of the tidal generation at each location is based on their potential energy and is shown in Table 5.2.

5.3.2 Scenarios

Five scenarios for the Irish power system model are studied:

- **Scenario 1:** The load is stochastic and modeled as presented in Section 3.4 with no correlation and no jumps. This serves as a base scenario. Thus, the same stochastic load models are used in the remaining scenarios.
- **Scenario 2:** The onshore wind, 25 % of generation, is stochastic, modeled as presented in Subsection 4.3.1.
- **Scenario 3:** Stochastic onshore wind, 15 % of generation, and stochastic offshore wind, 10 % of generation.
- **Scenario 4:** Stochastic onshore wind, 15 % of generation, and stochastic tidal, 10 % of generation, modeled as presented in Subsection 4.3.3, without waves.
- **Scenario 5:** Same as Scenario 4, that is stochastic onshore wind, 15 % of generation, and stochastic tidal, 10 % of generation, but the tidal generation is disturbed by waves.

Note that the specific parameters for the SDE-based models used can be found in [132]. In Scenario 3-5, offshore wind and tidal generation is installed in the locations identified in Figure 5.3, replacing 10 % of the local onshore wind generation.

Typically, the sea surface is assumed to be stationary for 20 minutes, upto a couple of hours. A stationary sea-state can be characterized by a set of parameters. These are the significant wave height, H_s, and the peak wave period, T_p. The significant wave height is defined as the mean wave height (trough to crest) of the highest third of the waves. The peak wave period is the wave period with the highest energy. The wave parameters for the considered sea-states are based on those listed in Table 3.17 in [134]. The parameters utilized for different sea-states in the case study are shown in Table 5.3, where H_s refers to the significant wave height and T_p to the peak wave period; and $T_{\min} - T_{\max}$ gives the range of wave periods, sampled from the JONSWAP spectrum in (4.18), for the Stokes wave model in (4.16).

Table 5.3: Three sea-states considered for Scenario 5.

Sea-state		H_s [m]	T_p [s]	$T_{\min} - T_{\max}$ [s]
(S)	**Small waves**	1	5	$1.4 - 8.8$
(M)	**Moderate waves**	2.5	7	$2.8 - 13.5$
(L)	**Large waves**	5	10	$3.8 - 15.5$

Scenario 5 includes three cases, where waves affect the tidal current. The three cases take into account the locations of the four tidal power plants. The largest significant wave heights, of about 5 meters, are seen on the west coast during winter. On the other hand, the average significant wave heights, in the Irish sea, do not exceed 2 meters, during any season [141]. Thus, Location 1 & 2 are more likely to experience higher significant wave heights than Location 3 & 4, as they are facing the Atlantic ocean. Specifically, Location 1 is likely to experience the worst wave conditions. Table 5.4 shows the sea-state at each location, for the three cases of Scenario 5.

The standard deviation of the ramp rates, computed using (4.20), for a range of time lags of the Centre of Inertia (COI) frequency are utilized to compare the scenarios. This measure is used as it enables assessing the effect of the ACF and PDF of the stochastic sources on the system variables through a single process.

Table 5.4: Sea-state at each location, for the three cases considered in Scenario 5. S, M and L represent small, moderate and large waves, respectively as presented in Table 5.3.

Case\Location	**1**	**2**	**3**	**4**
a	S	S	S	S
b	M	M	S	S
c	L	M	S	S

5.3.3 Wind versus tidal generation

The Irish system with all the loads modeled as stochastic (Scenario 1) is studied first. This scenario serves as a reference for the remaining scenarios. To validate the stochastic load scenario, frequency data from the Irish system, gathered in the AMPSAS project is used. The frequency is measured with a 10 Hz sampling frequency. In this case, the morning of a singular day, that is the 20th of May in 2014, is considered. During this time period there is almost no wind generation, hence the stochastic fluctuations in the frequency are mainly due to loads, as well as dispatches. Further details on these measurements are provided in [142].

Figure 5.4 shows the standard deviation of the ramp rates of the measured frequency data and the COI frequency, for the simulated Scenario 1. The model underestimates the frequency ramps in the initial 20 s, when compared to the measured data. However, for higher time steps, the model, for Scenario 1, and the measured data are in agreement.

The five different scenarios, as presented in Subsection 5.3.2, are compared in Figure 5.4. The inclusion of stochastic wind, in Scenario 2, increases the standard deviation of the ramp rates by approximately 25 %. An even bigger change is seen for Scenario 3-5. For these scenarios, however, the generation profile of the system had to be modified to accommodate offshore wind or tidal power plants.

The wind generation in Ireland is mostly composed of small farms spread across the system. For Scenario 3-5, these small farms are replaced by four much larger offshore wind or tidal farms. This causes relatively larger power fluctuations to be introduced in four points in the system. Whereas, for Scenario 2, smaller power fluctuations are installed in locations spread across the area.

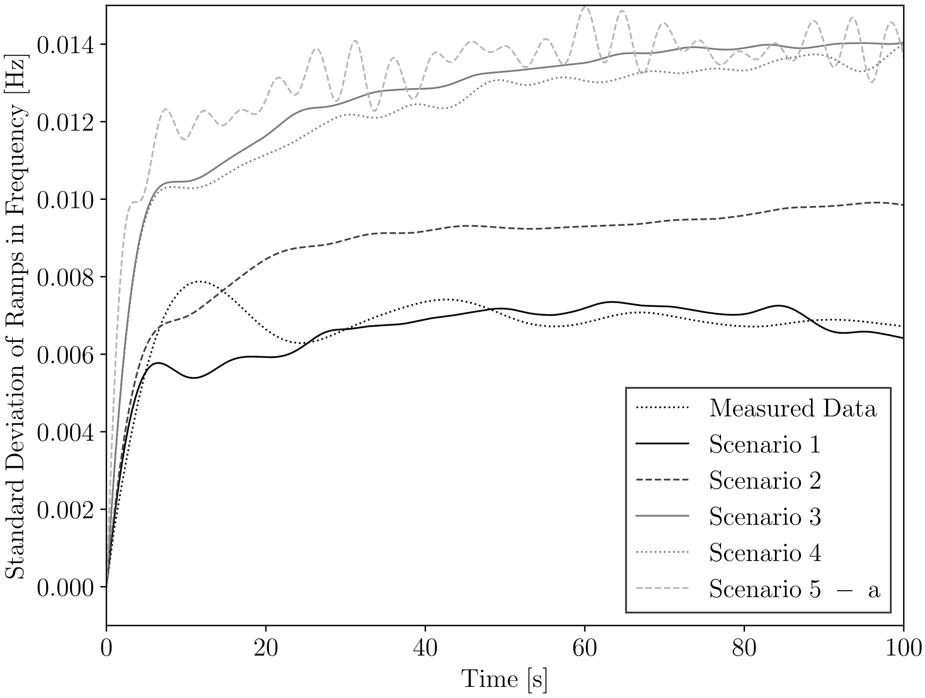

Figure 5.4: Standard deviation of the ramps in the frequency of the COI for Scenario 1-5, as well as of the measured frequency [142]. Ramp rates are computed as in (4.20).

Figure 5.4 shows that Scenario 4 has slightly smaller frequency variations than Scenario 3. This indicates that offshore wind introduces larger frequency variations than tidal generation. However, the set up of the farms, the number of turbines and the turbine sizes also impact the stochastic variations in the output power of the farms. Thus, it cannot be claimed that either source introduces less frequency variations. It can only be stated that tidal generation, when compared to wind generation, if no waves are presents, does not necessarily introduce bigger system frequency variations.

The trajectories of the standard deviation of the frequency ramps for Scenario 5-a are shown in Figure 5.4. In this case, all tidal farms are subject to relatively small waves simultaneously. This is the most common wave scenario for the Irish system. The inclusion of waves in the tidal current results in oscillatory fluctuations in the power outputs of the tidal farms, with a time period of less than 10 s. This increases the frequency variability, for the initial 20 s and introduces oscillations in the system frequency.

Scenario 5-b represents moderate waves in both Location 1 & 2, which are facing the Atlantic ocean. In this case, frequency ramps have a standard deviation of about 0.015 Hz, within a few seconds, as shown in Figure 5.5. This state is likely to last for 20 minutes upto a few hours at a time.

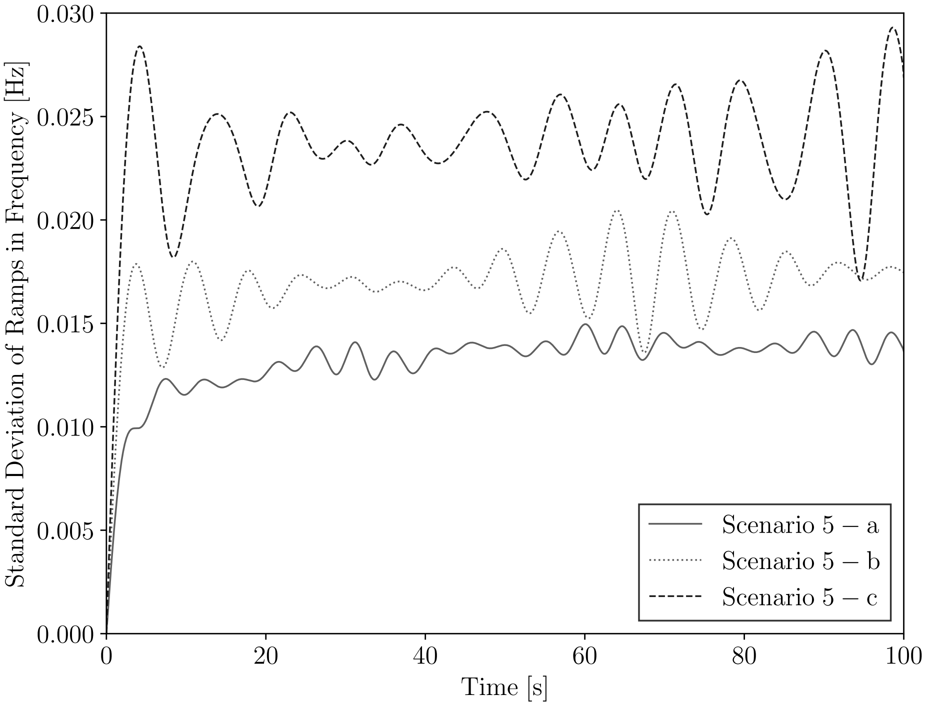

Figure 5.5: Standard deviation of the ramps in the frequency of the COI for Scenario 5, case a, b and c. Ramp rates are computed as in (4.20).

Scenario 5-c represents the worst case scenario. In this case Location 1 is experiencing large waves, with longer time periods, that is swell waves. This case is characterized by unacceptable frequency variations. Energy storage systems can be installed along side tidal generation, as suggested in [102] to mitigate these fluctuations. An alternative solution is to include primary frequency control in the tidal generation. This is discussed in the next section.

5.3.4 Frequency control of tidal generation

In this section, frequency control of tidal generation is considered, to reduce the frequency variability caused by the waves of Scenario 5. The similarity between tidal and wind turbines allows for the the frequency control implemented for wind turbines to be adapted for tidal turbines. A common approach for wind turbine frequency control is to bypass the Maximum Power Point Tracking and set the power output based on the deviation of the measured frequency (droop control) and/or Rate of Change of Frequency (ROCOF) control. The combination of the two strategies proposed in [143] for wind turbines is considered below.

The droop controller, with gain $1/R$, is comparable to the primary frequency controller of a synchronous machine. The ROCOF controller consists of a low-pass filter with time constant T_l, the time derivative of the frequency measurement and a gain K_l. The two controllers are complementary. The ROCOF control is faster and has its main effect in the very first instants after the frequency drop. However, the droop control is slower and mitigates the frequency deviation [143].

Figure 5.6 shows a comparison of the three different cases for Scenario 5 with the inclusion of frequency control in the four tidal power plants. Compared to the results presented in Figure 5.5, frequency variations are approximately halved in size for all three cases. For comparison, Figure 5.6 also shows Scenario 2 and 3, i.e. the two scenarios with only wind generation. The frequency control of the tidal turbines effectively mitigates the frequency variations for both Scenario 5-a and 5-b to be less than those for Scenario 3, excluding the first few seconds. Therefore, coupling frequency control to tidal generation can reduce the frequency variations, due to the waves, to an acceptable level.

5.3.5 Remarks

It is important to note that the sea state is strongly dependent on the location, as discussed in Subsection 5.3.2. Thus, the location is the first design parameter to be considered to reduce the impact of waves on tidal generation. If the potential tidal locations are all prone to extreme wave conditions, it is key to determine the optimal placement for the tidal power plants to minimize the impact of waves on the system. In the case of the Irish system, for Location 1 & 2, Scenario 5-c represents the worst case scenario, while for Location 3 & 4 the frequency variations due to wave disturbance would not get bigger than those shown for

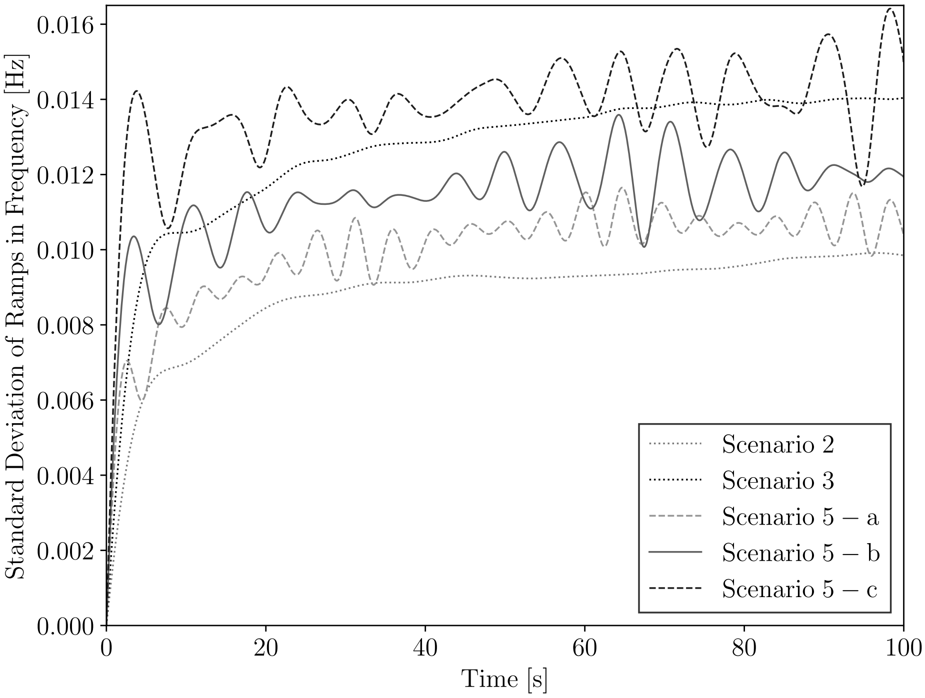

Figure 5.6: Standard deviation of the ramps in the frequency of the COI for Scenario 5, case a, b and c with frequency control. Scenarios 2 and 3 are shown for comparison. Ramp rates are computed as in (4.20).

Scenario 5-a. Thus, it appears sensible to commission tidal installments on the east coast first, e.g. Locations 3 & 4.

5.4 Irish system with inclusion of wind and solar generation

The Climate Action Plan from 2019 states that 70 % of electricity in the Irish system will be supplied by renewable sources by 2030. This means that the current limit of 65 % renewable energy in the system needs to be raised to 95 % by 2030 [55]. To meet this goal 1.5 GW of grid-scale solar PV energy is set to be installed in the system, along side the biggest source of renewable energy, wind. The current goal of Eirgrid Group is to have 100 MW of solar installed by 2024. In Northern Ireland over 100 MW is already supplied by solar PV and System Operator for Northern Ireland expects the solar capacity to grow to 179 MW by the end of 2022

[144]. This section presents a case study of the Irish system with solar and wind generation.

5.4.1 Irish system model

The Irish system model is divided up into 10 areas. In 7 of those areas there is wind generation. For this case study 10 % of the wind generation in the system presented in Section 5.1 is replaced with solar PV generation. The capacity of the installed solar PV is distributed equally between the 7 areas.

5.4.2 Scenarios

Three different scenarios for the Irish system model are studied:

- **Scenario a:** The onshore wind, 25 % of generation, is stochastic modeled as presented in Subsection 4.3.1.
- **Scenario b:** Stochastic onshore wind, 15 % of generation, and stochastic solar, 10 % of generation, modeled as presented in Subsection 4.3.2, for a mostly clear sky.
- **Scenario c:** Stochastic onshore wind, 15 % of generation, and stochastic solar, 10 % of generation, modeled as presented in Subsection 4.3.2, for a mixed clouding condition.

In all scenarios the loads are modeled as stochastic as presented in Section 3.4, with no jumps and no correlation in the active and reactive power. The parameters used for the stochastic load and wind models are presented in [132]. The parameters for the stochastic solar model are those presented, based on data, in [78]. The plant area parameter S for the aggregated model, presented in Subsection 4.3.2 is set based on the capacity of the individual PV farms. All PV farms are assumed to produce 150 W/m^2.

5.4.3 Wind versus solar generation

All scenarios are simulated for 10,000 s with a time step of 0.1 s. In Figure 5.7, the standard deviation of the ramps in the COI frequency of the system is shown for Scenario a, b and c, calculated using (4.20). There it can be seen that for the first 10 s the standard deviation is approximately the same for all three scenarios. In the time frame from 10 to 40 s Scenario a, with only wind has a slightly higher standard deviation. Scenario b which represents a mostly clear sky has a lower standard deviation than Scenario a in time frames upto approximately 60 s after that the two scenarios are similar. Scenario c shows bigger ramps in the frequency for time steps above 40 s. This is as expected because of the jumps in the solar generation. However, the filtering effect of aggregating multiple PV generators results in the jumps ramping up over longer time frames.

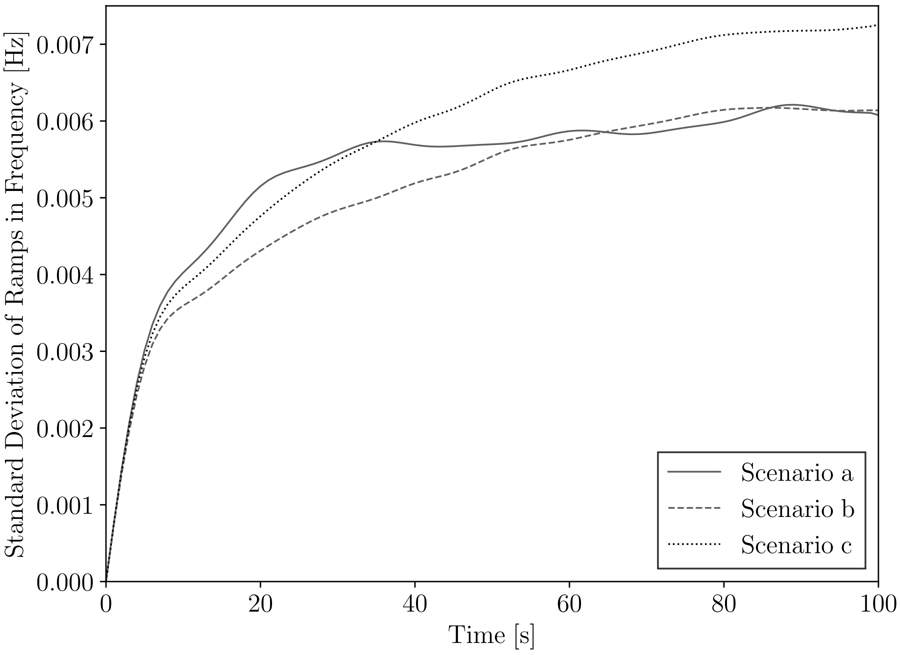

Figure 5.7: Standard deviation of the ramps in the frequency of the COI for Scenario a, b and c. Ramp rates are computed as in (4.20).

5.4.4 Remarks

It is worth noting that the stochastic solar model used in Scenario c represents the worst case scenario in terms of short-term variability of solar PV. That is the scenario where there are intermittent clouds blocking the solar PVs. In all other weather conditions it is likely that the solar generation will not add more than wind to the system frequency uncertainty as can be seen for Scenario b. Thus, including solar generation in the renewable energy mix in Ireland could be a good option, considering the frequency stability of the system.

5.5 Case study with correlated active and reactive power loads

In this case study the effect of the correlation in the active and reactive power of loads on power system dynamics is studied. First the 3-machine, 9-bus test system is used as presented in [117]. Then, the analysis is extended to the Irish system.

5.5.1 9-bus test system model

The test power system used in this case study is the Western System Coordinating Council 3-machine, 9-bus system shown in Figure 5.8. The system base is 100 MVA and the system frequency is 60 Hz. Further details on the model can be found in [145]. Note that for this case study the voltage levels of the system have been lowered compared to the original case. This is done to demonstrate a case where the lower voltage limits might be reached.

Loads are modeled as stochastic as presented in Section 3.4. The parameters used for the load model are set as follows. The mean reversion parameters of the processes are set as $\alpha_p = \alpha_q = 0.02$. σ_p and σ_q are set individually for each load so that the standard deviation of the variations is 5 % of p_{L0} and q_{L0}, respectively. The standard deviation of the jump size σ_{ς_p} and σ_{ς_q} is set to 10 % of p_{L0} and q_{L0}, respectively.

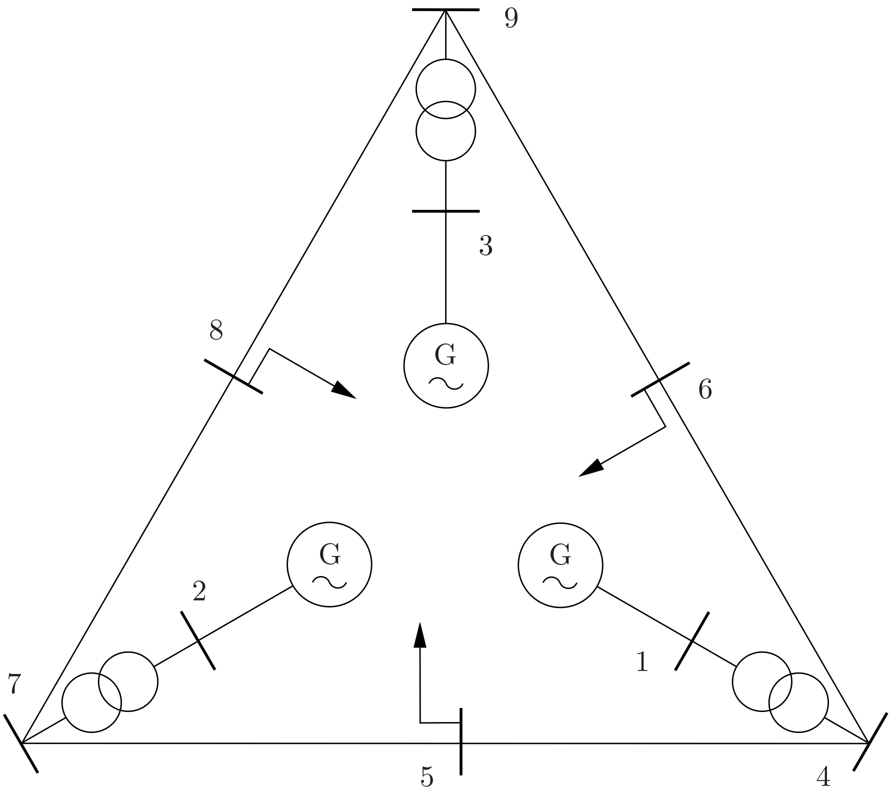

Figure 5.8: Western System Coordinating Council 9-bus test system.

For this case study two different cases are considered:

- **Case 1:** Loads are modeled without jumps. That is $\varsigma_p(t) = \varsigma_q(t) = 0$. The effect of correlation in the stochastic component, through ρ_W, is studied.
- **Case 2:** Loads are modeled with jumps. The effect of correlation in the jump time (ρ_J) and size (ρ_{J_s}) is studied.

Case 1

Three scenarios are examined, namely: (a) $\rho_W = 0$, (b) $\rho_W = 0.5$ and (c) $\rho_W = 0.9$.

The test system is simulated $1,000$ times using Monte Carlo simulation for a duration of 110 s and with a time step of 0.05 s for both Cases 1.a and 1.c. A fault is applied in these simulations at Bus 7 at time 101 s that is cleared in 0.1 s. The resulting effect on the voltage at Bus 5 is shown in Figure 5.9 and 5.10. In these figures, the black line presents the voltage mean value of the $1,000$ simulations. This process gives an idea of the effect of the perturbation for the deterministic case, that is where the loads are not modeled as stochastic. In that case, the disturbance does not result in the voltage at Bus 5 reaching the lower voltage limit.

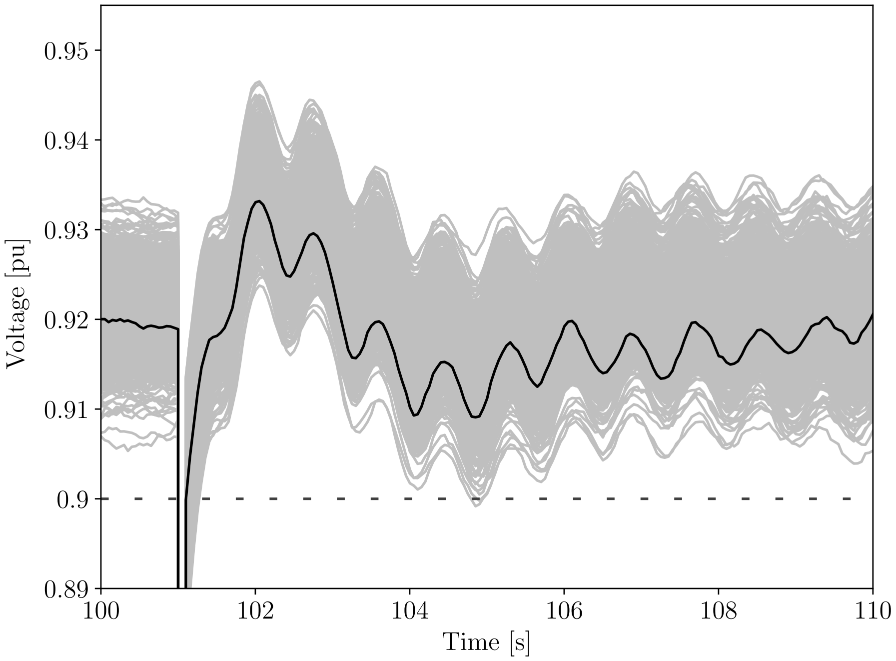

Figure 5.9: Voltage magnitude at Bus 5 with no correlation (Case 1.a). The trajectories of the 1, 000 simulations are shown in gray, the mean trajectory of the 1, 000 simulations is shown in black and the lower voltage limit of 0.9 pu is indicated with a dashed line.

Figure 5.9 shows that the voltage for only one trajectory goes below the voltage limit. This corresponds to 0.1 % of the simulations. In Figure 5.10, where the correlation in the active and reactive power of the loads is considered approximately 2 % of the trajectories go below the limit and stay there for a longer duration. This shows the importance of considering the correlation in the active and reactive power uncertainty when the voltage stability of the system is considered.

The correlation also affects the steady-state standard deviation of the voltage as can be seen in the spread of the simulated trajectories around the mean value in Figure 5.10 when compared to Figure 5.9. To further examine this point, the ramp rates of the voltage are computed using (4.20) and compared for the different scenarios.

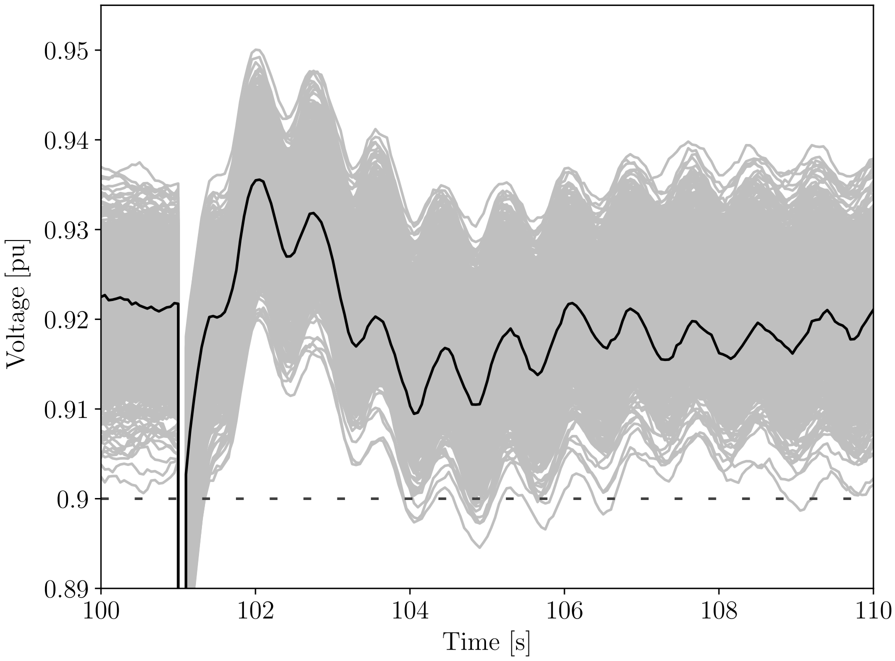

Figure 5.10: Voltage magnitude at Bus 5 with correlation (Case 1.c). The trajectories of the 1,000 simulations are shown in gray, the mean trajectory of the 1,000 simulations is shown in black and the lower voltage limit of 0.9 pu is indicated with a dashed line.

Ramp rates are obtained by simulating the system once for a duration of 10,000 s with a time step of 0.1 s without any disturbance. Figure 5.11 shows the standard deviations of the ramp rates of the voltage at Bus 5 for Case 1.a, 1.b and 1.c. The standard deviation increases as the correlation, ρ_W is increased. Thus, the more the stochastic variations of the active and reactive load power are correlated the bigger the variations/uncertainty in the voltages of the system.

Case 2

Three scenarios are considered, namely: (a) $\rho_J = \rho_{J_s} = 0$, (b) $\rho_J = 0.9$ and $\rho_{J_s} = 0$ and (c) $\rho_J = \rho_{J_s} = 0.9$. In all scenarios $\rho_W = 0$.

Figure 5.12 compares the standard deviation of the ramp rates in the voltage at Bus 5 for Case 2. If the jump times are correlated (Case 2.b), the standard deviation of the ramps in the voltage is significantly decreased when compared to the base case with no correlation (Case 2.a). Case 2.b, where the jump times

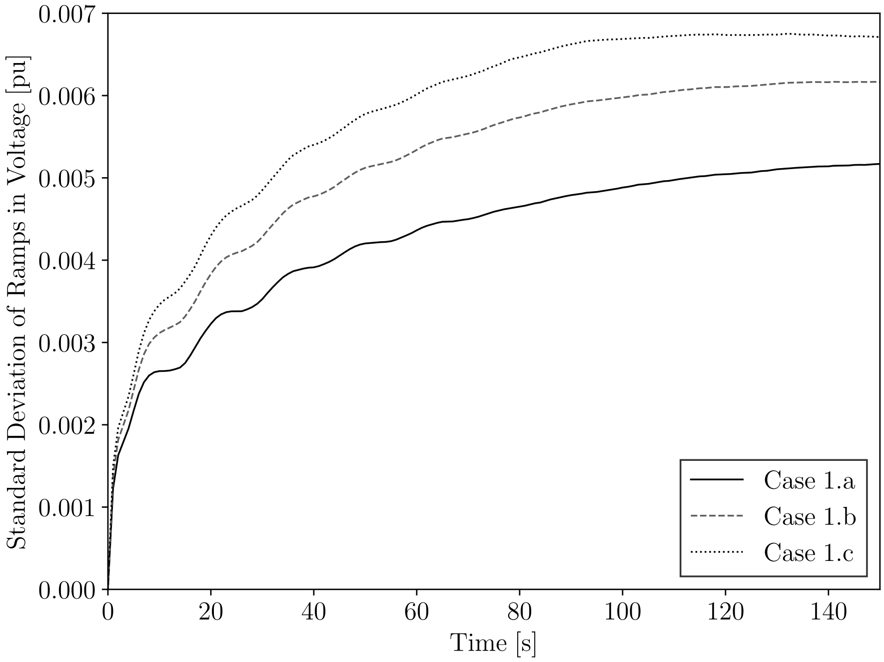

Figure 5.11: Standard deviation of the ramps in the voltage at Bus 5 of the test system for Cases 1.a, 1.b and 1.c.

are correlated but not the jump size, results in the lowest levels of ramps in the voltage. Case 2.c, where the jump times and sizes are both correlated, results in lower voltage ramps than if no correlation is considered.

5.5.2 Irish system model

In this case study, only the loads in the Irish system are modeled as stochastic. The model presented in Section 3.4, coupled with the same parameters as are used for the 9-bus test system, is used. In Figure 5.13, the standard deviation of the ramp rates in the voltage of a centrally located bus (Athlone in county Westmeath) in the Irish system is shown for Case 1.a, 1.b and 1.c. The same behavior is observed in this case. That is, with more correlation in the stochastic component of the active and reactive power of the loads, the higher the standard deviation of the ramp rates in the voltage, and thus, the higher the uncertainty.

The standard deviation in the ramp rates of the voltage at the same centrally located bus in the system for Case 2.a, 2.b and 2.c is shown in Figure 5.14. The

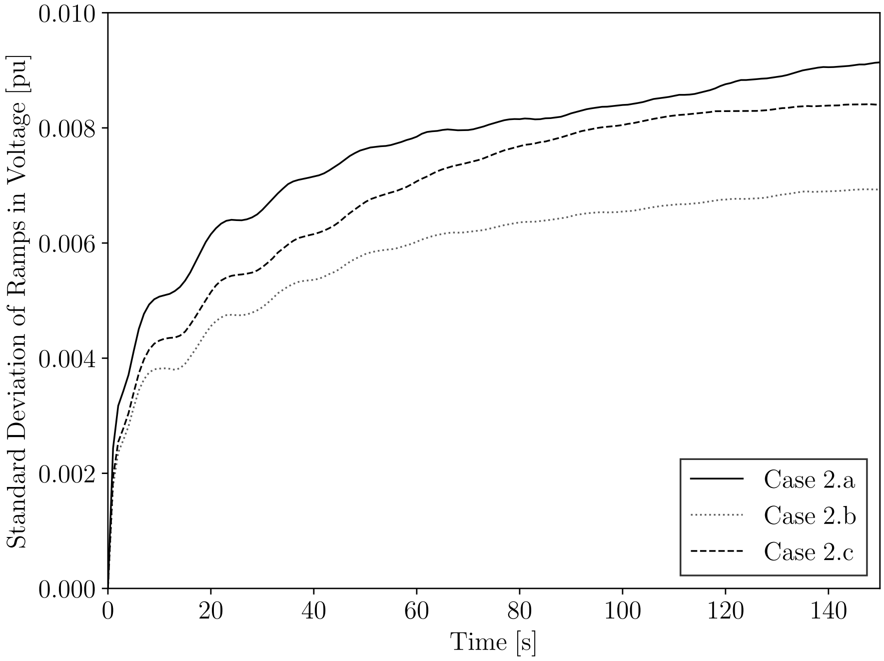

Figure 5.12: Standard deviation of the ramps in the voltage at Bus 5 of the test system for Cases 2.a, 2.b and 2.c.

same behavior can be seen for the Irish system as is observed for the 9-bus test system.

5.5.3 Remarks

The results for Cases 1 and 2 highlight the importance of modeling the correlation of the loads of the system as it affects the variations of bus voltages and thereby the stability limits of the whole network. The level and type of correlation in the active and reactive powers may vary for different types of loads. Thus, it appears relevant to examine measured data for a variety of loads and further investigate this correlated behavior.

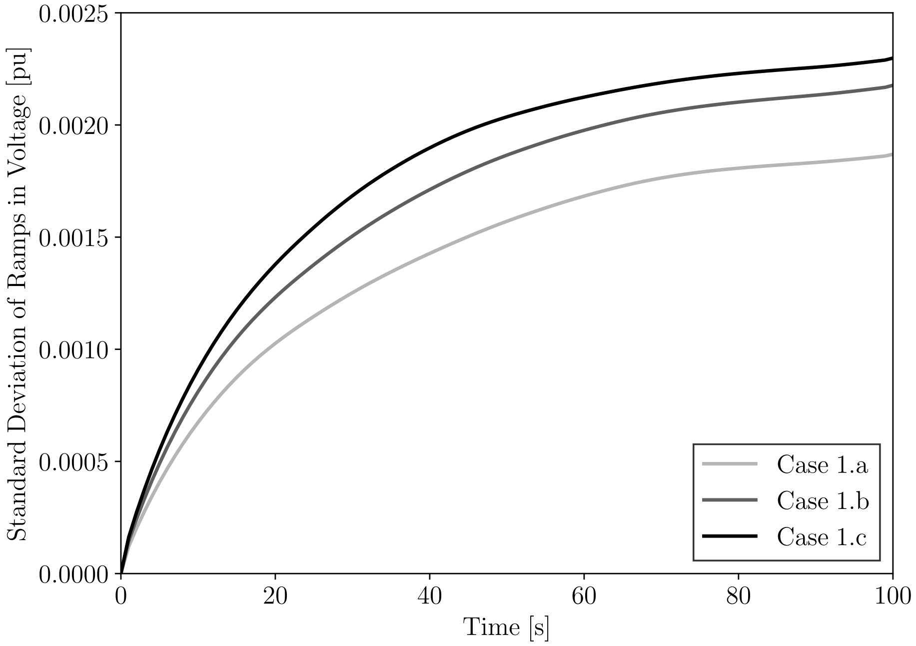

Figure 5.13: Standard deviation of the ramps in the voltage at a centrally located bus in the Irish system for Cases 1.a, 1.b and 1.c.

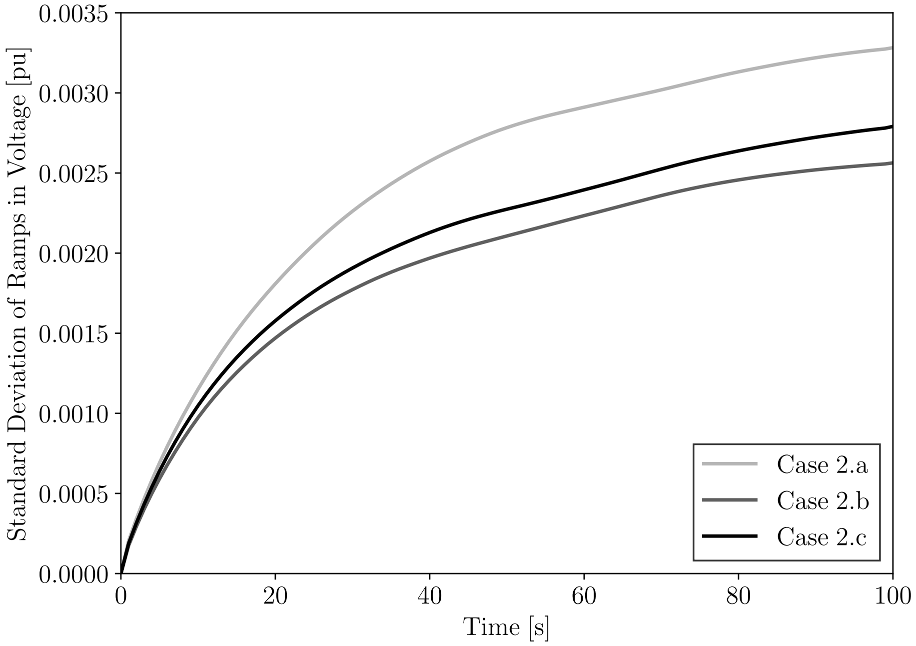

Figure 5.14: Standard deviation of the ramps in the voltage at a centrally located bus in the Irish system for Cases 2.a, 2.b and 2.c.

CHAPTER

SIX

CONCLUSIONS

This thesis discusses stochastic modeling for the short-term dynamic analysis of power systems. To model the sources of random variability in the system Stochastic Differential Equations (SDEs) are utilized. Chapter 2 presents the SDE-based methods utilized for modeling the sources of volatility in the system. In Table 6.1 the properties of the four stochastic modeling methods, presented in Chapter 2 are outlined. Methods I and II can be used to build a continuous SDE with an arbitrary PDF and an ACF that can be fitted as a sum of weighted decaying exponentials and sinusoidals based on data. Method II offers a more systematic approach to defining the SDE model based on the statistical properties of measured data, namely the PDF and ACF. However, Method I is a good option in a case where a predefined ARMA model is available. Method III allows modeling SDEs with jumps. This method does not propose a systematic way to define the jump diffusion SDE. This is because many different types of jumps may be encountered in stochastic measured data. Thus, more extensive data analysis is required than just defining the ACF and PDF. Finally, Method IV can be used to model the correlation of two SDEs in terms of the stochastic driving component and if present the jump component. A limitation of this method is that only the correlation between two processes can be modeled. However, in power systems multiple random perturbations in the system can be correlated.

Table 6.1: SDE methods presented in Chapter 2.

Method	PDF	ACF	Jumps	Correlation
I	Any numerical or analytical PDF	Sum of weighted decaying exponentials and sinusoidals	-	-
II			-	-
III	-	-	Yes	-
IV	-	-	Yes	Between two SDE processes

In Chapter 3, four sources of random fluctuations and jumps in power systems are modeled using the modeling methods presented in Table 6.1, namely wind, solar and tidal generation as well as loads. All the modeling in this chapter is supported by measured data and the models can all be used in dynamic analysis of power systems. In Chapter 3, it is demonstrated how Method I and II can be utilized to model wind speed based on measured data sets with a range of sampling frequencies, as presented in [38] and [72], respectively. It is shown that Method II specifically can be used to capture the stochastic properties of wind speed seen in measured data sampled with a sampling rate from a second to a hour. Method II is also used to model tidal current speed as presented in [116]. The method is used to model two measured data sets, one where the short-term variations are purely due to turbulence and one where they are due to a mix of turbulence and waves. In Chapter 3, measured solar irradiance data is analyzed. It is shown that the solar irradiance jumps up and down as clouds pass over the PV solar panel. To model the solar irradiance a SDE jump diffusion model is proposed using Method III as presented in [78]. A load model that uses Method III and IV, proposed in [117], is presented in Chapter 3. This model can model the correlation in the stochastic component, the jump size and time of the active and reactive power consumed by a load.

Chapter 4 focuses on the integration of the SDE-based models (proposed in Chapters 2 and 3) into power systems, modeled as a set of Differential Algebraic Equations (DAEs). The resulting stochastic power system model is a set of Stochastic Differential Algebraic Equation (SDAE). In this chapter a novel method to initialize the SDAE power system model is presented and compared to methods previously used, as discussed in [125]. Additionally, the adaptations done to model the aggregated volatile renewable sources, namely wind, solar and tidal are outlined. In this chapter, the One-Machine Infinite-Bus (OMIB) test system is used to show examples of simulations of a power system modeled as a set of SDAEs. It is demonstrated how the volatility of the renewable energy sources can affect the system variables in different ways.

In Chapter 5, four case studies utilizing the 1, 479 bus Irish power system model are outlined. First the proposed initialization method, presented in Chapter 4, is tested and it is shown that the method scales well for larger systems. The proposed initialization method has a lower computation time and requires less disc space when compared to other initialization methods previously used for SDAE-based power systems.

The Irish system, including tidal and wind generation, is tested as presented in [132]. Different scenarios where the tidal current speed is disturbed by turbulence and waves are considered. It is shown that by including frequency control in the tidal turbines the effect of the stochastic perturbations in the tidal current on the system frequency can be reduced to acceptable levels.

A similar study of the Irish system is also presented where the system includes wind and solar generation. It is shown that in the Irish system, including solar generation will result in lower ramps in the system frequency for clear sky days. However, in case of mixed clouding conditions solar generation introduces larger frequency ramps.

Finally, a case study where the effect of modeling the correlation in the active and reactive power of loads is presented that utilizes both the 9-bus test system and the Irish test system. It is shown that modeling the correlation is important when considering the voltage stability of the system. If the stochastic component of the active and reactive power model is more correlated it results in bigger voltage variations in the system. However, if the jumps are correlated the system voltage variations are lower compared to the uncorrelated case.

These case studies highlight the importance of considering the stochastic perturbations that affect power systems in dynamic system studies. The perturbations introduced by the various sources of random variations affect the system in different ways. Thus, it is important to use measured data to build models that accurately represent the sources of randomness.

6.1 Future work

Numerous routes can be taken to continue this thesis work. For example the SDE modeling methods, presented in Chapter 2, can be extended to model multiple correlated SDE processes. This work has already begun. Another important modeling aspect would be to develop a more systematic way to build jump diffusion SDE models based on measured data.

The models, presented in Chapter 3, utilizing the SDE-based modeling methods presented in Chapter 2, demonstrate the versatility of the presented modeling methods. Thus, in future work, these modeling methods can be utilized to model other sources of volatility in power systems.

Finally, the stochastic power system studies that can be performed utilizing the models proposed in this thesis are endless. Future work could focus on the implementation of some of these potential stochastic case studies.

References

REFERENCES

[1] M. T. Schilling, A. L. Da Silva, R. Billinton, and M. El-Kady, “Bibliography on power system probabilistic analysis (1962-88),” *IEEE Transactions on Power Systems*, vol. 5, no. 1, pp. 1–11, 1990. 1

[2] J. V. Milanović, “Probabilistic stability analysis: the way forward for stability analysis of sustainable power systems,” *Philosophical Transactions of the Royal Society A: Mathematical, Physical and Engineering Sciences*, vol. 375, no. 2100, p. 20160296, 2017. 1

[3] K. N. Hasan, R. Preece, and J. V. Milanović, “Existing approaches and trends in uncertainty modelling and probabilistic stability analysis of power systems with renewable generation,” *Renewable and Sustainable Energy Reviews*, vol. 101, pp. 168–180, 2019. 1

[4] F. Milano and R. Zárate-Miñano, “A systematic method to model power systems as stochastic differential algebraic equations,” *IEEE Transactions on Power Systems*, vol. 28, no. 4, pp. 4537–4544, 2013. 1, 67

[5] N. Ahmed and T. Dabbous, “Modelling and on-line control of reliability dynamics of large scale interconnected power systems,” *International journal of systems science*, vol. 14, no. 12, pp. 1321–1353, 1983. 2

[6] C. Nwankpa and S. Shahidehpour, “Colored noise modelling in the reliability evaluation of electric power systems,” *Applied mathematical modelling*, vol. 14, no. 7, pp. 338–351, 1990. 2

[7] ——, “A stochastic model for small disturbance stability analysis of electric power systems,” *International Journal of Electrical Power & Energy Systems*, vol. 13, no. 3, pp. 139–147, 1991. 2

[8] K. Loparo and G. Blankenship, “A probabilistic mechanism for small disturbance instabilities in electric power systems,” *IEEE Transactions on Circuits and Systems*, vol. 32, no. 2, pp. 177–184, 1985. 2

[9] S. Shahidehpour and J. Qiu, “Effect of random perturbations on the dynamic behavior of power systems,” *Electric power systems research*, vol. 11, no. 2, pp. 117–127, 1986. 2

[10] E. B. Iversen, J. M. Morales, J. K. Møller, and H. Madsen, “Short-term probabilistic forecasting of wind speed using stochastic differential equations,” *International Journal of Forecasting*, vol. 32, no. 3, pp. 981–990, 2016. 2, 33

[11] J. K. Møller, M. Zugno, and H. Madsen, “Probabilistic forecasts of wind power generation by stochastic differential equation models,” *Journal of Forecasting*, vol. 35, no. 3, pp. 189–205, 2016. 2, 33

[12] H. Verdejo, A. Awerkin, W. Kliemann, and C. Becker, “Modelling uncertainties in electrical power systems with stochastic differential equations,” *International Journal of Electrical Power & Energy Systems*, vol. 113, pp. 322–332, 2019. 2, 3

[13] C. Roberts, E. M. Stewart, and F. Milano, “Validation of the Ornstein-Uhlenbeck process for load modeling based on μPMU measurements,” in *Power Systems Computation Conference (PSCC)*, 2016. 2, 3, 16, 67

[14] M. Anvari, B. Werther, G. Lohmann, M. Wächter, J. Peinke, and H.-P. Beck, “Suppressing power output fluctuations of photovoltaic power plants,” *Solar Energy*, vol. 157, pp. 735–743, 2017. 2, 3, 27, 43, 44, 48, 49

[15] D. F. H. Larson, “Modeling nonlinear stochastic ocean loads as diffusive stochastic differential equations to derive the dynamic responses of offshore

wind turbines," Ph.D. dissertation, Massachusetts Institute of Technology, 2016. 2, 33

[16] F. M. Mele, R. Zárate-Miñano, and F. Milano, "Modeling load stochastic jumps for power systems dynamic analysis," *IEEE Transactions on Power Systems*, vol. 34, no. 6, pp. 5087–5090, 2019. 2, 3, 27, 67, 68

[17] R. Zárate-Miñano and F. Milano, "Construction of SDE-based wind speed models with exponentially decaying autocorrelation," *Renewable Energy*, vol. 94, pp. 186–196, 2016. 2, 3, 16, 24, 32, 33, 34, 36

[18] H. Li *et al.*, "Analytic analysis for dynamic system frequency in power systems under uncertain variability," *IEEE Transactions on Power Systems*, vol. 34, no. 2, pp. 982–993, 2018. 2, 3

[19] B. Yuan, M. Zhou, G. Li, and X.-P. Zhang, "Stochastic small-signal stability of power systems with wind power generation," *IEEE Transactions on Power Systems*, vol. 30, no. 4, pp. 1680–1689, 2015. 2, 3, 33

[20] X. Wang, H. D. Chiang, J. Wang, H. Liu, and T. Wang, "Long-term stability analysis of power systems with wind power based on stochastic differential equations: Model development and foundations," *IEEE Transactions on Sustainable Energy*, vol. 6, no. 4, pp. 1534–1542, 2015. 2, 3, 33

[21] T. Huang and J. Wang, "A practical method of transient stability analysis of stochastic power systems based on eeac," *International Journal of Electrical Power & Energy Systems*, vol. 107, pp. 167–176, 2019. 2, 3

[22] P. Ju, H. Li, C. Gan, Y. Liu, Y. Yu, and Y. Liu, "Analytical assessment for transient stability under stochastic continuous disturbances," *IEEE Transactions on Power Systems*, vol. 33, no. 2, pp. 2004–2014, 2017. 2, 3

[23] P. Ju, H. Li, X. Pan, C. Gan, Y. Liu, and Y. Liu, "Stochastic dynamic analysis for power systems under uncertain variability," *IEEE Transactions on Power Systems*, vol. 33, no. 4, pp. 3789–3799, 2017. 2, 3

[24] P. Ju, *Stochastic Dynamics of Power Systems.* Springer, 2019. 2

[25] W. Wu, K. Wang, G. Li, and Y. Hu, "A stochastic model for power system transient stability with wind power," *IEEE PES General Meeting*, 2014. 2, 3, 33

[26] R. H. Hirpara and S. N. Sharma, "An Ornstein-Uhlenbeck process-driven power system dynamics," *9th IFAC Symposium on Control of Power and Energy Systems (CPES)*, 2015. 2, 3

[27] H. Verdejo, W. Kliemann, and C. Becker, "A stochastic methodology to adjust controllers based on moments Lyapunov exponents: Application to power systems," *International Journal of Electrical Power & Energy Systems*, vol. 93, pp. 15–29, 2017. 2, 3

[28] A. Loukatou, S. Howell, P. Johnson, and P. Duck, "Stochastic wind speed modelling for estimation of expected wind power output," *Applied energy*, vol. 228, pp. 1328–1340, 2018. 2, 3

[29] X. Wang, T. Wang, H.-D. Chiang, J. Wang, and H. Liu, "A framework for dynamic stability analysis of power systems with volatile wind power," *IEEE Journal on Emerging and Selected Topics in Circuits and Systems*, vol. 7, no. 3, pp. 422–431, 2017. 2, 3

[30] R. Zárate-Minano, F. M. Mele, and F. Milano, "SDE-based wind speed models with Weibull distribution and exponential autocorrelation," *IEEE PES General Meeting*, 2016. 2, 3

[31] D. Villanueva, J. L. Pazos, and A. Feijoo, "Probabilistic load flow including wind power generation," *IEEE Transactions on Power Systems*, vol. 26, no. 3, pp. 1659–1667, 2011. 12

[32] B. Oksendal, *Stochastic differential equations: an introduction with applications.* Springer Science & Business Media, 2013. 13

[33] P. E. Kloeden, E. Platen, and H. Schurz, *Numerical solution of SDE through computer experiments.* Springer Science & Business Media, 2012. 13, 14, 88

[34] C. Gardiner, *Stochastic methods.* Springer Berlin, 2009, vol. 4. 13

[35] J. Chen, M. C. Hui, and Y. Xu, "A comparative study of stationary and non-stationary wind models using field measurements," *Boundary-layer meteorology*, vol. 122, no. 1, pp. 105–121, 2007. 15

[36] M. Olsson, M. Perninge, and L. Soder, "Modeling real-time balancing power demands in wind power systems using stochastic differential equations," *Electric Power Systems Research*, vol. 80, no. 8, pp. 966 – 974, 2010. 16

[37] M. Perninge, M. Amelin, and V. Knyazkins, "Load modeling using the Ornstein-Uhlenbeck process," in *IEEE 2nd International Power and Energy Conference (PECon)*, Johor Bahru, Malaysia, 2008, pp. 819–821. 16, 67

[38] G. M. Jónsdóttir, B. Hayes, and F. Milano, "Continuous-time ARMA models for data-based wind speed models," in *Power Systems Computation Conference (PSCC)*, 2018. 17, 32, 33, 34, 35, 111

[39] S. S. Pappas, L. Ekonomou, D. C. Karamousantas, G. Chatzarakis, S. Katsikas, and P. Liatsis, "Electricity demand loads modeling using AutoRegressive Moving Average (ARMA) models," *Energy*, vol. 33, no. 9, pp. 1353–1360, 2008. 18

[40] S.-J. Huang and K.-R. Shih, "Short-term load forecasting via ARMA model identification including non-Gaussian process considerations," *IEEE Transactions on Power Systems*, vol. 18, no. 2, pp. 673–679, 2003. 18

[41] K. Yunus, T. Thiringer and P. Chen, "ARIMA-based frequency-decomposed modeling of wind speed time series," *IEEE Transactions on Power Systems*, vol. 31, no. 4, pp. 2546–2556, 2016. 18, 20, 33

[42] E. Erdem and J. Shi, "ARMA based approaches for forecasting the tuple of wind speed and direction," *Applied Energy*, vol. 88, no. 4, pp. 1405–1414, 2011. 18, 20, 33

[43] A. Lojowska, "Wind speed modeling," Master's thesis, Delft, the Netherlands, 2009. 18, 20, 33

[44] J. Wu and S. Wei, *Time series analysis.* Hunan Science and Technology Press, ChangSha, 1989. 18, 21

[45] H. Tómasson, "Some computational aspects of Gaussian CARMA modelling," *Statistics and Computing*, vol. 25, no. 2, pp. 375–387, 2015. 19, 20, 21

[46] M. Grigoriu, *Applied non-Gaussian processes: Examples, theory, simulation, linear random vibration, and MATLAB solutions.* Prentice Hall, 1995. 20, 23

[47] P. J. Brockwell and R. A. Davis, *Introduction to time series and forecasting.* Springer, 2016. 20

[48] M. Phadke and S. Wu, "Modeling of continuous stochastic processes from discrete observations with application to sunspots data," *Journal of the American Statistical Association*, vol. 69, no. 346, pp. 325–329, 1974. 21, 23

[49] F. Lu, K. K. Lin and A. J. Chorin, "Comparison of continuous and discrete-time data-based modeling for hypoelliptic systems," *Communications in Applied Mathematics and Computational Science*, vol. 11, no. 2, pp. 187–216, 2016. 21

[50] P. Brockwell, "Continuous-time ARMA processes," *Handbook of Statistics*, vol. 19, pp. 249–276, 2001. 21

[51] O. E. Barndorff-Nielsen and N. Shephard, *Non-Gaussian OU based models and some of their uses in financial economics.* Nuffield College Oxford, 1999. 25

[52] E. Platen and N. Bruti-Liberati, *Numerical solution of stochastic differential equations with jumps in finance.* Springer Science & Business Media, 2010, vol. 64. 27, 50

[53] L. Márkus and A. Kumar, "Comparison of stochastic correlation models," *Journal of Mathematical Sciences*, vol. 237, no. 6, pp. 810–818, Mar 2019. 28

[54] R. Tabar, *Analysis and data-based reconstruction of complex nonlinear dynamical systems.* Springer, 2019. 28

[55] EirGrid Group, "Strategy 2020-25, Transform the power system for future generations," 2020. [Online]. Available: http://www.eirgridgroup.com/about/strategy-2025/EirGrid-Group-Strategy-2025-DOWNLOAD.pdf 32, 100

[56] V. L. Brano, A. Orioli, G. Ciulla, and S. Culotta, "Quality of wind speed fitting distributions for the urban area of Palermo, Italy," *Renewable Energy*, vol. 36, no. 3, pp. 1026–1039, 2011. 32

[57] T. B. M. J. Ouarda, C. Charron, J.-Y. Shin, P. R. Marpu, A. H. Al-Mandoos, M. H. Al-Tamimi, H. Ghedira, and H. T. N. Al, "Probability distributions of wind speed in the UAE," *Energy Conversion and Management*, vol. 93, pp. 414–434, 2015. 32

[58] J. A. Carta, P. Ramirez, and S. Velazquez, "A review of wind speed probability distributions used in wind energy analysis: Case studies in the Canary Islands," *Renewable and Sustainable Energy Reviews*, vol. 13, no. 5, pp. 933–955, 2009. 32

[59] T. Burton, N. Jenkins, D. Sharpe, and E. Bossanyi, *Wind energy handbook.* John Wiley & Sons, 2011. 32

[60] P. Milan, M. Wächter, and J. Peinke, "Turbulent character of wind energy," *Physical Review Letters*, vol. 110, no. 13, p. 138701, 2013. 32

[61] A. C. Brett and S. E. Tuller, “The autocorrelation of hourly wind speed observations,” *Journal of Applied Meteorology*, vol. 30, no. 6, pp. 823–833, 1991. 32

[62] R. B. Corotis, A. B. Sigl, and M. P. Cohen, “Variance analysis of wind characteristics for energy conversion,” *Journal of Applied Meteorology*, vol. 16, no. 11, pp. 1149–1157, 1977. 32

[63] G. M. Jónsdóttir, B. Hayes, and F. Milano, “Optimum data sampling frequency for short-term analysis of power systems with wind,” *IEEE PES General Meeting*, 2018. 32

[64] D. C. Hill, D. McMillan, K. R. W. Bell, and D. Infield, “Application of auto-regressive models to UK wind speed data for power system impact studies,” *IEEE Transactions on Sustainable Energy*, vol. 3, no. 1, pp. 134–141, 2012. 33

[65] L. Soder, “Simulation of wind speed forecast errors for operation planning of multiarea power systems,” in *Probabilistic Methods Applied to Power Systems, 2004 International Conference on.* IEEE, 2004, pp. 723–728. 33

[66] G. D’Amico, F. Petroni, and F. Prattico, “First and second order semi-Markov chains for wind speed modeling,” *Physica A: Statistical Mechanics and its Applications*, vol. 392, no. 5, pp. 1194–1201, 2013. 33

[67] A. Shamshad, M. A. Bawadi, W. M. A. W. Hussin, T. A. Majid, and S. A. M. Sanusi, “First and second order Markov chain models for synthetic generation of wind speed time series,” *Energy*, vol. 30, no. 5, pp. 693–708, 2005. 33

[68] M. Lei, L. Shiyan, J. Chuanwen, L. Hongling, and Z. Yan, “A review on the forecasting of wind speed and generated power,” *Renewable and Sustainable Energy Reviews*, vol. 13, no. 4, pp. 915–920, 2009. 33

[69] H. Verdejo, A. Awerkin, E. Saavedra, W. Kliemann, and L. Vargas, “Stochastic modeling to represent wind power generation and demand in

electric power system based on real data," *Applied Energy*, vol. 173, pp. 283–295, 2016. 33

[70] R. Calif, "PDF models and synthetic model for the wind speed fluctuations based on the resolution of Langevin equation," *Applied Energy*, vol. 99, pp. 173–182, 2012. 33

[71] R. Zárate-Miñano, M. Anghel, and F. Milano, "Continuous wind speed models based on stochastic differential equations," *Applied Energy*, vol. 104, pp. 42–49, 2013. 33

[72] G. M. Jónsdóttir and F. Milano, "Data-based continuous wind speed models with arbitrary probability distribution and autocorrelation," *Renewable Energy*, vol. 143, pp. 368–376, 2019. 33, 36, 37, 38, 111

[73] Met Éireann, The Irish meterological service online. Historical data (2017). [Online]. Available: http://met.ie/climate-request/ 34, 35, 37, 58

[74] RE<C: Renewable Electricity Less Than Coal. Surface Level Wind Data Collection (2017). [Online]. Available: https://code.google.com/archive/ 37, 58, 59, 80

[75] University of Massachusetts, Wind Energy Center. Resource Data (2018). [Online]. Available: https://www.umass.edu/windenergy/resourcedata 37

[76] BP, Statisical Review of World Energy (June 2018). [Online]. Available: https://www.bp.com/en/global/corporate/energy-economics/statistical-review-of-world-energy/renewable-energy/solar-energy.html 43

[77] A. Mills, M. Ahlstrom, M. Brower, A. Ellis, R. George, T. Hoff, B. Kroposki, C. Lenox, N. Miller, M. Milligan *et al.*, "Dark shadows," *Power and Energy Magazine*, vol. 9, no. 3, pp. 33–41, 2011. 43, 80

[78] G. M. Jónsdóttir and F. Milano, "Modeling solar irradiance for short-term dynamic analysis of power systems," *IEEE PES General Meeting*, 2019. 43, 46, 47, 50, 52, 81, 101, 111

[79] A. Mills, M. Ahlstrom, M. Brower, A. Ellis, R. George, T. Hoff, B. Kroposki, C. Lenox, N. Miller, J. Stein *et al.*, "Understanding variability and uncertainty of photovoltaics for integration with the electric power system," *The Electricity Journal*, 2009. 43

[80] Y. Dazhi, P. Jirutitijaroen, and W. M. Walsh, "The estimation of clear sky global horizontal irradiance at the equator," *Energy Procedia*, vol. 25, pp. 141–148, 2012. 43, 45

[81] M. J. Reno, C. W. Hansen, and J. S. Stein, "Global horizontal irradiance clear sky models: Implementation and analysis," *Sandia report (SAND2012-2389)*, 2012. 43, 45, 46

[82] R. Elliott, A. Ellis, P. Pourbeik, J. Sanchez-Gasca, J. Senthil, and J. Weber, "Generic photovoltaic system models for WECC-a status report," *IEEE PES General Meeting*, 2015. 43

[83] M. Hossain, T. Saha, N. Mithulananthan, and H. Pota, "Robust control strategy for PV system integration in distribution systems," *Applied Energy*, vol. 99, pp. 355–362, 2012. 43

[84] T. Alquthami, H. Ravindra, M. Faruque, M. Steurer, and T. Baldwin, "Study of photovoltaic integration impact on system stability using custom model of PV arrays integrated with PSS/E," in *North American Power Symposium (NAPS)*. IEEE, 2010, pp. 1–8. 44

[85] R. Ayyanar and A. Nagarajan, "Distribution system analysis tools for studying high penetration of PV with grid support features," *Arizona State University, Tech. Rep*, 2013. 44, 47

[86] A. Nagarajan and R. Ayyanar, "Methods for dynamic analysis of distribution feeders with high penetration of PV generators," in *Photovoltaic Specialists Conference (PVSC), IEEE*, 2016, pp. 1848–1852. 44, 47

[87] J. Sexauer and S. Mohagheghi, “Hybrid stochastic short-term models for wind and solar energy trajectories,” in *IEEE Green Technologies Conference (GreenTech)*, 2015, pp. 191–198. 44, 47, 48

[88] M. Sengupta, A. Andreas (2010). Oahu Solar Measurement Grid (1-Year Archive): 1-Second Solar Irradiance; Oahu, Hawaii (Data); NREL Report No. DA-5500-56506. [Online]. Available: http://dx.doi.org/10.5439/1052451 44, 45, 52

[89] M. Lave, J. Kleissl, and E. Arias-Castro, “High-frequency irradiance fluctuations and geographic smoothing,” *Solar Energy*, vol. 86, no. 8, pp. 2190–2199, 2012. 46

[90] R. Alcorn and D. O’Sullivan, Eds., *Electrical Design for Ocean Wave and Tidal Energy Systems*, ser. Energy Engineering. Institution of Engineering and Technology, 2013. 54

[91] Ocean Energy Forum, “Ocean energy strategic roadmap: Building ocean energy for Europe,” Tech. Rep., 2016. 54

[92] E. Segura, R. Morales, J. Somolinos, and A. López, “Techno-economic challenges of tidal energy conversion systems: Current status and trends,” *Renewable and Sustainable Energy Reviews*, vol. 77, pp. 536–550, 2017. 54

[93] L. Buchsbaum, “MeyGen Array Sets Global Record for Harnessing Tidal Power,” September 2018. [Online]. Available: https://www.powermag.com/meygen-array-sets-global-records-for-harnessing-tidal-power/ 54, 57

[94] T. Thiringer, J. MacEnri, and M. Reed, “Flicker evaluation of the SeaGen tidal power plant,” *IEEE Transactions on Sustainable energy*, vol. 2, no. 4, pp. 414–422, 2011. 55

[95] I. Milne, R. Sharma, R. Flay, and S. Bickerton, “Characteristics of the turbulence in the flow at a tidal stream power site,” *Philosophical Transactions of the Royal Society A: Mathematical, Physical and Engineering Sciences*, 2013. 55, 61, 63

[96] J. Thomson, B. Polagye, M. Richmond, and V. Durgesh, “Quantifying turbulence for tidal power applications,” in *IEEE Oceans, Seattle*, 2010. 55, 61, 63

[97] J. Filipot, M. Prevosto, C. Maisondieu, M. Le Boulluec, and J. Thomson, “Wave and turbulence measurements at a tidal energy site,” in *IEEE/OES Eleveth Current, Waves and Turbulence Measurement (CWTM)*, 2015. 55, 61, 63

[98] J. Thomson, B. Polagye, V. Durgesh, and M. C. Richmond, “Measurements of turbulence at two tidal energy sites in Puget Sound, WA,” *IEEE Journal of Oceanic Engineering*, vol. 37, no. 3, pp. 363–374, 2012. 55, 61, 63

[99] B. Sellar, G. Wakelam, D. Sutherland, D. Ingram, and V. Venugopal, “Characterisation of tidal flows at the european marine energy centre in the absence of ocean waves,” *Energies*, vol. 11, no. 1, p. 176, 2018. 55, 60

[100] M. Arnold, F. Biskup, and P. W. Cheng, “Load reduction potential of variable speed control approaches for fixed pitch tidal current turbines,” *International Journal of Marine Energy*, vol. 15, pp. 175–190, 2016. 55

[101] M. B. Anwar, M. S. El Moursi, and W. Xiao, “Dispatching and frequency control strategies for marine current turbines based on doubly fed induction generator,” *IEEE Transactions on Sustainable Energy*, vol. 7, no. 1, pp. 262–270, 2016. 55

[102] Z. Zhou, M. Benbouzid, J. F. Charpentier, F. Scuiller, and T. Tang, “A review of energy storage technologies for marine current energy systems,” *Renewable and Sustainable Energy Reviews*, vol. 18, pp. 390–400, 2013. 55, 59, 98

[103] K. Ghefiri, I. Garrido, S. Bouallègue, J. Haggège, and A. Garrido, “Hybrid neural fuzzy design-based rotational speed control of a tidal stream generator plant,” *Sustainability*, vol. 10, no. 10, p. 3746, 2018. 55

[104] Z. Zhou, F. Scuiller, J. F. Charpentier, M. E. H. Benbouzid, and T. Tang, "Power smoothing control in a grid-connected marine current turbine system for compensating swell effect," *IEEE Transactions on Sustainable Energy*, vol. 4, no. 3, pp. 816–826, 2013. 55

[105] K. Hasselmann, T. Barnett, E. Bouws, H. Carlson, D. Cartwright, K. Enke, J. Ewing, H. Gienapp, D. Hasselmann, P. Kruseman *et al.*, "Measurements of wind-wave growth and swell decay during the Joint North Sea Wave Project (JONSWAP)," *Ergänzungsheft 8-12*, 1973. 55

[106] Recommend Practice DNV-RP-C205 - Environmental conditions and environmental loads (April, 2014). [Online]. Available: https://rules.dnvgl.com/docs/pdf/DNV/codes/docs/2014-04/RP-C205.pdf 55

[107] J. Widén, N. Carpman, V. Castellucci, D. Lingfors, J. Olauson, F. Remouit, M. Bergkvist, M. Grabbe, and R. Waters, "Variability assessment and forecasting of renewables: A review for solar, wind, wave and tidal resources," *Renewable and Sustainable Energy Reviews*, vol. 44, pp. 356–375, 2015. 56

[108] H. Andre, "Operating experience with bulb units at the rance tidal power plant and other french hydro-power sites," *IEEE Transactions on Power Apparatus and Systems*, vol. 95, no. 4, pp. 1038–1044, 1976. 56

[109] M. J. Woo, "Tidal Energy: The New Sustainable Resource," *Wood Harbinger's newsletter series*, 2017. [Online]. Available: https://www.woodharbinger.com/tidal-energy-sustainable-resource/ 56

[110] World Energy Council (WEC), "World Energy Resources - Marine Energy," 2016. [Online]. Available: https://www.marineenergywales.co.uk/wp-content/uploads/2016/01/World-Energy-Council-Marine-Energy-Resources-2016.pdf 56

[111] G. Savidge *et al.*, “Strangford Lough and the SeaGen tidal turbine,” in *Marine renewable energy technology and environmental interactions.* Springer, 2014, pp. 153–172. 57, 93

[112] S. Benelghali, M. E. H. Benbouzid, and J. F. Charpentier, “Generator systems for marine current turbine applications: A comparative study,” *IEEE Journal of Oceanic Engineering*, vol. 37, no. 3, pp. 554–563, 2012. 57

[113] NOAA - Tides and currents, “Current data, February 15, 2019.” [Online]. Available: https://tidesandcurrents.noaa.gov/cdata/ 58

[114] A. I. Winter, “Differences in fundamental design drivers for wind and tidal turbines,” in *IEEE Oceans, Spain*, 2011. 58, 59, 80

[115] The Reliable Data Acquisition Platform for Tidal energy (ReDAPT), “Met-Ocean Data Science for Offshore Renewable Energy Applications),” 2017. [Online]. Available: http://redapt.eng.ed.ac.uk/index.php 59, 60

[116] G. M. Jónsdóttir and F. Milano, “Modeling of short-term tidal power fluctuations,” *IEEE Transactions on Sustainable Energy (in press)*, 2019. 60, 63, 82, 111

[117] ——, “Modeling correlation of active and reactive power of loads for short-term analysis of power systems,” *IEEE 20th International Conference on Environment and Electrical Engineering (EEEIC)*, 2020. 65, 68, 70, 88, 103, 111

[118] D. J. Hill, “Nonlinear dynamic load models with recovery for voltage stability studies,” *IEEE Transactions on Power Systems*, vol. 8, no. 1, pp. 166–176, 1993. 66

[119] V. Knyazkin, C. A. Cañizares, and L. H. Söder, “On the parameter estimation and modeling of aggregate power system loads,” *IEEE Transactions on Power Systems*, vol. 19, no. 2, pp. 1023–1031, 2004. 66

[120] G. Hou and V. Vittal, "Trajectory sensitivity based preventive control of voltage instability considering load uncertainties," *IEEE Transactions on Power Systems*, vol. 27, no. 4, pp. 2280–2288, 2012. 66

[121] L. Meiyan, M. Jin, and Z. Dong, "Uncertainty analysis of load models in small signal stability," in *International Conference on Sustainable Power Generation and Supply (SUPERGEN)*, Nanjing, China, 2009. 67

[122] Y. Zhou, Y. Li, W. Liu, D. Yu, Z. Li, and J. Liu, "The stochastic response surface method for small-signal stability study of power system with probabilistic uncertainties in correlated photovoltaic and loads," *IEEE Transactions on Power Systems*, vol. 32, no. 6, pp. 4551–4559, 2017. 67

[123] Z. Y. Dong, J. H. Zhao, and D. J. Hill, "Numerical simulation for stochastic transient stability assessment," *IEEE Transactions on Power Systems*, vol. 27, no. 4, pp. 1741–1749, 2012. 67

[124] N. Duan and K. Sun, "Stochastic power system simulation using the Adomian decomposition method," *arXiv*, 2017. 67

[125] G. M. Jónsdóttir, M. A. A. Murad, and F. Milano, "On the initialization of transient stability models of power systems with the inclusion of stochastic processes," *IEEE Transactions on Power Systems (in press)*, 2020. 73, 88, 112

[126] H. J. Carmichael, *Statistical methods in quantum optics 1: master equations and Fokker-Planck equations.* Springer Science & Business Media, 2013. 74

[127] E. Bølviken, N. Christophersen, and G. Storvik, *Linear dynamical models, Kalman filtering and statistics. Lecture notes to IN-ST 259.* University of Oslo, 1998. 75

[128] N. Chaudhuri, B. Chaudhuri, R. Majumder, and A. Yazdani, *Multi-terminal direct-current grids: Modeling, analysis, and control.* John Wiley & Sons, 2014. 79

[129] B. C. Cochran, “The influence of atmospheric turbulence on the kinetic energy available during small wind turbine power performance testing,” *Ceder-Ciemat. Spain April*, 2002. 79

[130] T. Petru and T. Thiringer, “Modeling of wind turbines for power system studies,” *IEEE Transactions on Power Systems*, vol. 17, no. 4, pp. 1132–1139, 2002. 79, 80

[131] T. Ackermann, *Wind power in power systems.* John Wiley & Sons, 2005. 79

[132] G. M. Jónsdóttir and F. Milano, “Stochastic modeling of tidal generation for transient stability analysis: A case study based on the all-island Irish transmission system,” in *Power Systems Computation Conference (PSCC)*, 2020. 80, 84, 88, 92, 94, 101, 112

[133] J. Marcos, Í. de la Parra, M. García, and L. Marroyo, “Simulating the variability of dispersed large PV plants,” *Progress in Photovoltaics: Research and Applications*, vol. 24, no. 5, pp. 680–691, 2016. 80

[134] S. Chakrabarti, *Handbook of Offshore Engineering (2-volume set).* Elsevier, 2005. 83, 84, 95

[135] A. N. Einrí, G. M. Jónsdóttir, and F. Milano, “Modeling and control of marine current turbines and energy storage systems,” *IFAC Workshop on Control of Smart Grid and Renewable Energy Systems (CSGRES), Jeju, Korea*, 2019. 84

[136] F. Milano, “A Python-based software tool for power system analysis,” *IEEE PES General Meeting*, 2013. 88, 90

[137] EirGrid Group, “All-Island Generation Capacity Statement 2018-2027,” 2018. [Online]. Available: http://www.eirgridgroup.com/site-files/library/EirGrid/Generation_Capacity_Statement_2018.pdf 89

[138] ——, "EirGrid Group Transmission System in January 2020," 2020. [Online]. Available: http://www.eirgridgroup.com/annual-report-2019/EirGrid-2020-Updates-to-Transmission-System-Map-A4-(Proof-1b).pdf 89

[139] ——, "EirGrid Group achieves record level of variable renewable energy on Irish electricity system," April 13, 2018. [Online]. Available: http://www.eirgridgroup.com/newsroom/record-renewable-energy-o/ 89

[140] F. O'Rourke, F. Boyle, and A. Reynolds, "Tidal current energy resource assessment in Ireland: Current status and future update," *Renewable and Sustainable Energy Reviews*, vol. 14, no. 9, pp. 3206–3212, 2010. 93, 94

[141] S. Gallagher, R. Tiron, and F. Dias, "A long-term nearshore wave hindcast for Ireland: Atlantic and Irish Sea coasts (1979–2012)," *Ocean Dynamics*, vol. 64, no. 8, pp. 1163–1180, 2014. 95

[142] M. Adeen, G. M. Jónsdóttir, and F. Milano, "Statistical correlation between wind penetration and grid frequency variations in the irish network," in *IEEE 19th International Conference on Environment and Electrical Engineering (EEEIC)*, 2019. 96, 97

[143] J. Cerqueira *et al.*, "Comparison of the dynamic response of wind turbine primary frequency controllers," in *IEEE PES General Meeting*, 2017. 99

[144] EirGrid Group, "All-Island Generation Capacity Statement 2019-2028," 2019. [Online]. Available: http://www.eirgridgroup.com/site-files/library/EirGrid/Generation_Capacity_Statement_2018.pdf 101

[145] P. W. Sauer and M. A. Pai, *Power system dynamics and stability*. Prentice Hall, 1998. 103